

# IMPROVEMENT OF SUBSONIC WALL CORRECTIONS IN AN INDUSTRIAL WIND TUNNEL

by

Alvaro TOLEDANO ESCALONA

THESIS PRESENTED TO ÉCOLE DE TECHNOLOGIE SUPÉRIEURE  
IN PARTIAL FULFILLMENT FOR THE DEGREE OF  
DOCTOR OF PHILOSOPHY  
Ph.D.

MONTRÉAL, OCTOBER 22, 2019

ÉCOLE DE TECHNOLOGIE SUPÉRIEURE  
UNIVERSITÉ DU QUÉBEC



Alvaro Toledano Escalona, 2019



Cette licence Creative Commons signifie qu'il est permis de diffuser, d'imprimer ou de sauvegarder sur un autre support une partie ou la totalité de cette œuvre à condition de mentionner l'auteur, que ces utilisations soient faites à des fins non commerciales et que le contenu de l'œuvre n'ait pas été modifié.

## **BOARD OF EXAMINERS**

**THIS THESIS HAS BEEN EVALUATED**

**BY THE FOLLOWING BOARD OF EXAMINERS:**

Mr. Julien Weiss, Thesis Supervisor  
Department of Mechanical Engineering at École de technologie supérieure

Mr. Simon Joncas, Chair, Board of Examiners  
Department of Systems Engineering at École de technologie supérieure

Mr. Patrice Seers, Member of the Jury  
Department of Mechanical Engineering at École de technologie supérieure

Mr. Norbert Ulbrich, External Evaluator  
NASA Ames Research Center

Mr. Marc Langlois, External Evaluator  
Bombardier Aerospace

Mr. Cabot Broughton, External Evaluator  
National Research Council of Canada

**THIS DISSERTATION WAS PRESENTED AND DEFENDED**

**IN THE PRESENCE OF A BOARD OF EXAMINERS AND PUBLIC**

**ON AUGUST 27 2019**

**AT ÉCOLE DE TECHNOLOGIE SUPÉRIEURE**



## **ACKNOWLEDGEMENTS**

A sincere thank you to my Ph.D. advisor, Professor Julien Weiss, for the opportunity provided to carry out this research project and his assistance over these years.

I would like to thank the staff at the Uplands Campus of the National Research Council, with special mention to Cabot Broughton, an undeniable source of advice and expertise throughout my journey in the world of wind-tunnel testing.

To all members of the jury, because I profoundly respect you and your work and I am honored to present you with the fruit of my research.

To my parents, my brothers and my sister; because despite the enormous distance between us you have believed in me and supported me when I decided to take up this beautiful but incredibly tough endeavor .

Finally, I would like to acknowledge the support of Bombardier Inc., the Natural Sciences and Engineering Research Council of Canada and the National Research Council's Aeronautical Product Development Technologies program.



# **Improvement of subsonic wall corrections in an industrial wind tunnel**

Alvaro TOLEDANO ESCALONA

## **ABSTRACT**

The National Research Council 5ft Trisonic Wind Tunnel enables testing of half-span models at a high Reynolds number cost effectively, however there is the possibility of experiencing relatively larger wall-interference effects compared to full span tests. Subsonic wall-interference effects due to the partially open boundaries at the NRC 5ft wind tunnel are corrected by the “one-variable” method, resulting in corrections in Mach number and angle of attack for the measured quantities. This dissertation introduces the need for adequately correcting for wall interference in subsonic half-model wind-tunnel testing in both pre-stall and post-stall conditions. The one-variable method is described and several aspects that require validation and improvement in this method are pointed out based on specific experimental and numerical results obtained for different test articles.

An initial assessment of the influence of the different possible tunnel configurations and computational parameters is defined based on experimental data from a test performed on a scaled model of the Bombardier Global 6000 business jet. This initial study unveils some of the weaknesses of the one-variable method. While this method provides accurate wall corrections during tests in pre-stall conditions; it is unable to generate reliable corrections in stall. Partially, this is due to the development of flow separation on a model tested at subsonic flow conditions reaching stall, not currently accounted for by the potential theory model representation used by the wall-correction methodology at the NRC 5ft TWT. Possible improvements to this singularity representation, paramount to the one-variable method, are then investigated. This revision of the model representation is based on high fidelity free-air CFD solutions for the NASA Common Research Model, validated by experimental data sets obtained from a semispan version of the CRM tested at the NRC 5ft Trisonic Wind Tunnel. The improved potential representation is tested on solid-wall experimental wind-tunnel data to present more reliable behavior of the wall-interference correction estimates when substantial wing stalling is encountered.

**Keywords:** wind tunnel, wall interference, wall correction, half-span, ground testing, subsonic flow, computational fluid dynamics.





# **Améliorations des corrections de parois en écoulement subsonique dans une soufflerie industrielle**

Alvaro TOLEDANO ESCALONA

## **RÉSUMÉ**

La soufflerie trisonique de 5 pieds du Conseil National de Recherches du Canada permet de réaliser des essais demi-maquette à un nombre de Reynolds élevé de façon efficace. En revanche, on peut s'attendre à des effets d'interférence des murs relativement plus importants que ceux rencontrés lors des essais avec des maquettes à pleine envergure. Les effets d'interférence de paroi subsoniques dus aux limites partiellement ouvertes de la soufflerie de 5 pieds du CNRC sont corrigés par la méthode "one-variable". Cette méthode fournit des corrections pour le nombre de Mach et de l'angle d'attaque mesurés. Dans ces travaux est introduit le besoin de corriger de manière appropriée l'interférence des parois dans les essais demi-maquette en écoulement subsonique, avant et après le décrochage.

Une évaluation initiale de l'influence des différentes configurations de la soufflerie et des paramètres de calcul possibles, est définie à partir de données expérimentales provenant d'un essai effectué sur un modèle à échelle réduite du jet d'affaires Bombardier Global 6000. Cette étude initiale met en lumière les limitations de la méthode one-variable. Bien qu'elle fournisse des corrections de paroi précises pendant les essais dans des conditions de pré-décrochage, cette méthode ne permet pas de générer des corrections fiables en conditions de décrochage. Cela est dû en partie au fait que le modèle utilisée par la méthode de correction des murs, basé dans la théorie d'écoulement potentiel, ne prends pas actuellement en compte ces conditions. Des améliorations de cette représentation potentielle du modèle, essentielle à la méthode one-variable, sont étudiées par la suite. Cette révision de la représentation du modèle est basée sur des résultats CFD obtenus pour le NASA Common Research Model, validés ensuite par des données expérimentales obtenues à partir d'une version demi-maquette du CRM testée à la soufflerie trisonique de 5 pieds du CNRC. La nouvelle représentation potentielle proposée, est finalement testée sur des données expérimentales de soufflerie à paroi solide, ce qui permet d'obtenir des corrections de paroi plus fiables lorsque le décrochage de l'aile est significatif.

**Mots-clés :** soufflerie, interférence parois, corrections parois, demi-maquette, essais au sol, écoulement subsonique, mécanique des fluides numérique.



## TABLE OF CONTENTS

	Page
INTRODUCTION .....	1
0.1 History and background.....	3
0.2 Scope and approach .....	5
CHAPTER 1 LITERATURE REVIEW AND STATE OF THE ART .....	7
1.1 Main factors of aerodynamic interference in wind-tunnel testing.....	9
1.1.1 Flow speed .....	9
1.1.2 Wind-tunnel models.....	14
1.1.3 Wind-tunnel design.....	15
1.1.4 Nature of the wind-tunnel test.....	19
1.2 Wind-tunnel wall-interference correction.....	20
1.2.1 Classification of wall corrections.....	21
1.2.2 Wall-correction calculation techniques.....	24
1.2.3 Wall-correction methods.....	28
1.3 The one-variable method at the NRC 5ft TWT .....	36
1.4 Problem statement.....	42
CHAPTER 2 OBJECTIVES.....	45
2.1 Main goal - Improve wall corrections in stall conditions .....	45
2.2 Secondary objectives .....	45
CHAPTER 3 METHODOLOGY .....	47
3.1 Development of an offline test bench for the one-variable method.....	47
3.2 Geometries considered for the investigations at the NRC 5ft TWT.....	49
3.2.1 Bombardier Global 6000.....	49
3.2.2 NRC Symmetrical Calibration Wing.....	50
3.2.3 NASA Common Research Model.....	54
3.3 Study of the NASA Common Research Model (CRM) at NRC TWT.....	57
3.3.1 NASA CRM experimental test campaign.....	58
3.3.2 NASA CRM numerical simulations .....	59
3.4 The use of CFD to improve and validate wall corrections .....	66
CHAPTER 4 RESULTS .....	69
4.1 Parametric study on semispan models tested at the NRC 5ft TWT.....	69
4.2 CFD-based Validation of the Complete Wall Correction Algorithm .....	74
4.3 Improvement of the current non-pitching Rankine body fuselage representation.....	76
4.4 Improvement of the current wing representation.....	84
4.5 Overall improvement to Wall Corrections.....	97
4.6 CFD-based Wall-Correction Data Set .....	98
4.7 Applications to Transonic Flow.....	100

CONCLUSIONS AND PERSPECTIVES.....	103
REFERENCES.....	107

## LIST OF TABLES

		Page
Table 1.1	Classification of wall corrections.....	23
Table 1.2	Keller Wall Boundary Conditions coefficients.....	33
Table 1.3	Semispan Global 6000 test campaign matrix.....	42
Table 3.1	NRC calibration wing (Calwing) geometry specifications. ....	50
Table 3.2	Test configuration during NRC TWT run 56303 for the NACA 0012 “calwing”. ....	52
Table 3.3	Semispan CRM geometry specifications. ....	55
Table 3.4	Normalized spanwise section location $\eta$ of the pressure port rows on the semispan CRM wing. ....	56
Table 3.5	Semispan CRM test campaign matrix.....	58
Table 3.6	Computational grid parameters for the CRM WB meshes. ....	60



## LIST OF FIGURES

	Page
Figure 0.1	Stages of the aircraft design process, from concept to manufacturing. ....1
Figure 1.1	Different approaches to obtain high Reynolds number by adjusting wind-tunnel testing parameters .....8
Figure 1.2	Wall interference described as the difference between the wind-tunnel and free-air flow fields. ....9
Figure 1.3	Elementary singularities of the Laplace equation in potential flow models. From: Krynytzky and Ewald in AGARDograph 336 (1998). ....11
Figure 1.4	Example of a potential theory representation for an aircraft wind-tunnel model. From: Iyer and Everhart (2001). ....12
Figure 1.5	Sketch of a full-span model (left) and a semispan model (right) of an aircraft in the same test section. Notice the higher model span-to-tunnel width ratio for the semispan case. ....14
Figure 1.6	Overview of the NRC 5ft Trisonic Wind Tunnel. ....16
Figure 1.7	Detail view of the wall perforations in the NRC 5ft wind-tunnel test section. ....18
Figure 1.8	Layout of the reflection-plate and pressure rails in the NRC 5ft wind-tunnel test section. ....19
Figure 1.9	Contour plot showing the variation of the angle-of-attack over a tunnel model to illustrate the concept of first and higher order corrections. ....23
Figure 1.10	Vortex near a solid boundary and image vortex placed to guarantee the no flow through condition. From: Kuethé and Chow (1986). ....25
Figure 1.11	Illustration of the method of images: Image system for a wing in a closed rectangular tunnel. From: Rae and Pope (1984). ....26
Figure 1.12	Example of a discretization of the geometry of a three-dimensional body using a panel representation with constant-strength surface doublets and sources. From: Katz and Plotkin (2001). ....27

Figure 1.13	NASA Ames 12ft PWT test section interior and paneling. From: Ulbrich (1998).....	32
Figure 1.14	Real-time wall interference calculation at NASA Ames 11ft TWT. From: Ulbrich <i>et al.</i> (2003).....	34
Figure 1.15	Region and bounding surfaces for application of Green's theorem. From: Ashill <i>et al.</i> (1982). ....	35
Figure 1.16	Distribution of pressure rows in the RAE 13ft x 9ft Low-Speed Wind Tunnel From: Ashill <i>et al.</i> (1988). ....	36
Figure 1.17	NRC 5ft TWT test section and mirror image respect to reflection plane. ....	38
Figure 1.18	Panel distribution on boundary test surface. ....	39
Figure 1.19	Interference velocity interpolation sequence. ....	40
Figure 1.20	Angle-of-attack correction for the Global 6000 solid-wall data set. ....	43
Figure 3.1	Contour maps including Mach number and angle of attack corrections. The red dot indicates the location of the model's reference point in the wind tunnel. ....	48
Figure 3.2	Semispan Bombardier Global 6000 model. ....	49
Figure 3.3	Semispan NRC calibration wing (Calwing) model. ....	51
Figure 3.4	Assembly of semispan calibration wing (Calwing) at NRC TWT. ....	52
Figure 3.5	Experimentally measured aerodynamic coefficients for the symmetrical calibration wing tested at the NRC TWT with a solid-wall test boundary at $M=0.25$ and $Re=3.97 \times 10^6$ ....	53
Figure 3.6	NRC experimental wing pressure distributions at $\alpha=15^\circ$ measured on the symmetrical calibration wing tested at the NRC TWT (run 56303). ....	54
Figure 3.7	NRC experimental wing pressure distributions at $\alpha=20^\circ$ measured on the symmetrical calibration wing tested at the NRC TWT (run 56303). ....	54
Figure 3.8	Location of the nine rows of wing pressure taps at the 2.7% scale semispan NASA CRM. ....	56
Figure 3.9	Assembly of semispan NASA CRM at NRC TWT. ....	57



Figure 3.10	Coarse (left), medium (middle) and fine (right) CRM surface meshes.....	60
Figure 3.11	Measured model loads at $\alpha=5.02^\circ$ compared to those predicted by CFD at $\alpha=5^\circ$ using the three meshes considered versus the number of grid points $N$ to the power of $-2/3$ . ....	61
Figure 3.12	Measured model loads at $\alpha=12.32^\circ$ compared to those predicted by CFD at $\alpha=12.5^\circ$ using the three meshes considered versus the number of grid points $N$ to the power of $-2/3$ . ....	61
Figure 3.13	CFD predicted aerodynamic coefficients for the CRM WB half-model (red-filled CFD data points indicate flow separation is significant) compared to ventilated-wall NRC experimental results (run 56307).....	62
Figure 3.14	CFD predicted wing pressure distributions at $\alpha=0^\circ$ compared to NRC experimental ventilated-wall results (run 56307) at $\alpha=0.08^\circ$ .....	63
Figure 3.15	CFD-predicted evolution of the flow separation over the CRM wing. The x-component of the skin friction coefficient vector is used to indicate flow separation on the suction side of the wing.....	64
Figure 3.16	CFD predicted wing pressure distributions at $\alpha=11.25^\circ$ compared to NRC experimental ventilated-wall results (run 56307) at $\alpha=11.29^\circ$ .....	65
Figure 3.17	CFD predicted wing pressure distributions at $\alpha=14^\circ$ compared to NRC experimental ventilated-wall results (run 56307) at $\alpha=13.93^\circ$ .....	65
Figure 3.18	Theoretical “zero” wall interference described as the difference between CFD-predicted and potential theory free-air flow fields. ....	67
Figure 3.19	Mach and angle-of-attack “zero-correction” uncertainty budget based on AGARDograph 184. ....	68
Figure 4.1	Computational boundary for panel method. From: Mokry <i>et al.</i> (1987).....	70
Figure 4.2	Results from the computational boundary surface parametric study using solid-wall experimental data from a test performed on the Bombardier Global 6000 model.....	71
Figure 4.3	Results from the reference pressure re-adjustment using solid-wall experimental data from a test performed on the Bombardier Global 6000 model.....	72

Figure 4.4	Original (top) and extended (bottom) versions of the NRC TWT reflection plate. ....	73
Figure 4.5	Results from the study of the influence of the reflection plane extension using solid-wall experimental data from a test performed on the Bombardier Global 6000 model.....	74
Figure 4.6	Validation of the one-variable method using free-air CFD results as input. ....	75
Figure 4.7	Rankine body fuselage representation over sketch of the CRM fuselage relative to the NRC 5ft TWT boundary location. ....	77
Figure 4.8	Pressure signature at the Top North (TN) rail location comparing (a) the Rankine body fuselage representation to (b) a CFD simulation of the actual 2.7% scale NASA CRM fuselage. ....	78
Figure 4.9	Error band for Mach number and angle of attack corrections computed using the one-variable method applying the original fuselage representation of the CRM. ....	79
Figure 4.10	Singularity distribution in the updated fuselage representation over sketch of the CRM fuselage relative to the NRC 5ft TWT boundary location.....	81
Figure 4.11	Pressure signature at the Top North (TN) rail comparing (a) the updated fuselage representation to (b) a CFD simulation of the actual 2.7% scale NASA CRM fuselage.....	82
Figure 4.12	CFD validation of the n=22 sources-sinks and n=22 doublets fuselage representation for $\alpha=0^\circ$ .....	82
Figure 4.13	CFD validation of the n=22 sources-sinks and n=22 doublets fuselage representation for $\alpha=10^\circ$ .....	83
Figure 4.14	CFD validation of the n=22 sources-sinks and n=22 doublets fuselage representation for $\alpha=20^\circ$ .....	83
Figure 4.15	Error band for Mach number and angle of attack corrections computed using the one-variable method applying the updated fuselage representation of the CRM. ....	84
Figure 4.16	Sketch of the singularity distribution employed to represent the model's wing.....	85

Figure 4.17	Comparison between the farfield pressure signature estimated by the potential-theory representation of the CRM and that predicted by CFD at $\alpha=0^\circ$ , $C_L=0.195$ ..	87
Figure 4.18	Comparison between the farfield pressure signature estimated by the potential-theory representation of the CRM and that predicted by CFD at $\alpha=14^\circ$ , $C_L=1.033$ ..	87
Figure 4.19	Error band for Mach number and angle of attack corrections computed using the one-variable method applying the original wing representation of the CRM WB.	88
Figure 4.20	CFD predicted separation bubble at the CRM wing at $\alpha=11.25^\circ$ .	89
Figure 4.21	CFD predicted separation bubble at the CRM wing at $\alpha=14^\circ$ .	90
Figure 4.22	Qualitative estimation of the separation bubble size over the CRM WB at $\alpha=14^\circ$ .	90
Figure 4.23	Sketch of the singularity distribution employed to represent the model's wing, including a doublet distribution to represent the separation bubble volume effects.	91
Figure 4.24	CFD predicted separation bubble at CRM wing station $\eta=0.950$ at $\alpha=14^\circ$ . The streamlines illustrate the recirculating flow region in the bubble.	92
Figure 4.25	Error band for Mach number and angle of attack corrections computed using the one-variable method including the separation bubble volume on the wing representation of the CRM WB.	92
Figure 4.26	Sketch of the singularity distribution employed to represent the model's wing, including the redistribution of the horseshoe vortices to account for flow separation at the outboard region of the wing.	94
Figure 4.27	Error band for Mach number and angle of attack corrections computed using the one-variable method including the skin friction estimated effective span on the wing representation of the CRM WB.	94
Figure 4.28	Comparison between the farfield pressure signature estimated by the potential-theory representation of the CRM considering the lift vortices redistribution (based on skin friction data from CFD results) and that predicted by CFD at $\alpha=14^\circ$ , $C_L=1.033$ .	95

Figure 4.29	Error band for Mach number and angle of attack corrections computed using the one-variable method including the wing pressure tap estimated effective span on the wing representation of the CRM WB. ....	96
Figure 4.30	Error band for Mach number and angle of attack corrections computed using the one-variable method including the balance data estimated effective span on the wing representation of the CRM WB. ....	97
Figure 4.31	Comparison between Mach number and angle of attack corrections computed using the one-variable method for the half-model CRM WB solid-wall test, using the original and updated potential theory model representations. ....	98
Figure 4.32	CFD predicted aerodynamic coefficients for the CRM WB half-model (red-filled CFD data points indicate flow separation is significant) compared to solid-wall NRC experimental results from run 56306. ....	99
Figure 4.33	Mach number and angle of attack corrections computed using the one-variable method for the half-model CRM WB solid-wall test, based on the validated free-air CFD results. ....	100
Figure 4.34	Additional Mach number corrections computed using the one-variable method to rectify the supersonic bubble effects over the half-model CRM WB, based on CFD results. ....	101

## **LIST OF ABBREVIATIONS**

AGARD	Advisory Group for Aerospace Research and Development
AIAA	American Institute of Aeronautics and Astronautics
CASI	Canadian Aeronautics and Space Institute
CFD	Computational Fluid Dynamics
CRM	(NASA) Common Research Model
DFS	Design and Fabrication Services (of NRC)
DND	Department of National Defense (Canada)
ESDU	Engineering Sciences Data Unit
ESP	Electronically Scanned Pressure
ETW	European Transonic Windtunnel
JAXA	Japan Aerospace Exploration Agency
LaRC	Langley Research Center
NACA	National Advisory Committee for Aeronautics
NAE	National Aeronautical Establishment
NASA	National Aeronautics and Space Administration
NFAC	National Full-Scale Aerodynamics Complex
NRC	National Research Council
NTF	National Transonic Facility
ONERA	Office National d'Etudes et de Recherches Aérospatiales
PWT	Pressure Wind Tunnel
RAE	Royal Aircraft Establishment
RANS	Reynolds-Averaged Navier–Stokes
TWICS	Real-Time Wall Interference Correction System
TWT	Trisonic Wind Tunnel or Transonic Wind Tunnel
V/STOL	Vertical and/or Short Take-Off and Landing
WB	Wing-Body
WICS	Wall Interference Correction System



## LIST OF SYMBOLS

$b$	Wingspan, in
$c$	Wing mean aerodynamic chord, in
$C_D$	Drag coefficient
$C_l$	Rolling moment coefficient
$C_L$	Lift coefficient
$C_M$	Pitching moment coefficient
$C_P$	Pressure coefficient
$L$	Fuselage length, in
$m$	Rankine body strength
$M$	Mach number
$r$	Fuselage radius, in
$q$	Dynamic pressure, psi
$Re_c$	Reynolds number based on mean aerodynamic chord
$S$	Model reference area, in <sup>2</sup>
$U$	Flow reference velocity
$u$	Streamwise velocity (x-component of flow velocity vector)
$v$	Side velocity (y-component of flow velocity vector)
$\vec{V}$	Flow velocity field
$w$	Upwash velocity (z-component of flow velocity vector)
$\alpha$	angle of attack, deg
$\beta$	Prandtl-Glauert factor
$\Gamma$	Vortex strength
$\Delta M$	Mach number correction
$\Delta \alpha$	Angle of attack correction
$\epsilon$	Blockage factor
$\eta$	Normalized spanwise position $y/(0.5b)$
$\kappa$	Ratio of specific heats
$\rho$	Flow density

$\sigma$	Source/sink strength
$\xi$	Compressibility-scales axial coordinate
$\mu$	Flow viscosity or doublet strength
$\phi$	Velocity potential



## INTRODUCTION

Aircraft design is the engineering process of creating a flying vehicle that meets a series of specifications and requirements, generally established by an aircraft manufacturer. Occasionally, these aircraft designs may be part of scientific investigations to explore innovative technologies. Conceptual design, preliminary design and detail design are the three subsequent phases of this engineering process (Anderson, 1999). A general aircraft configuration layout should be the result from the conceptual design phase. This configuration is then subject to minor changes during the preliminary design phase. At this point, substantial wind-tunnel testing will be carried out in combination with the application of computational fluid dynamics (CFD) simulations to verify design requirements and unveil any potential design flaws that may drive configuration changes, as part of experimental test cycles much like those presented by Blackwell (1982). At the end of this preliminary design phase, the aircraft configuration should be precisely defined before committing to the endeavor of manufacturing a full-scale aircraft. The detail design phase consists of defining the necessary elements that will concern the manufacturing and technical assembly of the aircraft, literally this would be the “nuts and bolts” phase of the design. This concludes the design process, which is followed by prototype manufacturing, flight test, certification and production.



Figure 0.1 Stages of the aircraft design process, from concept to manufacturing.

This research project has a particular interest in the preliminary design phase of contemporary transport aircrafts, specifically in one of the main tools employed at this stage, wind-tunnel testing. It will also explore its relationship with CFD. Over the last 40 years, the development of CFD has been partially responsible for the reduction in the use of wind-tunnel tests. As a result, a number of wind tunnels have been decommissioned. Nevertheless, wind-tunnel testing continues to be paramount to the aircraft design process to test flight configurations at subsonic speed and high angle-of-attack, characteristic of take-off or landing. A good example would be the determination of the maximum lift coefficient  $C_{Lmax}$ . For an aircraft at a given speed, lift increases almost linearly until its maximum at a critical value of the angle of attack, the stall point, before dropping as a consequence of flow separation at high incidence. Understanding aerodynamic behavior during stall is a very important phase of the design of any aircraft. However, the flow complexity when separation begins to develop close to the stall point makes predicting  $C_{Lmax}$  mathematically very complicated (Tinoco *et al.*, 2005). Therefore, CFD cannot be used autonomously to develop high-lift system details if the adequate prediction of maximum lift cannot be made. Under these circumstances, common CFD simulations would fall short and the use of wind-tunnel testing would be required. Aircraft manufacturers know the importance of such an essential tool and very rarely would they fly a vehicle that has not been previously tested in a wind-tunnel.

As wind-tunnel testing continues to have a powerful impact on the aircraft design process, there is interest in how to improve the accuracy of tunnel tests results. The National Research Council of Canada (NRC) Trisonic Wind Tunnel (TWT) is a perfect example of a facility with outstanding capabilities that, after over fifty years of operation, still continues to invest in its own development and improvement. Even though the notable performance of this facility is undeniable, the fidelity of its test results can further be refined within specific test conditions. Take, for instance, low-speed tests investigating the behavior of an aircraft model at high angle-of-attack, where the complexity of the flow around the test article challenges the ability to obtain high definition results in such an important section of the aircraft performance envelope. In this context, it is worth the effort to explore how to enhance the current capabilities of the TWT to refine test results. The research project described by this

dissertation focuses on the improvement of wind-tunnel wall corrections at the NRC TWT, particularly when testing semispan models at low-speed.

## **0.1 History and background**

The history of the wind tunnel goes back to the numerous experiments carried out towards the end of the nineteenth century to try and understand aerodynamics. Before that, most of these experiments employed whirling arms, first used by Benjamin Robins to study basic geometries (Baals, 1981). A typical whirling arm would mount any given test geometry to its end, and when moved through still air in a centrifuge motion, one could study its aerodynamic behavior. Later on, Sir George Cayley also used a whirling arm to obtain the necessary test data to build a small glider, believed to be the first heavier-than-air vehicle to successfully fly.

It was not until the early 1900's when the first wind tunnels started to be commonly used by aeronauts. Wilbur and Orville Wright, in their quest to create their renowned aircraft, were forced to reject the existing aerodynamics handbook and trust their own data. The Wright brothers built a wind tunnel in 1901 with a simple design that allowed them to measure the relative lifting forces on a test article. The results encouraged the Wrights to build a bigger and more sophisticated wind tunnel with a 16-inch square section that provided them with all the necessary data to conceive their 1903 Wright Flyer.

After the Wright brothers' achievement in the United States, Europe closely followed by funding the construction of a series of major wind tunnels which led to a European technical leadership in aviation between 1903 and 1914. This is the reason why the two basic types of wind tunnels are named after European scientists. The open-jet version of the open-return wind tunnel also gets the name of Eiffel tunnel, after the French engineer Gustave Eiffel. The German aerodynamicist Ludwig Prandtl gave his name to the closed-return or Göttingen type tunnel.

In the following years, the construction of the US Navy wind tunnel in 1916 at the Washington Navy Yard and the tunnel built in Paris by ONERA in the early 1930's were the

most remarkable activities in the field. During World War II, Germany made significant progress in wind-tunnel technology by building at least three different supersonic facilities, one of them able to reach Mach 4.4 air flows. At the end of WWII, in 1946, France rebuilt an Austrian dismantled wind tunnel that still is operated today by ONERA as the world largest transonic wind tunnel. The US also built eight new wind tunnels, including the National Full-Scale Aerodynamics Complex (NFAC) at NASA Ames, currently the world's largest wind tunnel located in Mountain View, California.

The National Aeronautical Establishment (NAE), founded in 1951 and known today as the aerospace division of the National Research Council (NRC Aerospace), coupled with the construction of several wind tunnels, promoted Canada as a world-class aerospace nation. Motivated to develop high-speed aircraft like the Arrow program, the Canadian government built one of its most relevant testing facilities, the 5ft Trisonic Blowdown Wind Tunnel in Ottawa (Nelson *et al.*, 2004). Since becoming fully operational in 1963 (Ohman, 2001), this facility has hosted projects for clients such as Bombardier, the Department of National Defense (DND), NASA and other major airframers and research entities.

Since the emergence of computational fluid dynamics (CFD) at the end of the 1960s, the increasing role of numerical simulations has influenced the way wind tunnels are used in the aerospace design process. The advances in computational capabilities, development of new algorithms, and cost disparity between numerical and experimental techniques have favored an aggressive use of CFD, resulting in the reduction in wind-tunnel time for aircraft development programs (Chapman, 1979). Sources like the RAND report (Anton *et al.*, 2014) recognize CFD as a contributor to a reduction of about 50 percent of required wind-tunnel testing hours for applications such as transport aircraft tests at cruise conditions. Since 1980, NASA alone has closed over 20 wind-tunnel facilities (Malik and Bushnell, 2012). However, while reliable in typical cruise flow conditions, computational fluid dynamics (CFD) struggles to accurately predict separated flow regions for aircraft applications. For this and other complex flow applications, wind-tunnel testing continues to be the backbone of the aeronautical development process (Kraft, 2001). Today, the discussion needs to focus on how CFD and wind-tunnel testing can be integrated to increase productivity in aerospace design.

Although CFD is a useful tool for identifying options in the preliminary design of an aircraft, authors like Goldstein (2010) describe how wind tunnels are still needed to gather the data in situations where significant turbulent flow develops around complex geometries. A typical example of this synergy is the use of CFD in pre-test planning to optimize the use of the wind-tunnel facility. Additionally, computational methods can be used in parallel with experimental testing to assess and study wind-tunnel effects such as wall interference.

## **0.2 Scope and approach**

This section intends to serve as a guide to the contents presented in this dissertation. As briefly introduced before, this work studies how wind-tunnel wall corrections at the NRC TWT may be improved, particularly when testing semispan models at low-speed, and how experimental and numerical data can be used in combination to achieve this goal.

The first chapter will provide an overall perspective of important concepts to wind-tunnel testing like scale effects, flow similarity and wall interference. It will introduce the main factors that determine the relevance of wall interference, such as flow velocity or type test article, using them as a frame of reference to the considered research project. Then, the tools employed to rectify such interference will be described. In particular, the concept of wall corrections, their classification, computation techniques and specific wall-correction methods applied at relevant facilities will be reviewed. Special attention will be given to the one-variable method, the wall-correction method applied at the NRC TWT. At the end of this chapter, the problem statement addressed in this dissertation will be presented following a preliminary analysis of the one-variable method based on some available experimental data from the Bombardier Global 6000.

The primary goal of this research project is the update of the one-variable method, as it will be presented in the second chapter, together with the complementary secondary objectives that will be sought to contribute to that main goal. The methodology to achieve the desired results will be detailed in the third chapter. Details about the development of an offline test bench that was used throughout the entire research project will be also provided in this chapter. This offline tool efficiently computes wall corrections using the one-variable method

without the need to access and re-process wind-tunnel raw data. The three different model geometries employed during this research are the Bombardier Global 6000, the NRC NACA0012 Symmetrical Calibration Wing and the NASA Common Research Model (CRM); all of them in a half-model configuration. These models will be presented together with the particular applications given to the experimental data obtained using each of them as a test article. Special attention is given to the NASA CRM, for which both experimental tests and numerical simulations were performed. The methodology section will conclude by explaining how CFD results will be used to achieve the project goals and establishing the criteria to determine the validity of all the updates applied to the one-variable method.

The fourth chapter will present the results generated during the process of updating the wall-correction methodology. It will begin by studying the influence of several test parameters over an offset issue described as part of the problem statement. Then a CFD-based validation of the current wall-correction methodology as a whole, in the context of the criteria defined in the methodology chapter, will be presented. The results chapter will then propose an update to the potential theory representation of a semispan tunnel model's fuselage and wing, which will be validated using free-air CFD results for the particular case of the CRM at the NRC TWT. The advantages of using these updates will be gauged in terms of the overall improvement to the wall corrections. The fourth chapter will continue presenting wall corrections from an experimental data set using the CRM at the NRC TWT with a solid-wall test boundary that was corrected using free-air simulations of the same model in the same conditions. The end of the results chapter presents an application of the techniques applied in this project for tests performed in transonic flow conditions. Finally, the last chapter will review the work completed to validate and update the one-variable method and suggest some further advances that can be performed, particularly improvements to the methodology in transonic flow conditions at the NRC TWT.

## **CHAPTER 1**

### **LITERATURE REVIEW AND STATE OF THE ART**

The ultimate goal of testing a new aircraft at the preliminary design stage is to determine its operational limits and verify whether its original design specifications and requirements will be met at the production phase. At that final stage, the product will be a full-scale aircraft capable of flying within the desired operational envelope. In general, differences between test results obtained from a scaled aircraft model and a full-scale production aircraft ploughing through the sky can be attributed to scale effects. Rae and Pope (1984) focus on presenting scale effects as the differences that arise when the fluid dynamic dimensionless parameters are not the same in the experiments than in actual flight operation. Others like Bushnell (2006) reflect on other reasons for concern when scaling from wind-tunnel to flight, such as mounting effects, aeroelastic distortion, geometric fidelity or wind-tunnel walls, the latter being of great importance to this dissertation. In addition to presenting the scale effect problem, Blackwell (1982) introduces several ways to cope with the problem of wind-tunnel to flight Reynolds number disparity.

When it comes to the huge difference in terms of size between a scaled model and a full-scale aircraft, flow similarity plays a very important role to ensure the data obtained from the scaled test article is meaningful for the full-scale case. In general, flows around two differently sized models of the same flight vehicle are considered to be similar if Reynolds and Mach numbers can be matched (Anderson, 1984). Flow similarity is of great importance in wind-tunnel testing applications.

To ensure that the flow physics of a wind-tunnel model match those of its full-scale version, sufficiently high chord Reynolds numbers are usually required. This can be achieved in wind-tunnel testing by different strategies (Figure 1.1), such as using large scale models, pressurizing the tunnel to run tests above atmospheric pressure (higher pressure means higher fluid density according to the equation of state) or resorting to a cryogenically cooled test

medium to benefit from the advantageous properties of gases at low temperature (lower viscosity, higher density and lower speed of sound) described by authors like Kilgore *et al.* (1974). Another possibility to obtain higher Reynolds numbers is to play with the viscosity parameter by operating the wind-tunnel exchanging fluids between the actual and the test conditions, for instance, using nitrogen or water instead of dry air.

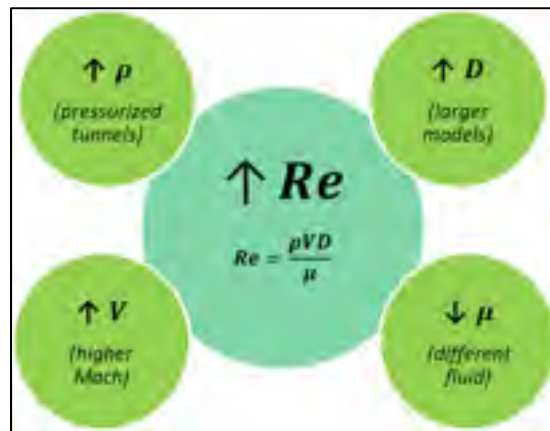


Figure 1.1 Different approaches to obtain high Reynolds number by adjusting wind-tunnel testing parameters

The use of higher than full-scale test velocity is also an option to reach high Reynolds numbers. This allows using smaller scale models in wind tunnels where model size is a constraint. Of course this may affect the similarity of the flow since the Mach number is not matched anymore. However, for low Mach number applications this is less critical (Katz and Plotkin, 2001), provided assumptions like incompressible flow (discussed later in this chapter) are not violated.

In addition to considering flow similarity to deal with scale effects, a scaled model tested in a wind tunnel also experiences the influence of the test section walls. In a very simple way, wall interference may be described as the difference between the wind-tunnel flow field and its free-air counterpart (Figure 1.2). Wall interference is a test section specific bias error in wind-tunnel test data.



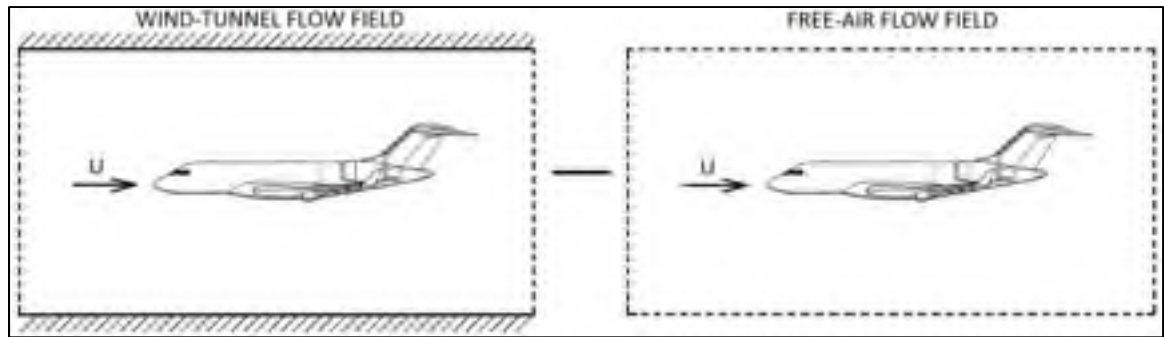


Figure 1.2 Wall interference described as the difference between the wind-tunnel and free-air flow fields.

This interference originates from the longitudinal static pressure gradient in the tunnel test section and along its boundaries, which produces a series of forces that need to be subtracted out. In order to rectify this phenomenon and obtain the aircraft free-air behavior, wall interference must be calculated and a series of wall corrections must be applied.

## 1.1 Main factors of aerodynamic interference in wind-tunnel testing

As part of the Advisory Group for Aerospace Research and Development report published in 1998 (AGARDograph 336), Krynytzky and Hackett consider that the severity of wall interference is driven by several factors including (1) flow speed, (2) type and size of the test article, (3) type of test section walls and, in general, (4) the nature of the aerodynamic forces generated by the test article. This section will discuss each of those factors.

### 1.1.1 Flow speed

As previously introduced, flow similarity needs to be ensured to correlate scaled model test results to full-scale. In wind-tunnel testing applications, Mach and Reynolds numbers are the most relevant correlation parameters to consider. If testing at low-speed, the Mach number dependence of the governing equations of fluid dynamics is small enough to be neglected.

Aside from high-lift (take-off/landing) configurations, this is generally considered to be the case for Mach numbers lower than 0.3, where the principles of low-speed aerodynamics are generally applicable.

### Low-speed aerodynamics

At low-speed Mach, the Reynolds number becomes the main parameter of interest for similarity and the flow is considered to be incompressible. For incompressible flows, density  $\rho$  is considered to be a constant. When this constant density condition is applied to the continuity equation, the outcome is that the divergence of the flow velocity field is zero, as seen in Eq. (1.1).

$$\frac{\partial \rho}{\partial t} + \nabla \cdot (\rho \vec{V}) = \nabla \cdot \vec{V} = 0 \quad (1.1)$$

Additionally, if the flow viscosity  $\mu$  is low enough to be considered to be zero, the Reynolds number will be infinite and the flow can be considered inviscid. In an inviscid fluid, irrotational motion is permanent (Milne-Thomson, 1966). An irrotational flow around a streamlined body has zero vorticity or, what is the same, the curl of the velocity field is zero ( $\nabla \times \vec{V} = 0$ ). From vector analysis, a vector with zero curl must be the gradient of a scalar function. In the case of the velocity field  $\vec{V}$ , that scalar function is called velocity potential  $\phi$ , where  $\vec{V} = \nabla \phi$ .

Therefore, for low-speed irrotational flows, the Laplace equation, Eq. (1.2), is satisfied and may be derived as follows.

$$\nabla \cdot \vec{V} = \nabla \cdot \nabla \phi = \nabla^2 \phi = \Delta \phi = 0 \quad (1.2)$$

In summary, for an inviscid, irrotational flow, the velocity field  $\vec{V}$  is the gradient of the velocity potential  $\phi$ . This velocity potential is also known as potential flow. If the flow is also incompressible, the velocity potential satisfies the Laplace equation ( $\Delta \phi = 0$ ) and potential theory may be applied (Rae and Pope, 1984). All these concepts will be relevant for the use of potential theory.

### *Potential theory*

Low-speed inviscid flows around streamlined bodies, like the ones investigated in this research project, may be represented by means of singularities (fundamental solutions) of the Laplace equation. The discipline that studies how to combine those singularities into a potential flow  $\phi$  model is called potential theory.

Based on their particular application, most potential flow models employ complex combinations of basic singularities such as sources, sinks and vortices (Figure 1.3) to represent the lifting and non-lifting effects of the streamlined body. The non-lifting effects, known as blockage effects, are a combination of the contribution of the body's volume and wake. Authors such as Krynytzky and Ewald (1998) approach the use of different singularities and singularity-distributions to best represent the flow around the specific geometry studied.

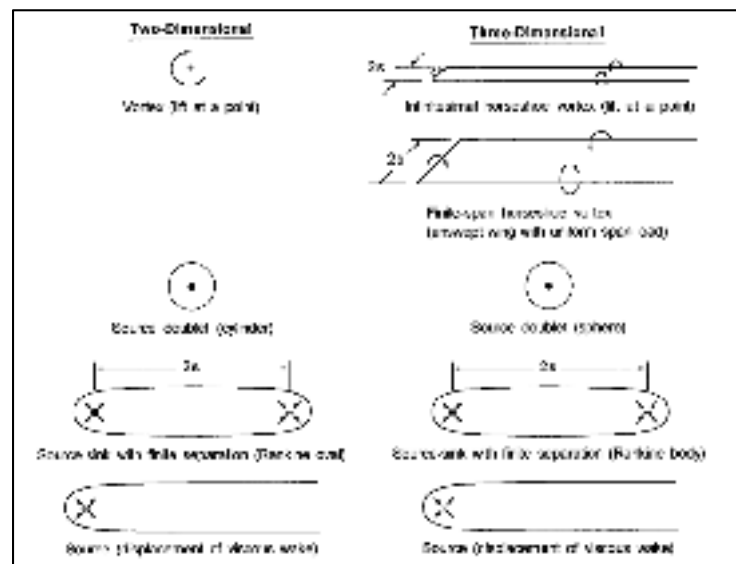


Figure 1.3 Elementary singularities of the Laplace equation in potential flow models. From: Krynytzky and Ewald in AGARDograph 336 (1998).

As noted by Hackett *et al.* (1979), in general, volume effects (solid blockage,  $\epsilon_s$ ) can be represented by a distribution of point doublets (source-sink pairs) and wake effects (wake blockage,  $\epsilon_w$ ) can be represented by sources. Additionally, lifting effects can be represented by horseshoe vortices or semi-infinite line doublets, as presented by Ulbrich (1998).

All levels of complexity may be achieved by combining different singularities into a specific potential flow model. A simple body of revolution may be modelled with just a source and a sink located at a distance from each other. Figure 1.4 shows an example of a simple array of singularities used by Iyer and Everhart (2001) to represent the flow around an aircraft wind-tunnel model tested at NASA Langley. More complex geometries may be modelled using potential theory. As Rae and Pope (1984) indicates, the use of the currently available computing technology allows models to be made up of thousands of singularities.

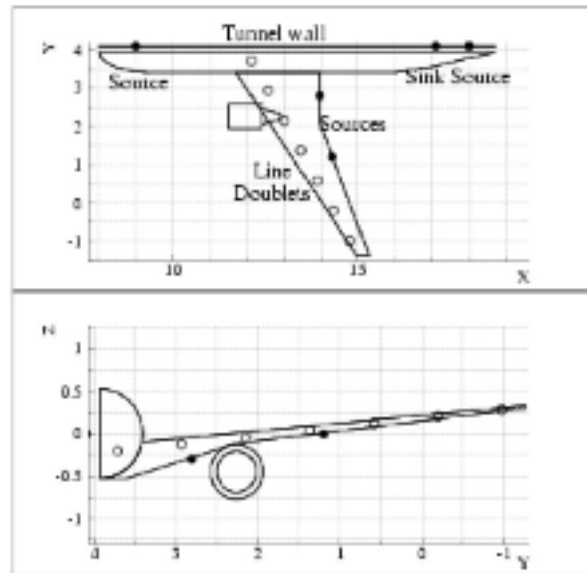


Figure 1.4 Example of a potential theory representation for an aircraft wind-tunnel model. From: Iyer and Everhart (2001).

Once the potential flow model  $\phi(x, y, z)$  around a specific streamline body has been defined, the velocity components, Eq. (1.3), may be obtained by derivation.

$$u = \frac{\partial \phi}{\partial x}; v = \frac{\partial \phi}{\partial y}; w = \frac{\partial \phi}{\partial z} \quad (1.3)$$

The use of potential theory is paramount to some of the wall-correction methodologies applied at different wind tunnels, which is why it is key for this entire dissertation. When flow viscosity is not an issue or when dealing with thin boundary layer, a detailed potential flow model can provide a proper representation of the flow behavior around a flying vehicle in free-air.

### *Viscous effects*

Unfortunately, potential theory is not applicable in all circumstances. For instance, wind-tunnel tests at low-speed Mach numbers and high incidence, typical of take-off and landing conditions, generally experience the additional challenge of the development of flow separation over the test article. These conditions result in zones experiencing significant adverse pressure gradients where complex separated flows with high viscosity and vorticity develop. The significant viscous forces and the vorticity void the inviscid and irrotational flow conditions assumed for the low-speed aerodynamic scenarios discussed so far. Consequently, when significant flow separation is present, the traditional use of potential theory as a tool to obtain solutions of the flow behavior is not valid.

The effects of flow separation over streamlined bodies include increased drag as well as a reduction of the pressure differential, resulting in reduced lift. Hoerner (1975) highlights the importance of investigating the stall properties of an aircraft and its relationship to relevant design variables such as aspect ratio, sweep angle, load distribution or planform. The ability to provide accurate results in stall conditions, where flow separation is significant, is paramount in the preliminary design phase of any aircraft.

### 1.1.2 Wind-tunnel models

At the beginning of this chapter, the necessity to obtain high enough Reynolds numbers to guarantee flow similarity when testing scaled models at low-speed was introduced. The use of larger scale models has been presented as a solution to this problem. A complementary technique for reaching higher chord Reynolds numbers at a given test facility is the use of semispan or half-models mounted on a solid plate over one of the tunnel walls, instead of full-span models mounted to a strut. Franz (1982) discusses in detail the application of half-models in wind-tunnel testing, as well as its benefits and drawbacks. Although semispan wind-tunnel models allow reaching the desired high Reynolds numbers, their larger size with respect to the tunnel cross section and proximity to the tunnel boundary accentuates the wall-interference effects.

#### Semispan models

Using the semispan or half-model approach allows for the building of larger scale models (Figure 1.5), which can easily fit the measuring instrumentation needed in the model for wind-tunnel testing such as pressure taps or balances. Additional advantages when using half-models include lower construction cost, compared to full-span models, and higher model geometric fidelity.

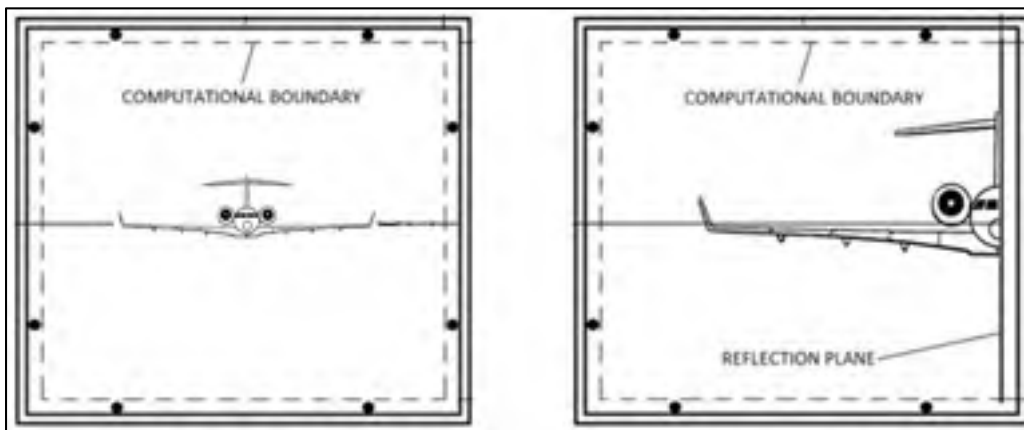


Figure 1.5 Sketch of a full-span model (left) and a semispan model (right) of an aircraft in the same test section. Notice the higher model span-to-tunnel width ratio for the semispan case.

Unfortunately, their main disadvantages are a large wall-interference effect compared to full-span testing and the effects of the side-wall boundary layer over the attached half-fuselage, which can be minimized by using splitter plates or standoffs, as pointed out by authors like Blackwell (1982) or Gatlin *et al.* (1997), to relocate the model at a distance where better flow quality can be provided. The severity of wall-interference effects experienced in half-model tests is related to the larger model size to test section size ratio (larger models are unavoidably closer to the tunnel walls) and must be rectified by applying wall-interference corrections.

Ultimately, wind-tunnel results using both full-span and semispan models should correlate when the data are adequately corrected for interference, as proved by authors like Gross and Quest (2004).

### **1.1.3 Wind-tunnel design**

Every wind tunnel has some distinctive and unique features that make it capable of attaining the specific flow conditions required for the testing it is designed to host. In general, all of them may be classified in terms of tunnel and test section types. There are two basic types of wind tunnels, open circuit and closed circuit (Rae and Pope, 1984). For each of them, their test section may be open, partially open (perforated or slotted-wall) or closed.

Aside from that general classification, special consideration must be given to minimizing problems derived from wall interference when selecting a particular wind tunnel for an experiment, as presented by Blackwell (1982). Some wind-tunnel test sections may be designed to minimize the wall-interference effect. That is the case of test sections with adaptive walls or boundary layer suppression/ingestion technology. Other facilities may also rely on post-processing their data by using some kind of wall-interference correction method, like the ones that will be introduced later in this chapter. For a specific wind tunnel, all of

these features make the test article more or less sensitive to wall interference. The National Research Council 5ft Trisonic Wind Tunnel, where wall interference is minimized by both the design features of its test section and by data correction, is the tunnel considered in this dissertation.

*The National Research Council 5ft Trisonic Wind Tunnel*

Located at the Uplands Road facilities in Ottawa, the NRC 5ft tunnel (Figure 1.6) is an open-return tunnel of the blow-down type. Unlike regular open-return wind tunnels, where air is drawn through the tunnel by suction, blow-down wind tunnels are a special kind of open return tunnels that operate by blowing air downstream for short periods of time. The Mach number range in this tunnel goes from low subsonic at 0.1 to a maximum of 4.25 (Ohman, 2001).



Figure 1.6 Overview of the NRC 5ft Trisonic Wind Tunnel.

The tunnel 8.4 MW (11,250 hp) compressor plant is used to charge the storage tanks with 40 tons of dry air at 21 atm and 21°C. When initiating a run, the control valve opens and the air flows through the settling chamber where a series of flow stabilizing devices, noise



attenuating devices and turbulence damping screens ensure quality air flow before it goes through a flexible nozzle that supplies air up to 17 atm to the closed 5ft by 5ft square test section, surrounded by an enclosed plenum. Finally, the air flow goes through a diffuser, a silencer and an exhaust where it is extracted at atmospheric pressure. Although run times are dependent on test conditions, a typical run can last about 20 seconds then taking around 20 minutes to recharge the air tanks. As described in Elfstrom *et al.* (2001), this facility has the capability of operating using the abovementioned 5ft by 5ft test section for 3D testing or a 1.25ft by 5ft test section for 2D testing, easily interchangeable thanks to its “roll-in roll-out test section system”. Only operation in the 3D test section will be considered for the remainder of this dissertation.

In order to perform tests with a partially-open boundary, the 3D test section walls are perforated by 0.5 inch diameter holes inclined  $60^\circ$  toward the oncoming flow (Figure 1.7) and equipped with splitter plates for edge tone suppression (Dougherty *et al.*, 1976). During ventilated-wall tests, the porosity in the walls can be adjusted from 0.5% to 6% by an external throttle plate. Porosity (or other forms of partially open boundary) is a necessity for transonic testing (Rae and Pope, 1984); it prevents choking at the near-sonic Mach numbers and prevents shock and expansion wave reflections at the low supersonic Mach numbers. At this facility, low-speed testing is also performed with the perforated boundary. A 1.5% porosity configuration is typically selected to (passively) reduce the wall interference. The use of the perforated test section with its complicated cross flow characteristics rules out the use of the standard textbook correction techniques. Solid-wall tests can also be performed in the test section on an ad hoc basis by appropriately taping the test section wall perforations, as first tested by Broughton (2013). Within this project, both solid-wall and ventilated-wall tests will be considered in subsonic flow conditions.

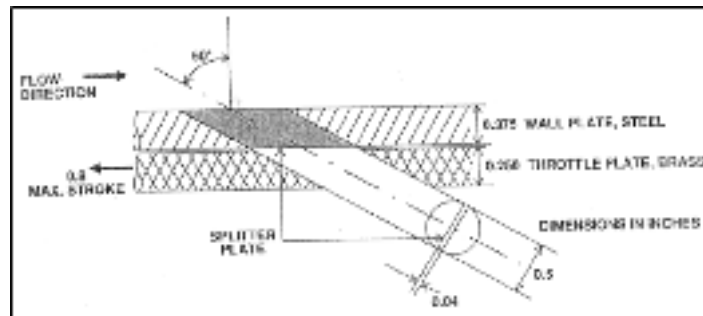


Figure 1.7 Detail view of the wall perforations in the NRC 5ft wind-tunnel test section.

This research will study the wall interference on half-model tests at subsonic flow. For half-model tests, the model is mounted on a solid plate (reflection plate) covering one of the side walls, hereafter the “north” wall, with a splitter plate on its upstream edge. The interaction of the reflection plate boundary layer with the flow over the fuselage is minimized by the use of a filler plate that creates an appropriate stand-off distance from the reflection plate. Unlike other facilities like the NASA Ames 11ft Transonic Wind Tunnel (TWT), where pressure orifices are directly drilled at the test section boundary (Boone and Ulbrich, 2002), NRC 5ft TWT uses six pressure rails located along the test section on the ceiling, floor and south walls to measure the static pressure. These measurements are needed to determine the wall interference (Mokry, 2006). The layout of the six pressure rails can be observed on Figure 1.8.

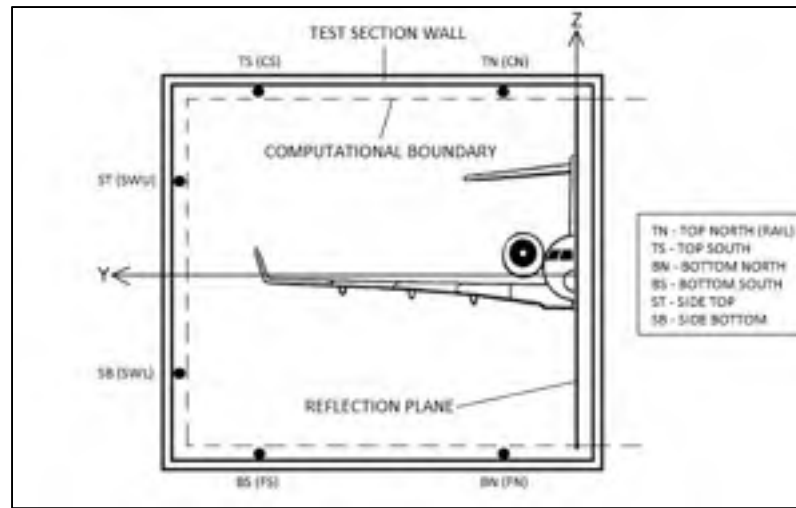


Figure 1.8 Layout of the reflection-plate and pressure rails in the NRC 5ft wind-tunnel test section.

A six-component sidewall balance is used to measure overall forces and moments relative to the model axis. The balance is installed on the north side of the wind tunnel, supported between bearings in the test section wall and the plenum shell. The balance incidence drive motor and gearbox assembly are mounted outside the plenum. Balance excitation and sampling frequency is typically set to 10 volts and 100 Hz, respectively.

#### 1.1.4 Nature of the wind-tunnel test

Consider a given flow speed, test section design and test article. Even in these somewhat fixed conditions, not all wind-tunnel tests are equally sensitive to wall interference. For instance, wind-tunnel tests simulating low-speed take-off, approach and landing conditions experience more complex flows that require accurate wall corrections.

To allow this section to serve as a recapitulation, this project will involve low-speed wind-tunnel tests using the semispan model of a transport aircraft mounted in the NRC 5ft

TWT with a solid-wall test section boundary. Even with all these parameters defined; the effect of wall interference will still depend on other test variables such as the model incidence.

These factors indicate that considerable wall interference will be experienced. This interference needs to be rectified through the use of wall corrections.

## **1.2 Wind-tunnel wall-interference correction**

In a wind tunnel, the distance of the test section boundaries relative to the test article may cause an effect over the flow properties, such as flow speed or angularity (Rae and Pope, 1984). To ensure an accurate description of wind-tunnel data, the interference generated as a consequence of the presence of the tunnel walls must be understood and rectified using wall corrections. Properly corrected data can then be compared to data from different tunnels or to a free-air situation.

Publications like AGARDograph 109 (1966) and ESDU 95014 (1995), which have their foundations in the work of Glauert (1933) and other aerodynamicists that investigated boundary interference in the 1920s and 1930s, may serve much like a handbook to determine wall corrections even before the wind-tunnel test is executed. These corrections will often be referred to as “textbook”, “handbook” or “theoretical” corrections in this dissertation. These textbook corrections rely on assumptions like idealized boundary conditions and apply traditional techniques like the method of images; requiring model and tunnel geometry, measured lift and drag values (or estimated values).

When the test section boundaries have properties that cannot be modeled simply (e.g. porosity) or flow complexity is significant, textbook corrections are typically replaced with methods that include additional experimental flow measurements at the boundary, like those developed by Ashill (1993), Ulbrich (1998) or Mokry (1987); introduced later in this chapter. These methods are not limited to any particular wall boundary condition, so they can also be used with solid-wall boundaries.

The different types of wall corrections, as well as the available tools to help calculate them will be introduced in this section.

### 1.2.1 Classification of wall corrections

Wall corrections are categorized (Table 1.1) as presented by Garner in AGARDograph 109 (1966). First order corrections consider the most important wall-interference effects that can be addressed by blockage and incidence corrections. These corrections are given as a mean adjustment to Mach number and the angle of attack at a specific reference point, required for the model aerodynamics measured in the test section to be transferable to a “free-air” situation. Higher-order methods may be calculated to provide the gradients of the corrections over the entire test article, as described by Taylor and Ashill in AGARDograph 336 (1998).

#### *A. First-order corrections – Blockage and incidence corrections*

Blockage corrections try to compensate the volume (solid blockage) and wake (wake blockage) effects of the test article confined in the wind-tunnel test section. Solid blockage is the result of the interaction between the test section boundaries and the physical volume of the test article. In other words, it is the effect of the test section boundaries altering the distance between the streamlines in the vicinity of the test article compared to a free-air situation. In closed-jet wind-tunnels, this forces the air to flow through a smaller area as compared to a free-air scenario, which increases the air velocity around the model (Maskell, 1963). Wake blockage is caused by the wake generated by the test article, where the mean velocity is much lower than the free stream. In a closed tunnel, this results in an altered flow velocity and pressure around the model, which needs to be rectified.

Blockage corrections are represented by the blockage factor  $\epsilon$ , Eq. (1.4), which is the ratio between the axial velocity increment due to the tunnel walls  $\Delta U$  (or interference axial

velocity  $u_I$ ) and the flow reference velocity  $U$  (Rae and Pope, 1984). Corrections for dynamic pressure  $\Delta q$  and Mach number  $\Delta M$  can be obtained from the blockage factor, as seen in Eqs. (1.5) and (1.6). The magnitude of blockage corrections can be related to the type of wind-tunnel test section boundary considered. In solid-wall tests, blockage corrections generally have greater values than in ventilated-wall tests. In addition, the sign of blockage corrections is positive in solid-wall tests and typically negative in ventilated-wall tests.

$$\epsilon = \frac{u_I}{U} \quad (1.4)$$

$$\Delta q = q(1 + \epsilon)^2 \quad (1.5)$$

$$\Delta M = \left[ \left( 1 + \frac{\kappa - 1}{2} M^2 \right) \epsilon \right] M \quad (1.6)$$

The flow angle on the model is also influenced by the presence of the tunnel walls; therefore the angle of attack needs to be corrected using incidence corrections. Different formulae to calculate the incidence correction may be derived for specific test section geometry, as explained by Garner (1966). In general, the angle of attack correction  $\Delta\alpha$  is obtained as a function of the interference upwash velocity  $\Delta w$  (or  $w_I$ ) and the tunnel reference velocity  $U$  at a given reference point in the test article (Krynytzky and Ewald, 1998), as seen in Eq. (1.7). For positive lift, the angle of attack correction is positive in solid-wall tests and usually negative for ventilated test sections.

$$\Delta\alpha = \frac{w_I}{U} \quad (1.7)$$

### ***B. Higher-order corrections***

Depending on the client's test goals, higher-order corrections may be applied to wind-tunnel test data as a function of the first-order corrections. Higher order corrections, such as pitching moment corrections  $\Delta C_M$  or buoyancy drag corrections  $\Delta C_D$ , take into account the fact that first-order corrections are not constant at different points on the model. Pitching moment corrections for a wing may be calculated as a function of the spanwise or chordwise variation

of the angle of attack. Buoyancy drag corrections can be computed as a variation of the blockage factor along the fuselage (Taylor and Ashill, as part of AGARDograph 336, 1998).

Table 1.1 Classification of wall corrections.

<b>FIRST-ORDER CORRECTIONS</b>	<ul style="list-style-type: none"> <li>• <u>Rectify</u> most important effects of wall interference.</li> <li>• Calculated at selected reference point.</li> <li>• Blockage (<math>\Delta q</math> and <math>\Delta M</math>) / Incidence (<math>\Delta\alpha</math>)</li> </ul>
<b>HIGHER-ORDER CORRECTIONS</b>	<ul style="list-style-type: none"> <li>• <u>Rectify</u> first order variation effects throughout the model.</li> <li>• <math>\Delta C_M</math> or <math>\Delta C_D</math> are common examples</li> </ul>

As a visual example, let's consider the illustration in Figure 1.9, where the angle of attack correction for a certain aircraft model in a wind tunnel is plotted on a XY plane. Typically, the wind-tunnel client would receive first order corrections, i.e., blockage and incidence corrections, at a specified reference point. Additionally, the client could request higher-order corrections such as pitching moment correction  $\Delta C_M$  based on the variation of  $\Delta\alpha$ .

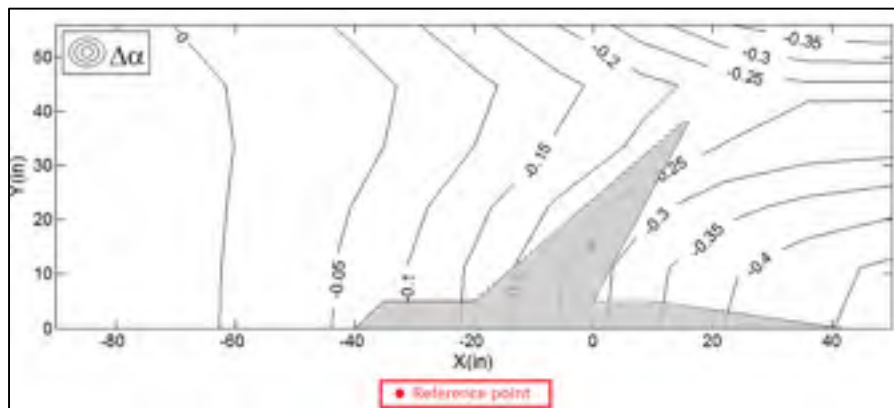


Figure 1.9 Contour plot showing the variation of the angle-of-attack over a tunnel model to illustrate the concept of first and higher order corrections.

### 1.2.2 Wall-correction calculation techniques

The effect of wall interference on a model tested in a wind tunnel may be calculated using three different approaches for wall-correction computation techniques. All of them require the exact location of the model in the test section as well as information about the test section boundary conditions.

#### *A. Analytical techniques*

Analytical techniques apply potential theory to compute wall interference. They are based on solutions of the linearized potential equation of the wall-interference flow field (Milne-Thomson, 1966), Eq. (1.8), where  $\phi_I$  is the interference velocity potential near the walls.

$$(1 - M)^2 \frac{\partial^2 \phi_I}{\partial x^2} + \frac{\partial^2 \phi_I}{\partial y^2} + \frac{\partial^2 \phi_I}{\partial z^2} = 0 \quad (1.8)$$

By introducing the compressibility factor  $\beta$  of Eq. (1.9) and applying the Prandtl-Glauert transformation, Eq. (1.8) becomes the Laplace equation and potential theory may be applied. At low-speed tests,  $\beta$  is expected to be close to one.

$$\beta = \sqrt{1 - M^2} \quad (1.9)$$

Given that the wall interference is a “far-field” effect (Mokry, 2006), a priori it is not necessary to represent in detail the test article geometry and singularities of the Laplace equation such as sources, sinks or doublets can be used to represent the model. Analytical techniques include the method of images, which can be applied to wind tunnels with rectangular solid-wall test sections.

#### *Method of images*

Previously in this chapter, the use of potential theory to represent the unbounded flow around a streamlined body was introduced. However, there are times when the flow around that body is disturbed by a nearby boundary.



Assuming a wind tunnel has a constant rectangular cross section extending far enough both upstream and downstream from the model and provided that the nearby boundary satisfies the no-flow-through condition, like in the case of a model tested in a wind tunnel with a solid-wall test section, it is appropriate to apply analytic techniques such as the method of images as described by Krynytzky and Ewald in AGARDograph 336 (1998). In wind tunnels where the model is located on the centerline of the test section, symmetry conditions can help simplify the analysis and determine the interference velocity and, by extension, wall-interference corrections.

Historically, wind-tunnel wall interference is taken into account by using potential theory method of images suitably arranged for the test section geometry and boundary conditions. By applying this method, the flow field created by certain singularities in the vicinity of a solid boundary can be simulated by superimposing mirror image singularities; this guarantees that there is no flow in the symmetry plane at the actual boundary location (Kuethe and Chow, 1986).

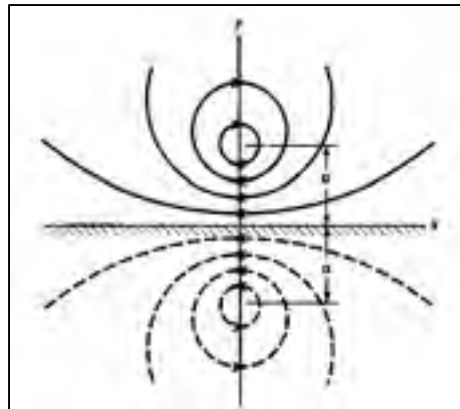


Figure 1.10 Vortex near a solid boundary and image vortex placed to guarantee the no flow through condition. From: Kuethe and Chow (1986).

For example, consider a vortex of strength  $\Gamma$  at distance  $a$  from a solid boundary like the one represented in Figure 1.10, located at  $(0, a)$ . By placing another vortex of opposite strength  $-\Gamma$  at a symmetrical location with respect to the boundary, i.e.,  $(0, -a)$ ; the normal component of the velocity would be cancelled at the wall.

As explained by Krynytzky and Ewald, the method of images may be applied to wall-interference calculations by developing a set of image singularities required to represent all the wall surfaces of a given test section and adding their effect to determine the interference on the model. As depicted by Figure 1.11, for 3D model (or half-model) testing in rectangular test sections, the image system is doubly infinite because of mutual interference of vertical and horizontal walls, which require images along the diagonals (Rae and Pope, 1984).

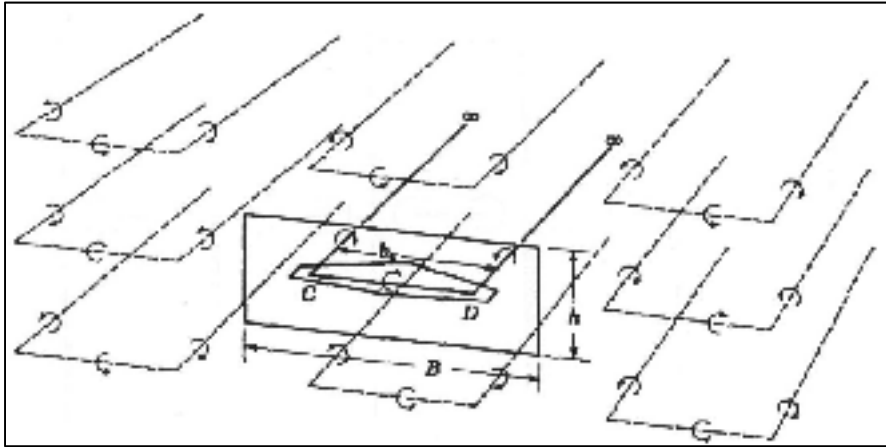


Figure 1.11 Illustration of the method of images: Image system for a wing in a closed rectangular tunnel. From: Rae and Pope (1984).

### ***B. Numerical techniques***

Numerical techniques allow representing more complex model and test section geometries. These techniques use tools like panel codes to obtain the wall-interference flow. The wall-interference flow field is calculated by taking away the free-air flow field of the test article from the computed solution obtained in the wind tunnel.

### Panel codes

For wind-tunnel testing, the current computational resources can create complex singularity models to represent a test article in a specific test section, including its walls. For this kind of problem, panel methods allow modelling a solution for the inviscid, irrotational flow under study using singularities of the Laplace equation (Erickson, 1990). Those singularities are distributed over small quadrilateral panels placed over the test article surface. If the singularities employed by a panel method are sources or doublets, it may simply be called source-panel method or doublet-panel method. As mentioned, test section boundaries may also be represented using panel methods, satisfying the boundary conditions at a finite number of points at the wall.

Publications like Cebeci et al. (1989) show how panel methods may be used to represent more complex configurations. Katz and Plotkin (2001) show an example of the discretization of the geometry of the three-dimensional body of a combat aircraft using a panel representation (Figure 1.12).

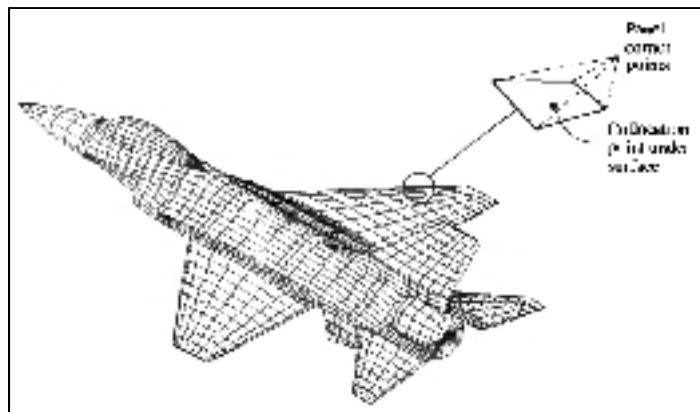


Figure 1.12 Example of a discretization of the geometry of a three-dimensional body using a panel representation with constant-strength surface doublets and sources. From: Katz and Plotkin (2001).

### ***C. Combined techniques***

Both analytical and numerical techniques are generally valid in wind-tunnel tests where flow separation is expected to be small and boundary conditions are somewhat simple. In any other case, combined techniques can be contemplated as an alternative.

These techniques combine wall boundary measurements with analytical solutions of the subsonic potential equation to calculate the effect of wall interference. In separated flow conditions, these techniques can match the measured wall-signature on the test section boundary with numerical solutions to calculate the wall corrections. This kind of techniques will be discussed in detail in the next section, considering three main wall-correction calculation methods: the one-variable method developed by Mokry *et al.* (1987), the wall-signature method developed by Hackett *et al.* (1979) (and its modifications performed by Ulbrich in 1998) and the two-variable method developed by Ashill *et al.* (1993).

### **1.2.3 Wall-correction methods**

Many wind tunnel facilities have implemented wall-correction methods that use flow measurements in the vicinity of the test section boundary. The major existing wall-correction methods are presented below.

#### ***A. One-variable method***

Capelier, Chevallier and Bouniol established in 1978 in ONERA what would be the grounds of what is known today as the one-variable method as an alternative for the existing textbook methods using traditional boundary conditions, which were unable to provide acceptable solutions for ventilated-wall or adaptive-wall wind-tunnel tests. This was the case with commonly used techniques that usually assumed idealized fully-open or fully-closed boundary conditions. As an example of these traditional techniques, the method of images can be used to obtain a solution of the flow around a model in a tunnel provided constant rectangular cross section and solid or open wall (free jet) boundaries assumptions can be made. One of the main innovations of this new method used by ONERA was the use of direct

measurements of the flow velocity in the test section walls, eliminating the uncertainties of previously used techniques. At the time, the velocities measured at the walls were compared to those due to the model, calculated by means of singularities in unlimited flow. This method was applied in the ONERA S4LCh adaptive-wall wind tunnel and the R1Ch ventilated-wall wind tunnel at subsonic flow.

In 1985, Mokry continued the trend to develop correction methods that use boundary flow measurements. In an effort to further develop the ability to accurately calculate wall corrections, Mokry developed the one-variable method, which also employed boundary measurements and numerical processing.

Among the innovations of Capelier *et al.*, was the calculation of wall corrections in a finite-length test section. This method is currently applied at the NRC Trisonic Blowdown Wind Tunnel to calculate the wall interference based on a combination of classical potential theory and panel methods. It requires (1) the measurement of one flow variable, the streamwise component of the flow velocity, on the test section walls and (2) a singularity representation of the wind-tunnel model.

At subsonic flow, the velocity potential  $\phi$  near the tunnel walls can be represented by the linearized subsonic equation, Eq. (1.10).

$$(1 - M^2) \frac{\partial^2 \phi}{\partial x^2} + \frac{\partial^2 \phi}{\partial y^2} + \frac{\partial^2 \phi}{\partial z^2} = 0 \quad (1.10)$$

In order to represent the compressibility effects in the tunnel, the Prandtl-Glauert transformation is used by applying the compressibility factor  $\beta$ , Eq. (1.9), to scale the axial coordinate  $\xi$ . As a result, the Laplace equation is obtained, Eq. (1.11).

$$\frac{\partial^2 \phi}{\partial \xi^2} + \frac{\partial^2 \phi}{\partial y^2} + \frac{\partial^2 \phi}{\partial z^2} = 0 \quad (1.11)$$

$$\xi = x/\beta \quad (1.12)$$

The velocity potential near the walls can be expressed as the superposition of its component due to wall interference  $\phi_I$  and its component at free-air conditions  $\phi_F$ .

$$\phi = \phi_F + \phi_I \quad (1.13)$$

The application of the one-variable method to the National Research Council Trisonic Wind Tunnel will be thoroughly explained later in this chapter. Other research institutions like JAXA in Japan have also implemented Mokry's one-variable method in their facilities as their wall-correction methodology, as can be verified following the work of Kohzai *et al.* (2013).

### ***B. Wall-signature method***

Very much like the one-variable method, the wall-signature method considers the linearized potential equation, taking into account compressibility effects for a subsonic wind-tunnel flow field by using the Prandtl-Glauert transformation. This method also employs a singularity representation of the model, satisfying the Laplace equation, as well as a panel method.

The wall signature method was originally developed by Hackett *et al.* in 1979 as a result of the need of a blockage correction method for the solid-wall Lockheed-Georgia 16¼ft x 23¼ft wind tunnel. It was able to estimate both solid and wake blockage for a three-dimensional model from the analysis of the tunnel wall pressure signature. Wall pressures were used to determine the strength, span and location of sources and sinks on the tunnel centerline representing a body outline equivalent to a simple test article and its wake. In order to locate the singularities representing the model, Hackett took a local least squares fit approach in his method. He introduced a piecewise approximation of the measured wall signature using a parabola for its maximum and a tanh-function for its downstream asymptote. The location of the singularities was found by matching the location of the maximum value of the parabola with the inflection point of the tanh-function. This methodology required the selection of

specific pressure ports as part of its tedious local least squares fit, which complicated its ability to be used in real-time tests. In a review of this method, Hackett *et al.* (1980) used multiple singularities at fixed locations (in lieu of determining their position based on the wall signature) and included the capability to calculate incidence corrections.

Due in part to the abovementioned limitations for the application of Hackett's method in real-time tests, in 1998, Ulbrich developed a modified version of the wall-signature method to be implemented in the Wall Interference Correction System (WICS) of the NASA Ames 12ft Pressure Wind Tunnel (PWT), able to compute wall-interference effects in real-time subsonic wind-tunnel testing of both full-span and semispan models.

In this updated method, Hackett's local least squares fit of the measured wall signature is replaced by a global least squares fit, matching the wall signature on all pressure ports using panel method code solutions of singularities placed inside the wind-tunnel test section. The panel method code used in Ulbrich's 1998 methodology allows the application of the Laplace equation to a three-dimensional representation of the quasi-octagonal cross-section of the solid-wall test section of the 12ft PWT, with a quasi-octagonal cross-section. To calculate first order corrections at the 12ft PWT, the wall-signature method requires a model representation and a least squares fit of the measured tunnel wall signature, together with balance forces from the model, calibration test data and pre-computed solutions of the subsonic potential equation.

As a continuation of Ulbrich's work on the Wall Interference Correction System (WICS) for the 12ft Pressure Wind Tunnel, a real-time wall-interference correction system (TWICS) was conceived by Ulbrich and Boone (2001) for the NASA Ames slotted-wall 11ft Transonic Wind Tunnel (TWT). This system was later implemented at NASA Langley 14x22ft Subsonic Tunnel (Iyer *et al.*, 2003).

Figure 1.13 shows a half model mounted on a finite-length reflection plate over the floor of the 12ft PWT test section, amongst a distribution of pressure measurement rows. Additionally, a panel representation of the test section and its mirror image with respect to the reflection plate is also shown.

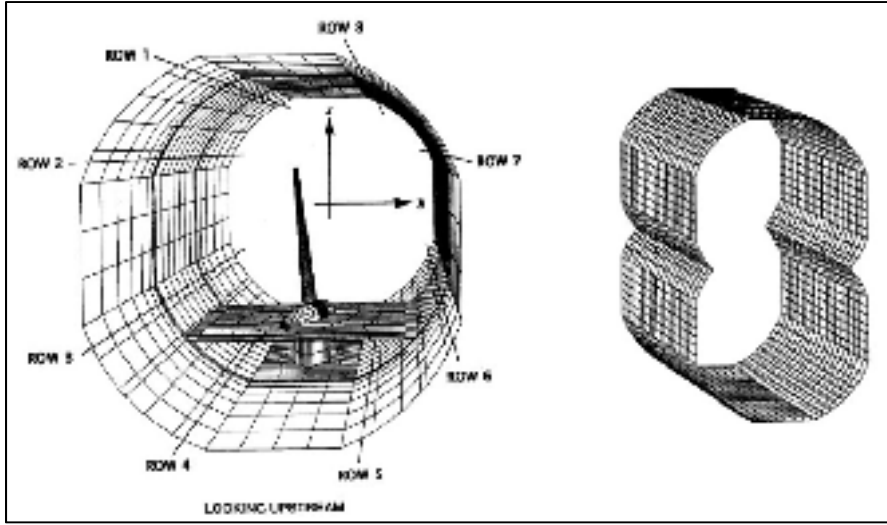


Figure 1.13 NASA Ames 12ft PWT test section interior and paneling. From: Ulbrich (1998).

Inspired by Keller's (1972) panel method algorithm, Ulbrich (2000) developed the panel method code ANTARES for wind tunnels with constant cross-section, which was integrated in an updated version of the WICS. One of the innovations of this improved methodology is the ability to customize the subsonic potential equation for different wind-tunnel wall boundary conditions such as solid wall, open jet, perforated wall, etc. Different boundary conditions can be represented by selecting different sets of constants  $c_1$ ,  $c_2$ ,  $c_3$  and  $c_4$  (Ulbrich, 2002), as applied in Eq. (1.14). For instance, a solid-wall boundary condition would be represented by applying  $c_1=c_2=c_4=0$  and  $c_3=1$  (see Table 1.2).

$$c_1 \cdot \phi + c_2 \cdot \frac{\partial \phi}{\partial x} + c_3 \cdot \frac{\partial \phi}{\partial \vec{n}} + c_4 \cdot \frac{\partial^2 \phi}{\partial x \partial \vec{n}} = 0 \quad (1.14)$$



Table 1.2 Keller Wall Boundary Conditions coefficients.

Type of Boundary Condition	$c_1$	$c_2$	$c_3$	$c_4$
Closed Wall	0	0	1	0
Open Jet	0	1	0	0
Perforated Wall	0	1	$B$	0
Ideal Slotted Wall (Integrated Form)	1	0	$K$	0
Ideal Slotted Wall (Differentiated Form)	0	1	$\partial K / \partial x$	$K$
General Form of the Slotted Wall	0	1	$\partial K / \partial x + B$	$K$

In the panel code ANTARES, wall boundary conditions are satisfied at each wall panel centroid. For  $N$  panels describing the wind-tunnel boundary, the strengths of the singularities describing the model can be obtained from a system of  $N$  linear equations. From the singularities strengths, the perturbation velocity can be calculated, which allows obtaining the blockage factor and angle of attack corrections. The principle of superposition is applied by Ulbrich (2000) to calculate the wall-interference corrections in terms of the linear superposition of the perturbation velocity from the use of panel method code ANTARES and the free-air results from the singularity representation of the test article. Figure 1.14 summarizes how the Wall Interference Correction System (WICS) and the panel code ANTARES are applied to calculate wall-interference corrections at NASA Ames 11 ft TWT.

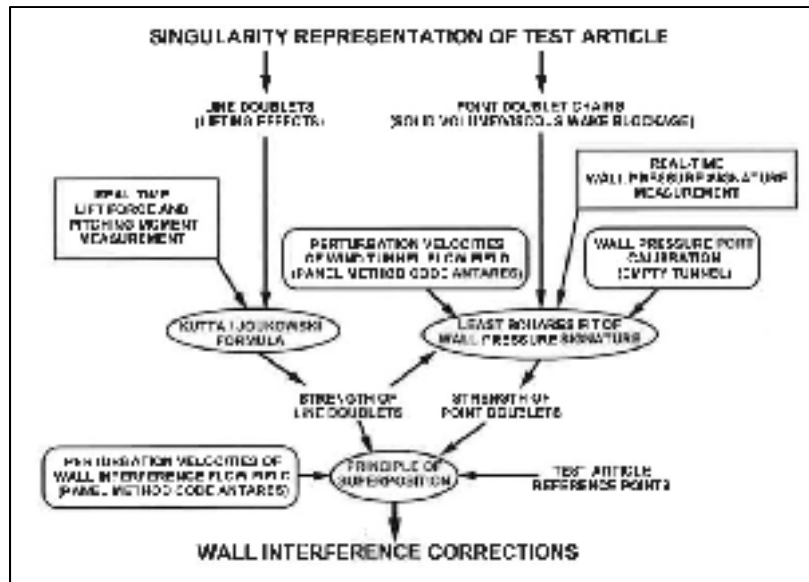


Figure 1.14 Real-time wall interference calculation at NASA Ames 11ft TWT. From: Ulbrich *et al.* (2003).

### C. Two-variable method

The two-variable method was developed by Ashill *et al.* (1982) at the Royal Aircraft Establishment (RAE) in the 1980s and then applied on combat aircraft testing at the RAE 13ft x 9ft wind tunnel at RAE Bedford (Ashill *et al.*, 1988). It was created as a suitable way of calculating wall interference for complex flows such as those observed around V/STOL aircraft or helicopters, where a potential-theory flow representation is not adequate and wall corrections cannot be achieved by any of the previously described techniques. In a classification and review of different wall-interference assessment and correction methods, Ashill (1993) explains how the two-variable method does not need any kind of model representation, but requires the measurement of both the axial and the normal components of the flow velocity on the walls.

The nature of the two-variable method makes it suitable for low-speed wind-tunnel testing with solid walls, where the boundary layer is relatively thin. In solid-wall tests, the normal component of the flow velocity at the walls is defined by the no-flow condition through the

wall, which simplifies the process by directly assuming the normal component of the flow velocity to be zero. However, for ventilated walls, the measurement of normal velocity over the whole measurement boundary is much more complicated; which explains why this method has usually been restricted to solid-wall tests.

In the two-variable method, it is supposed that there is a region  $\Lambda$  (Figure 1.15) in the test section, bounded by the surface  $S_1$  surrounding the model and the surface  $S_2$  around the walls, where the flow satisfies the linearized form of the potential equation as in Eq. (1.8).

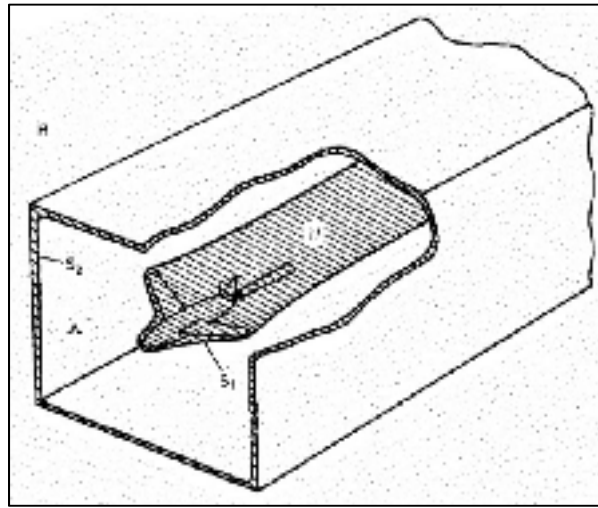


Figure 1.15 Region and bounding surfaces for application of Green's theorem. From: Ashill *et al.* (1982).

By applying the Prandtl-Glauert transformation to account for compressibility effects, the Laplace equation  $\Delta\phi = 0$  is obtained at the region  $\Lambda$ . Then the use of Green's theorem provides a solution of the flow potential  $\phi$  in  $\Lambda$ . Similarly, the free-air component of the potential flow  $\phi_F$  can be obtained if integration is confined to the surface  $S_1$ . The potential

due to the wall interference  $\phi_I$  can be calculated by subtracting these two expressions, as seen in Eq. (1.15), from Ashill (1993).

$$\phi_I = \phi - \phi_F \quad (1.15)$$

In the solid-wall test section of the 13ft x 9ft Low-Speed Wind Tunnel, static pressures are measured at seven streamwise rows at the roof and side walls and at a number of positions, referred to as Row 'A', at the mid-station away from the corner fillets (Figure 1.16). No measurements are taken at the floor where half-models are mounted, which acts as a reflection plate (plane of symmetry). The measured pressure data  $C_P$ , corrected to empty tunnel conditions, can be used to estimate the streamwise velocity  $u$  at the walls by using the linearised version of Bernoulli's equation, where  $U_0$  is the free-stream velocity far upstream.

$$C_P = -2 \frac{u}{U_0} \quad (1.16)$$

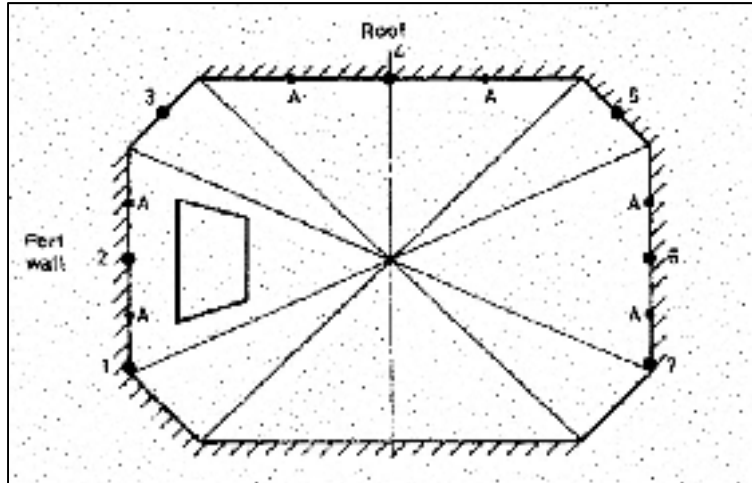


Figure 1.16 Distribution of pressure rows in the RAE 13ft x 9ft Low-Speed Wind Tunnel From: Ashill *et al.* (1988).

### 1.3 The one-variable method at the NRC 5ft TWT

The one-variable method established by Mokry (1985) is the wall-interference calculation methodology currently applied at the NRC 5ft Trisonic Wind Tunnel. It makes use of only

one flow variable, the stream-wise component of the interference velocity  $u_I$  to calculate the wall interference over the model and obtain the necessary wall corrections. By derivation of the potential flow  $\phi$  with respect to the compressibility-scaled axial coordinate, the flow velocity  $u$  can be obtained Eq. (1.17); which can be expressed as the superposition of wall-interference velocity and free-air velocity, Eq. (1.18), from Mokry (2006).

$$u = \frac{\partial \phi}{\partial \xi} = \beta \frac{\partial \phi}{\partial x} \quad (1.17)$$

$$u = u_F + u_I \quad (1.18)$$

The interference velocity satisfies the Laplace equation in the test section as indicated by Mokry (2006), Eq. (1.19).

$$\frac{\partial^2 u_I}{\partial \xi^2} + \frac{\partial^2 u_I}{\partial y^2} + \frac{\partial^2 u_I}{\partial z^2} = 0 \quad (1.19)$$

On the test section boundary, the interference velocity can be obtained from the linear superposition of the flow velocity and its component in free-air. The flow velocity can be obtained from the Mach number and the static pressure measured at the pressure rails located along the wind-tunnel walls, while the free-air velocity can be calculated from a potential theory singularity-model representation.

$$u_I = u - u_F = -\beta \frac{1}{2} C_P - \beta \frac{\partial \phi_F}{\partial x} \quad (1.20)$$

$$C_P = -2 \frac{\partial \phi}{\partial x} \quad (1.21)$$

Together, Eqs. (1.19) and (1.20) defining the interference velocity  $u_I$  in the test section and on the test section boundary, represent an interior Dirichlet problem. A doublet-panel method is the approach taken to solve this Dirichlet problem in half-model tests.

### ***Doublet-panel method***

In the general flow domain, as presented by Mokry *et al.* (1987), the interference velocity  $u_I$  can be represented by the double layer potential equation, Eq. (1.22), where  $f$  is the doublet strength,  $S$  is the test section surface and  $\partial/\partial n$  is the outward derivate.

$$u_I(\vec{r}_0) = \iint_S f(\vec{r}) \frac{\partial}{\partial n} \left( \frac{1}{4\pi|\vec{r}_0 - \vec{r}|} \right) \partial S \quad (1.22)$$

The position vectors  $\vec{r}_0 = (\xi_0, y, z)$  and  $\vec{r} = (\xi, y, z)$  point to a fixed observation point and a point running over the surface  $S$ , respectively. The acknowledged test section boundary is formed by the ceiling, floor, side-wall (south-wall, not attached to the model), upstream and downstream faces, and their reflection-plane images (Figure 1.17). The reflection-plate is not part of the surface  $S$ .

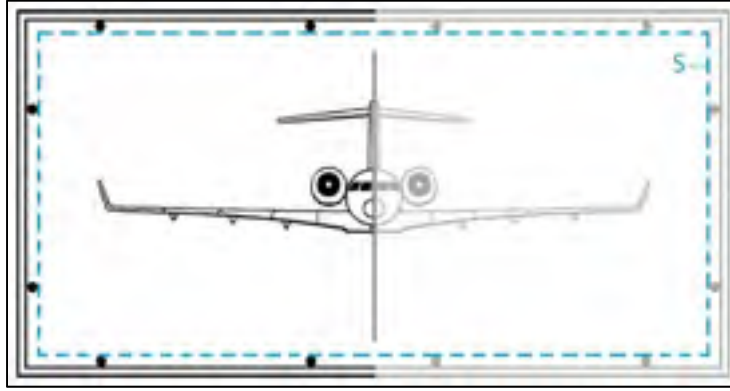


Figure 1.17 NRC 5ft TWT test section and mirror image respect to reflection plane.

As the observation point  $\vec{r}_0$  approaches a smooth surface point  $\vec{r}_k$ , the interference velocity  $u_I$  can be represented by the Fredholm integral equation of the second kind for the doublet strength, Eq. (1.23).

$$u_I(\vec{r}_k) = -\frac{1}{2}f(\vec{r}_k) + \iint_S f(\vec{r}) \frac{\partial}{\partial n} \left( \frac{1}{4\pi|\vec{r}_k - \vec{r}|} \right) \partial S \quad (1.23)$$

In order to solve this integral equation, a panel-method is applied by dividing the test section surface, upstream and downstream faces into  $N/2=215$  rectangular panels, as seen in Figure 1.18, each of them with a surface denoted by  $S_j$  ( $j = 1, \dots, N$ ) and a doublet strength  $f(\vec{r}) = f_j$  with  $\vec{r} \in S_j$ .

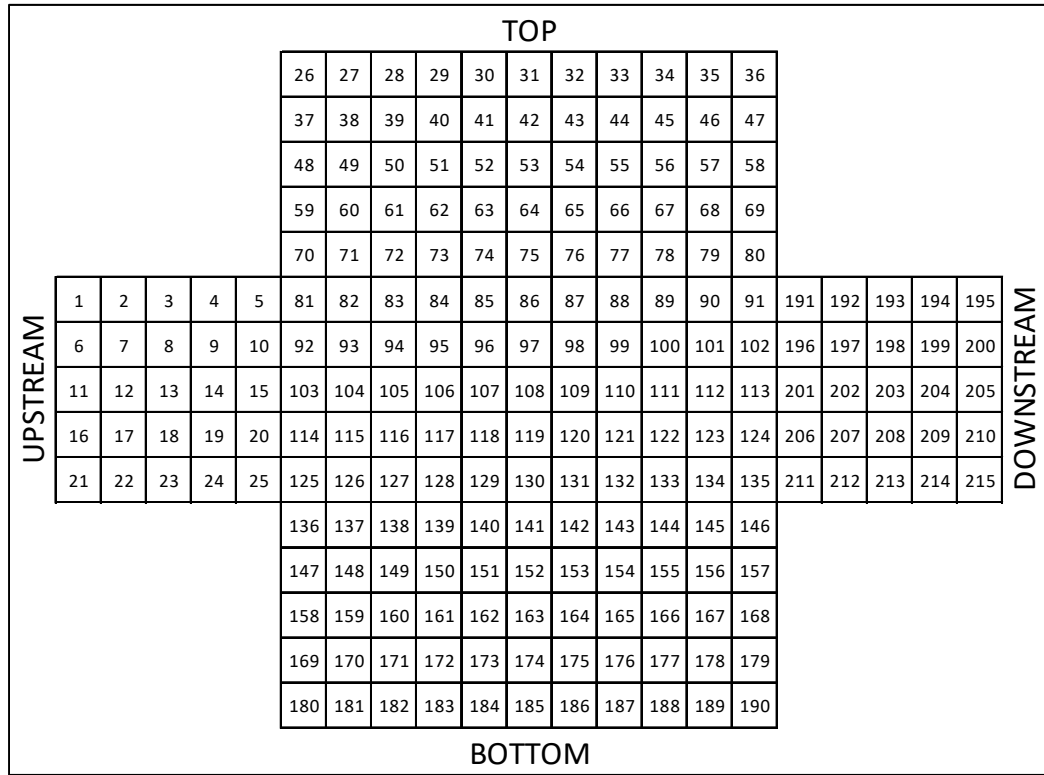


Figure 1.18 Panel distribution on boundary test surface.

Selecting  $\vec{r}_k$  to be the panel centroids and naming  $u_l(\vec{r}_k) = u_k$ , the result is the following system of linear algebraic equations.

$$\sum_{j=1}^N A_{kj} f_j = u_k, \quad k = 1, \dots, N \quad (1.24)$$

$$A_{kj} = \begin{cases} -\frac{1}{2}, & \text{if } j = k \\ \iint_S \frac{\partial}{\partial n} \left( \frac{1}{4\pi|\vec{r}_k - \vec{r}|} \right) dS, & \text{if } j \neq k \end{cases} \quad (1.25)$$

Because of symmetry, the system of equations can be reduced back to  $N/2=215$ .

The interference velocity  $u_I$  is first calculated at the pressure taps locations on the pressure rails and interpolated to the  $n_x$  X-coordinates of the panel centroids (Figure 1.19a). Then, for each of the sections in which the boundary surface is divided along the X-axis, the stream-wise  $u_I$  curves are smoothed and expanded to the panel centroids in the Y and Z directions by interpolation/extrapolation (Figure 1.19b and Figure 1.19c).



Figure 1.19 Interference velocity interpolation sequence.

Once the doublet strengths  $f_j$  are defined, the interference velocity  $u_I$  can be calculated at any point  $\vec{r}_0$  inside the test section using the discrete form of the double layer potential, Eq. (1.26).

$$u_I(\vec{r}_0) = \sum_{j=1}^N f_j \iint_{S_j} \frac{\partial}{\partial n} \left( \frac{-1}{4\pi|\vec{r}_0 - \vec{r}|} \right) \partial S \quad (1.26)$$



### *Wall corrections applied*

Once the stream-wise component of the interference velocity  $u_I$  is determined (and its transverse components,  $v_I$  and  $w_I$ , which can be calculated by integrating the irrotational-flow conditions), Mokry (2006) details how to calculate the necessary wall corrections. Zero side-wash interference  $v_I$  is assumed based on symmetry and zero-yaw. First, the Mach number correction  $\Delta M$  can be obtained as a function of the blockage factor  $\epsilon$ , as seen on Eqs. (1.27) and (1.28).

$$\epsilon = \frac{\Delta U}{U} = \frac{\partial \phi_I}{\partial x} = \frac{1}{\beta} \cdot \frac{\partial \phi_I}{\partial \xi} = \frac{1}{\beta} \cdot u_I(\xi, y, z) \quad (1.27)$$

$$\Delta M = \left[ \left( 1 + \frac{\kappa - 1}{2} M^2 \right) \epsilon \right] M \quad (1.28)$$

The angle of attack correction  $\Delta \alpha$ , Eq. (1.29), is calculated as a function of the vertical component of the interference velocity  $w_I$  and the free-air velocity  $\partial \phi_F / \partial z$ , obtained from a potential theory representation of the model. The coordinates  $x_{ups}$  and  $z_{bot}$  define the test section boundary.

$$\Delta \alpha = w_I \left( \frac{x_{ups}}{\beta}, -z_{bot} \right) - w_I(0, -z_{bot}) - \frac{\partial \phi_F}{\partial z}(x_{ups}, 0) \quad (1.29)$$

The stream-wise component of the interference velocity  $u_I$  and the half-model geometry can additionally provide a buoyancy drag correction  $\Delta C_D$ , Eq. (1.30).

$$\Delta C_D = \frac{1}{S_R} \int_{x_t}^{x_n} 2u_I F'(x) dx \quad (1.30)$$

Where  $S_R$  is the half-model reference area (planform) and  $F(x)$  is the axial distribution of the half fuselage cross-sectional area.

## 1.4 Problem statement

As previously discussed, several factors such as flow velocity, model size and location within a specific test section determine the relevance of wall interference in wind-tunnel testing. This research project studies the flow around the semispan model of a commercial aircraft in a wind tunnel with a square solid-wall test section at low-speed subsonic flow reaching high angles of attack. For these conditions, it is known that the presence of the wind-tunnel walls has a significant influence over test results.

At the NRC 5ft Trisonic Wind Tunnel, the one-variable method quantifies and corrects wall interference by employing basic model geometry parameters, balance loads and pressure data experimentally measured at the tunnel. Toledano *et al.* (2015) investigates the strengths and weaknesses of the one-variable method based on existing experimental data from a typically sized half-model tested at the TWT. The data considered was that from a 2012 Bombardier test performed on a semispan model of their Global 6000 aircraft at low subsonic speeds reaching stall. Test data were acquired using both a modified version of the TWT test section operating as a solid-wall boundary, as well as its usual 1.5% open perforated boundary, under the test conditions presented in Table 1.3. This allowed correcting the data using standard textbook techniques such as those from Rae and Pope (1984) as well as with the one-variable method currently applied in the NRC 5ft TWT. Different initial conclusions were drawn from the analysis of the available data, revealing concerns in the corrections provided by the system.

Table 1.3 Semispan Global 6000 test campaign matrix.

Model configuration	Test section boundary	Mach	Reynolds	Run number
Global 6000	Solid wall	0.2	$7.84 \times 10^6$	1271
Global 6000	Ventilated wall	0.2	$7.84 \times 10^6$	1269

Although the  $\Delta\alpha$  wall corrections calculated using the one-variable method in Figure 1.20 show a very good agreement of the  $\Delta\alpha/C_L$  slope with acceptable noise compared to theoretical corrections predicted by standard numerical methods like those defined by ESDU (1995) or AGARDograph 109 (1966), they present a significant constant offset. Particularly, all theories, regardless of the specifics of the wing, etc.; will predict zero angle of attack correction at zero lift when the wing and body are centrally located in the test section as this model was. A parametric study to investigate the possible reasons explaining the angle of attack correction offset was carried out. Its results will be presented in the results chapter.

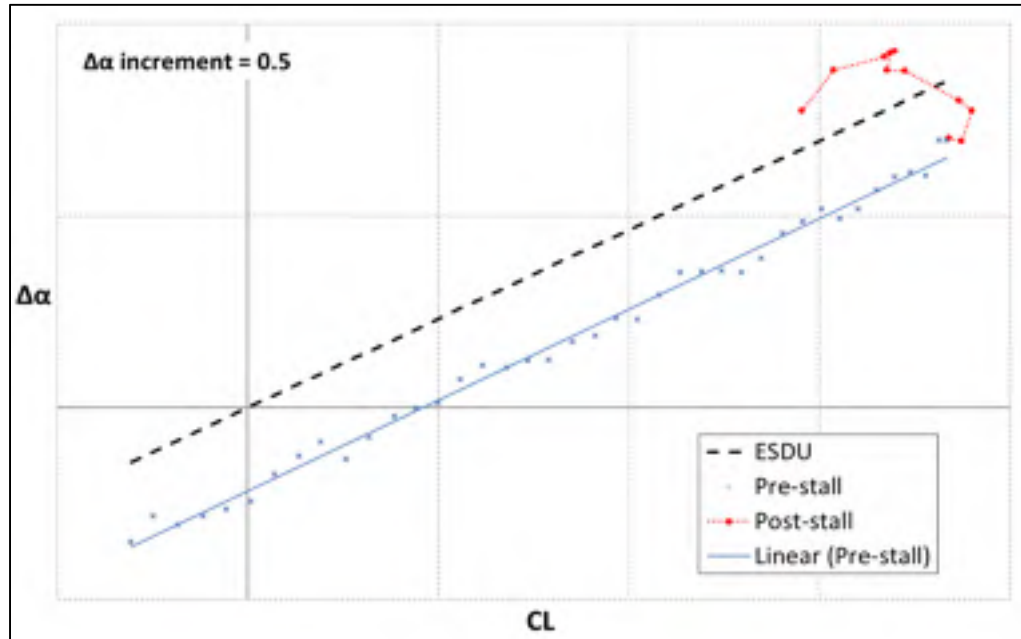


Figure 1.20 Angle-of-attack correction for the Global 6000 solid-wall data set.

Aside from the  $\Delta\alpha$  offset issue, the one-variable method performs adequately in the linear pre-stall region. However, the wall corrections calculated by this method lose credibility for high angles of attack, as can be appreciated in the post-stall curve in Figure 1.20, where flow separation is significant. At high angles of attack, the semispan tunnel model starts

experiencing stall, which dramatically changes the flow behavior around the model. The fact that the potential-theory singularity representation currently used by the one-variable method does not take separated flow regions into account, as it will be further argued in the results chapter, justifies the unreliability of the corrections in stall.

As the introduction chapter explained, the development of CFD has overshadowed wind-tunnel testing in the last few decades. However, in flow conditions with significant flow separation, neither wind-tunnel results corrected using the current one-variable method nor CFD are able to provide accurate enough solutions by themselves. One of the main sources of originality for this project will be to investigate how CFD can be used as a tool to validate and improve the wall corrections provided by the one-variable method. The methodology section will define the limits of accuracy considered for high incidence applications.

## CHAPTER 2

### OBJECTIVES

The studies performed over the course of this research project serve the main goal of gaining an overall improvement to the one-variable method, the wall-correction methodology applied at the NRC 5ft Trisonic Wind Tunnel. Several secondary objectives will also be sought throughout this investigation.

#### **2.1 Main goal - Improve wall corrections in stall conditions**

The main objective of the work described in this dissertation is to update the wall-correction methodology employed at the NRC 5ft TWT to correct its deficiencies, presented at the end of the previous chapter (§ 1.4). Experimental and numerical data are employed to investigate how the various stages of the wall-interference calculation method can be improved. The main challenge to overcome is calculating accurate and reliable wall corrections in real-time subsonic tests at angles of attack reaching stall, namely due to the significant flow separation that develops over the wind-tunnel model in these conditions.

The secondary objectives described below are intended to contribute to the project's main goal.

#### **2.2 Secondary objectives**

##### *Validation of the one-variable method in pre-stall conditions*

Before updating the wall-correction methodology, the range of validity of its current version needs to be clearly understood. The one-variable method can be validated based on standard corrections like those obtained using ESDU (1995) or Rae and Pope (1984), provided solid-wall experimental data are available. Investigating alternative methods to validate the

one-variable method is one of the secondary objectives of this research project. Employing CFD to obtain numerical results will enable exploration of this matter.

*Update the singularity representation of the wind-tunnel model*

As previously introduced, based on potential theory, the one-variable method represents the wind-tunnel model or test article by means of a combination of singularities or fundamental solutions of the Laplace equation. Increasing the accuracy of the model representation over the entire wind-tunnel testing envelope translates into increasing the quality of wall corrections. Investigating different ways to update the potential theory representation of the model of a typical aircraft tested at the NRC 5ft TWT is one of the secondary objectives sought in this project, which is expected to contribute to the main objective of improving the wall-correction methodology.

*Obtain wall corrections in stall*

A theoretical study will be launched to explore the use of computational results in free-air as an alternative to the potential theory representation of the model. Although it would be impossible to implement the use of CFD to represent the flow behavior around the model in free-air when correcting wind-tunnel data in production tests, it can be applied for any particular case study to investigate how wall corrections should behave when testing a typical transport aircraft at subsonic flow conditions reaching stall.

*Explore additional applications of the wall-correction methodology to common operations at the NRC 5ft TWT*

The techniques employed during the case studies included in this dissertation, such as the application of CFD in combination with the existing wall-correction methodology, have been generally applied to subsonic flow wind-tunnel testing. The implementation of these techniques to transonic-flow applications will be another secondary objective of this research project.

## **CHAPTER 3**

### **METHODOLOGY**

This section presents the specific methodology followed to achieve the goals presented in the previous chapter. Three particular test article geometries are considered throughout this research project, all of which are semispan wind-tunnel models. Those geometries correspond to the Bombardier Global 6000, a NACA0012 calibration wing and the NASA Common Research Model in its wing/body configuration. The experimental data from those geometries are analyzed and applied to calculate wall corrections using an offline test bench developed as part of this research project, which effectively reprocesses existing experimental data sets while testing any modifications to the wall-correction method. Experimental data for those geometries are available both in solid-wall and ventilated-wall boundary conditions for tests at the NRC TWT in low-speed subsonic flows reaching stall. In addition, CFD results are used to assess the accuracy of the potential theory model representation, paramount to the calculation of wall corrections, both in the attached and separated flow regions. These results are generated using commercial mesh generators and solvers, as it will be described later in this chapter. The use of CFD has a very important role, not only as a tool to optimize potential flow models, but also to function as a benchmark to validate whether the accuracy of the results is acceptable for the considered high incidence applications.

#### **3.1 Development of an offline test bench for the one-variable method**

The first step before introducing and testing modifications to the wall-correction methodology applied at the NRC 5ft Trisonic Wind Tunnel was to develop a tool that would allow computing wall corrections using the one-variable method without the need to access and re-process wind-tunnel raw data. The two main achievements of this offline test bench were a) allowing the possibility to work with pre-processed data to avoid the need for

running the data reduction code every time a data set was examined and b) optimizing the wall-correction code to increase its efficiency, cutting computational times about 35%.

An additional capability was added to allow plotting contour maps with the Mach number and the angle of attack corrections at the XY and YZ planes defined by a given location in the tunnel, requested as input by the code, as can be seen in Figure 3.1. A detailed description of this tool can be found in Toledano *et al.* (2015).

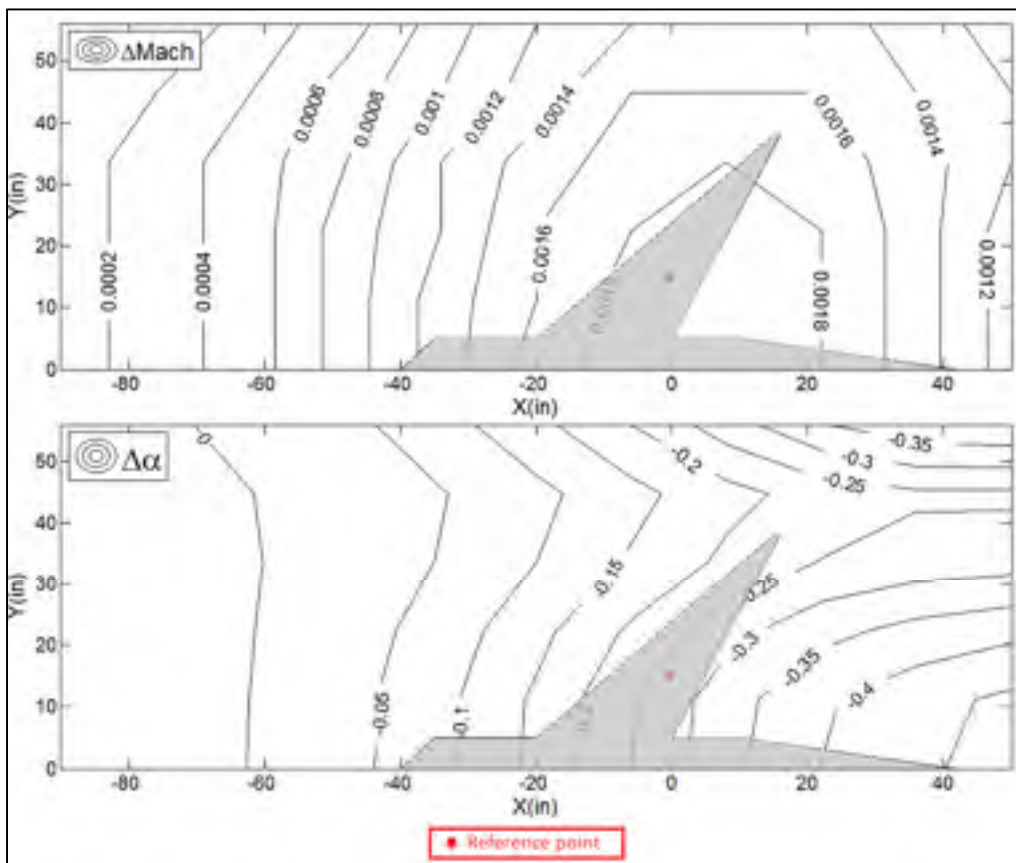


Figure 3.1 Contour maps including Mach number and angle of attack corrections. The red dot indicates the location of the model's reference point in the wind tunnel.



### 3.2 Geometries considered for the investigations at the NRC 5ft TWT

Any updates to the wall-correction methodology need to be tested for a specific data set on a given model geometry. Over the course of this research project, data from different semispan models have been available for the investigations carried out.

#### 3.2.1 Bombardier Global 6000

This semispan wind-tunnel model is a scaled representation of the starboard side of the Bombardier Global 6000 business jet with a clean-wing, tail-off configuration, as Figure 3.2 illustrates. Detailed geometry specifications for this model are confidential and will not be included in this dissertation.

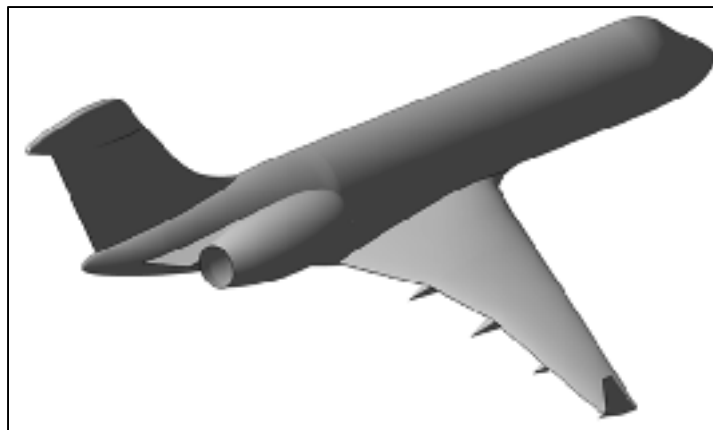


Figure 3.2 Semispan Bombardier Global 6000 model.

The considered data sets from wind-tunnel tests on this model at the NRC TWT are those summarized in Table 1.3, both with a solid-wall and ventilated-wall boundary at low-speed subsonic flow. These sets were employed during the development of the offline test bench presented in the previous section. Once in service, those sets were reprocessed in the test

bench and analyzed to complete the initial assessment of the strengths and weaknesses of the one-variable method presented as part of the problem statement in the first chapter (described in § 1.4).

Additionally, the Global 6000 data were used to perform a study to determine the influence of several test parameters over the  $\Delta\alpha$  offset issue observed in Figure 1.20. The results of this parametric study will be presented in the next chapter.

### 3.2.2 NRC Symmetrical Calibration Wing

This model was built by the NRC Design and Fabrication Services (DFS) to become part of their wind-tunnel calibration inventory. The model is a straight wing made of 17-4 PH steel with zero taper or twist, as can be seen in Figure 3.3. The airfoil is a NACA 0012 profile. The chord of the model is 10 inches and the span measured from the reflection plane to the tip is 30 inches. This gives an aspect ratio of 6 for the equivalent full span wing. Model geometry specifications can be found in Table 3.1.

Table 3.1 NRC calibration wing (Calwing)  
geometry specifications.

Aspect Ratio	6
Model Span (b)	30 inches
Reference Area (S)	300 square inches
Mean Aerodynamic Chord (c)	10 inches

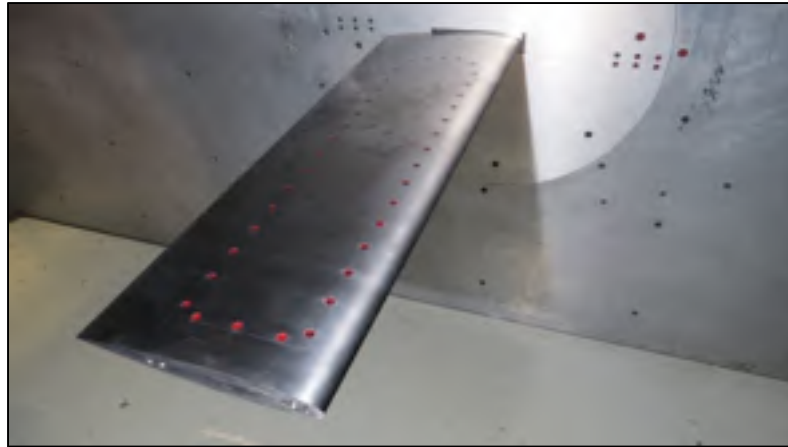


Figure 3.3 Semispan NRC calibration wing (Calwing) model.

The NACA 0012 airfoil is a commonly used profile for applications such as experimental wind-tunnel calibration or numerical code verification. An example of the latter can be observed in the work presented by Roy and Tinoco (2017) in the Sixth AIAA CFD Drag Prediction Workshop, including simulation results on a 2D NACA 0012 airfoil performed as CFD code verification preceding a series of test studies for the NASA Common Research Model.

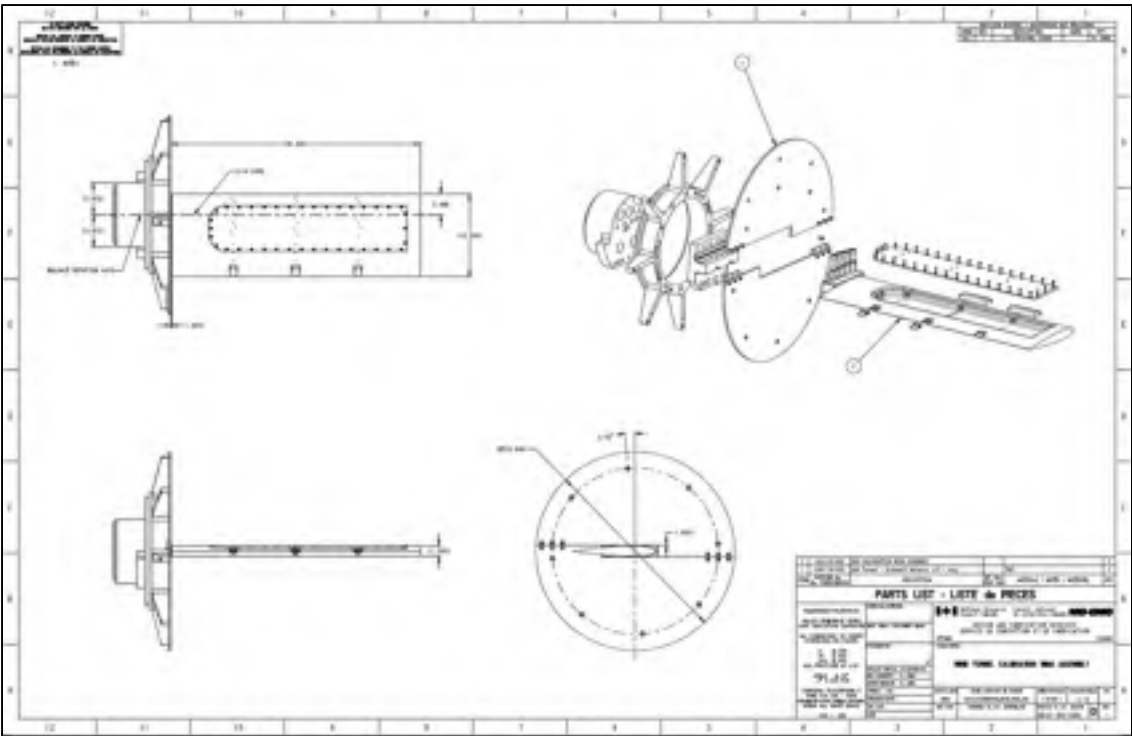


Figure 3.4 Assembly of semispan calibration wing (Calwing) at NRC TWT.

At the NRC TWT, the symmetrical NACA 0012 “calwing” (Figure 3.4) was used to collect balance data in subsonic and transonic conditions. These data were employed to assess some important calibration parameters like the absolute test section flow angularity. Figure 3.5 shows aerodynamic coefficients that were obtained from the balance forces and moments collected during a “sweep” run performed at subsonic flow in the TWT with a solid-wall test boundary configuration. This dataset test configuration is presented in Table 3.2.

Table 3.2 Test configuration during NRC TWT run 56303 for the NACA 0012 “calwing”.

Model configuration	Test section boundary	Mach	Reynolds	Run number
NACA 0012 “calwing”	Solid wall	0.25	$3.97 \times 10^6$	56303

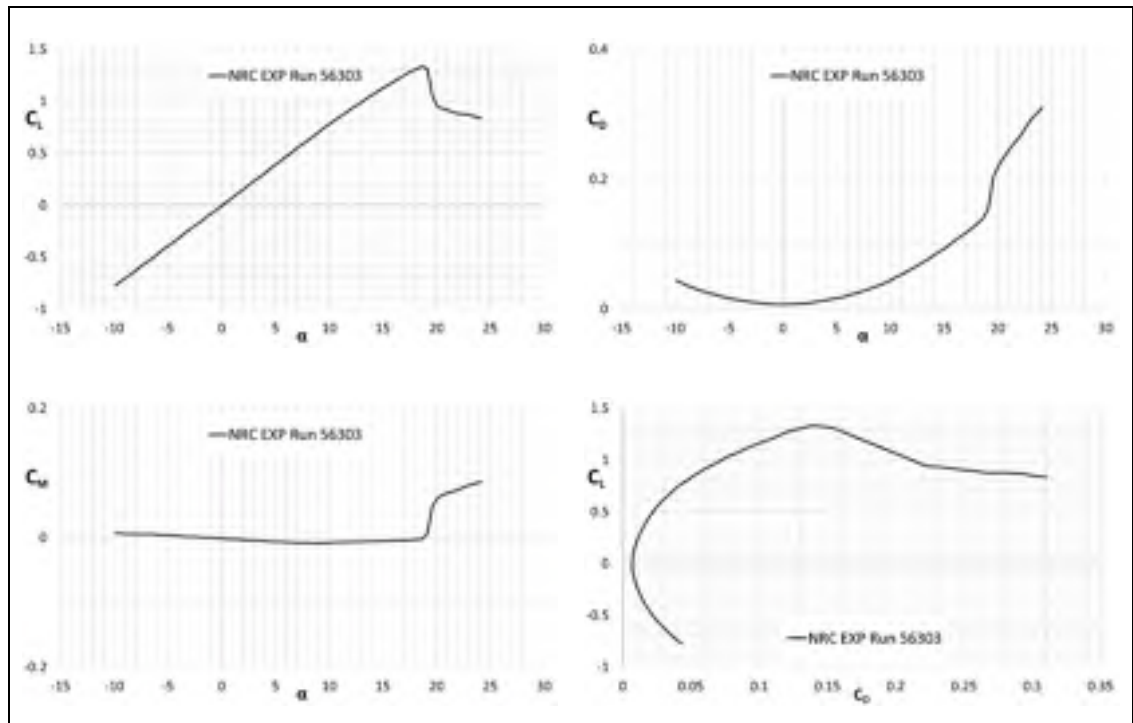


Figure 3.5 Experimentally measured aerodynamic coefficients for the symmetrical calibration wing tested at the NRC TWT with a solid-wall test boundary at  $M=0.25$  and  $Re=3.97 \times 10^6$

Additionally, model surface pressures were collected at three chordwise rows of pressure taps on the wing at the following span stations  $\eta = 0.25, 0.5, 0.75$ . Figure 3.6 and Figure 3.7 present some of those wing pressure readings at  $\alpha=15^\circ$  and  $\alpha=20^\circ$ , respectively. The model required two 50 psid and two 15 psid ESP modules. Due to the absence of a fuselage in this model, the ESP ZOC 22 pressure modules needed to be located within a cavity in the wing accessed by a removable cover. No boundary layer trips were used with this model.

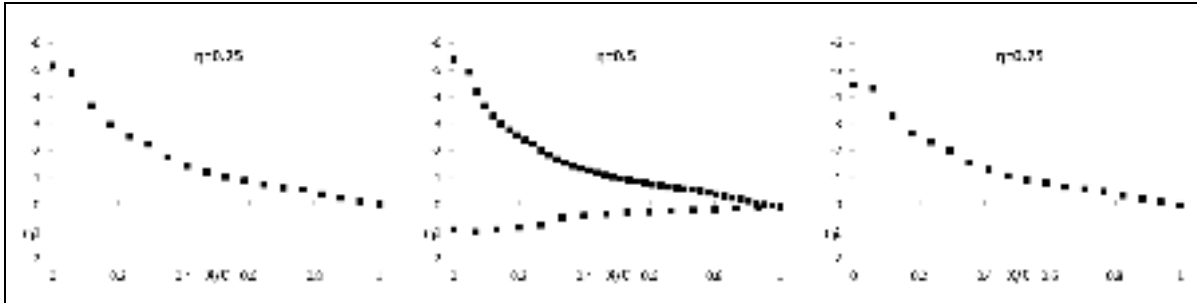


Figure 3.6 NRC experimental wing pressure distributions at  $\alpha=15^\circ$  measured on the symmetrical calibration wing tested at the NRC TWT (run 56303).

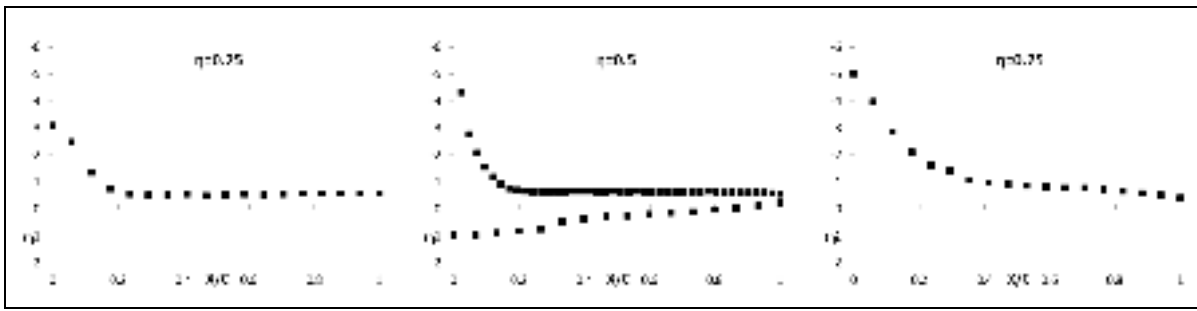


Figure 3.7 NRC experimental wing pressure distributions at  $\alpha=20^\circ$  measured on the symmetrical calibration wing tested at the NRC TWT (run 56303).

The validity of these data could be further checked against results available in the literature referring to this airfoil, like those presented by Abbott *et al.* (1959) or Goett *et al.* (1939) for a NACA 0012 wing of aspect ratio 6.

### 3.2.3 NASA Common Research Model

The NASA Common Research Model at 2.7% scale (Rivers *et al.*, 2011) in its standard cruise clean wing configuration was the semispan model geometry considered to investigate different possible ways to update the singularity representation of the test article required by the one-variable method. This geometry is representative of a typical transport aircraft model tested at the NRC 5ft TWT. To achieve the desired semispan model configuration, the CRM left (or port) wing, horizontal tail and nacelle/pylon were loaned from NASA Langley Research Center (LaRC). All the parts supplied by NASA are of VASCO Max C-250 steel

specifically selected for cryogenic operation. The model half fuselage, backing plate and boundary layer filler plate were designed and fabricated by NRC-DFS using materials suited to the NRC TWT. The fuselage, backing plate, and boundary layer filler plate are machined from aluminum, while the wing to balance mounting block and the dummy right hand wing stub are machined from PH 17-4.

A summary of the semispan CRM geometry specifications can be found in Table 3.3 and an overview of its assembly in the NRC TWT is presented in Figure 3.9.

Table 3.3 Semispan CRM geometry specifications.

Aspect Ratio	9.0
Model Span (b)	31.23 inches
Reference Area (S)	216.79 square inches
Mean Aerodynamic Chord (c)	7.45 inches
Fuselage Length (L)	66.73 inches
Fuselage Maximum Radius (r)	3.29 inches
Wing Taper Ratio	0.275
Sweep Angle	35°

Figure 3.8 indicates the location of nine chordwise rows of pressure taps on the model wing distributed spanwise at the stations specified in Table 3.4. These wing pressure measurements are relevant for the work included in this research project since they were used to understand the development of flow separation on the suction side of a lifting wing as the incidence nears stall conditions.

Table 3.4 Normalized spanwise section location  $\eta$  of the pressure port rows on the semispan CRM wing.

Row	A	B	C	D	E	F	G	H	I
$\eta(\%)$	13.1	20.1	28.3	39.7	50.2	60.3	72.8	84.6	95.0

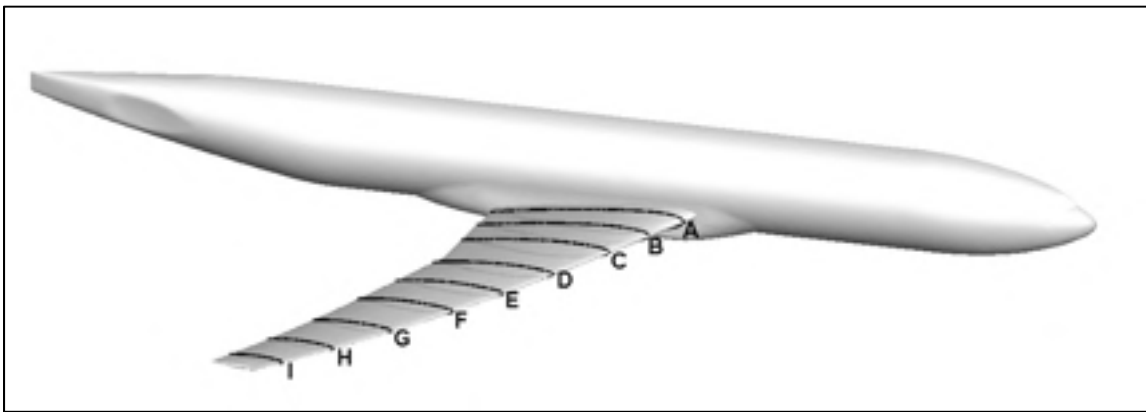


Figure 3.8 Location of the nine rows of wing pressure taps at the 2.7% scale semispan NASA CRM.

Boundary layer trips were also used both in the model's fuselage nose and wing 10% chord line to ensure turbulent boundary layer flow past them.



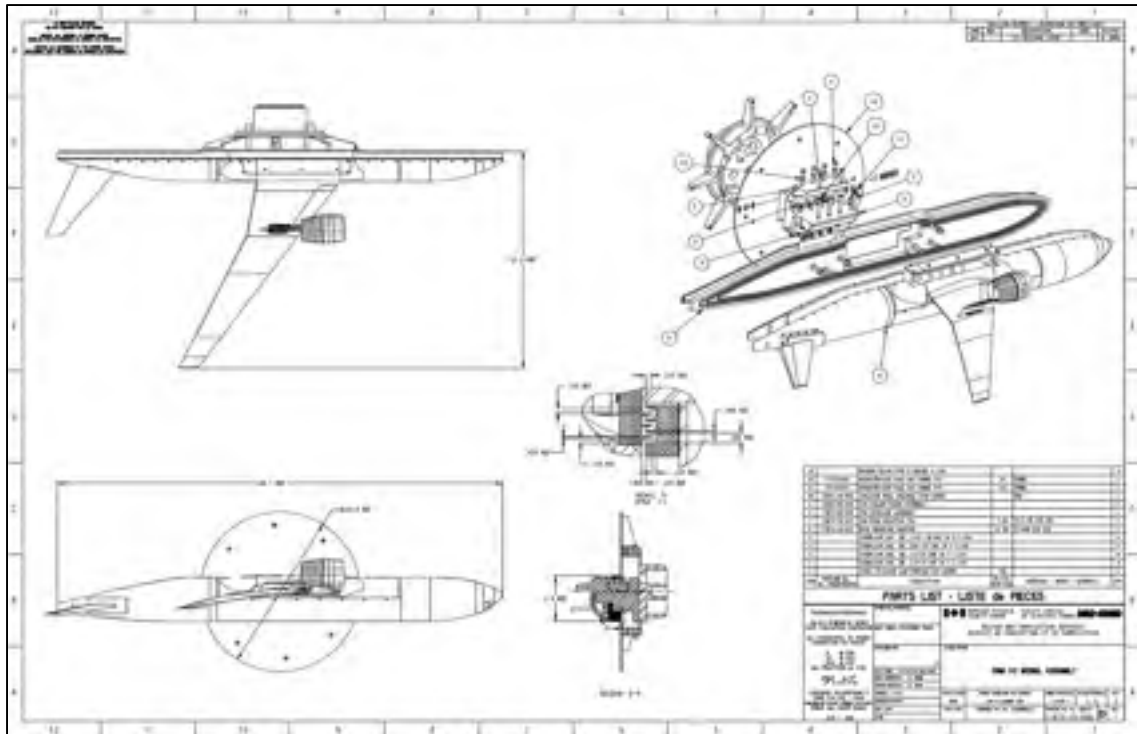


Figure 3.9 Assembly of semispan NASA CRM at NRC TWT.

The next section will describe the array of experimental tests and numerical simulations performed on the NASA CRM semispan model as part of this research project.

### 3.3 Study of the NASA Common Research Model (CRM) at the NRC 5ft TWT

An interest in developing experimental databases to validate specific CFD applications was the original motivation for the development of the NASA Common Research Model (Vassberg *et al.*, 2008). The first experimental investigations carried out using this model were performed in the NASA Ames 11ft Transonic Wind Tunnel and NASA's National Transonic Facility (Rivers *et al.*, 2014). These facilities use the Transonic Wall Interference Correction System (TWICS) for the assessment of wall interference (see Iyer *et al.*, 2000). Since then, this model has served as a case study in numerous projects. Some of the research

employing the CRM focused on the use of CFD to study phenomena like the influence of support systems in wind-tunnel testing, like the work presented by Rivers *et al.* (2012) and Waldmann *et al.* (2016). Other studies used the CRM as a benchmark to compare results at wind-tunnel facilities, like Rivers, Quest and Rudnik (2015) do when comparing test data from NTF to that obtained at the European Transonic Facility (ETW).

The NASA Common Research Model (CRM) was an ideal model to be employed in experimental and numerical experiments performed as part of this research project with the main goal of improving the wall-correction methodology at the NRC transonic wind tunnel. The CRM has already been used to investigate wall-interference effects in facilities like ETW (Gorbushin *et al.*, 2015) and JAXA (Kohzai *et al.*, 2013).

### 3.3.1 NASA CRM experimental test campaign

A wind-tunnel test campaign on the NASA CRM was completed in September 2016 (Toledano *et al.*, 2017) at the NRC 5ft TWT. Several CRM configurations were tested at subsonic and transonic flow conditions at  $Re_c = 2.93 \times 10^6$  and  $Re_c = 5 \times 10^6$ . However, only the results obtained at  $M = 0.25$ ,  $Re_c = 2.93 \times 10^6$  for the CRM wing/body (WB) configuration are relevant to the work included in this dissertation (Table 3.5). Working with the CRM WB configuration (no tail) allows accurately assigning the experimentally measured lift and drag forces to the different singularities representing the model's wing and fuselage. For this configuration, experimental data were obtained for two tunnel boundary conditions, the TWT conventional ventilated wall at 1.5% porosity and a solid-wall test section, which was achieved by covering the boundary perforations.

Table 3.5 Semispan CRM test campaign matrix.

Model configuration	Test section boundary	Mach	Reynolds	Run number
WB (wing/body)	Solid wall	0.25	$2.93 \times 10^6$	56306
WB (wing/body)	Ventilated wall	0.25	$2.93 \times 10^6$	56307

### 3.3.2 NASA CRM numerical simulations

To study the flow behavior around the model in free-air, a series of CFD simulations was performed on the CRM WB configuration at subsonic flow conditions reaching high angles of attack (Toledano *et al.*, 2017).

First, to assess the limitations of the potential flow representation of the model's fuselage, Euler CFD simulations are computed on the CRM fuselage geometry at  $M=0.2$ . These simulations assume the flow to be inviscid and obtain predictions performed on unstructured grids. The mesh size used for this study was about 500,000 cells (tetras), employing approximately 27,000 cells (triangles) to represent the fuselage surface.

The study of the potential flow representation of the wing included a series of RANS computations using the Spalart-Allmaras turbulence model (Spalart *et al.*, 1992; Allmaras *et al.*, 2012) performed on the CRM WB configuration at flow conditions matching the available experimental test results. A hybrid prismatic-tetrahedral unstructured grid was employed for this study. For both the CRM fuselage and CRM WB case studies, the grid generation was carried out using ICEM-CFD (version 15.0) and the CFD flow fields were obtained using the unstructured flow solver COBALT, from Cobalt Solutions LLC.

RANS simulations on the CRM WB were computed on three meshes. A detailed view of the surface mesh on the CRM wing is depicted in Figure 3.10, while Table 3.6 lists the main parameters for the volume meshes employed.

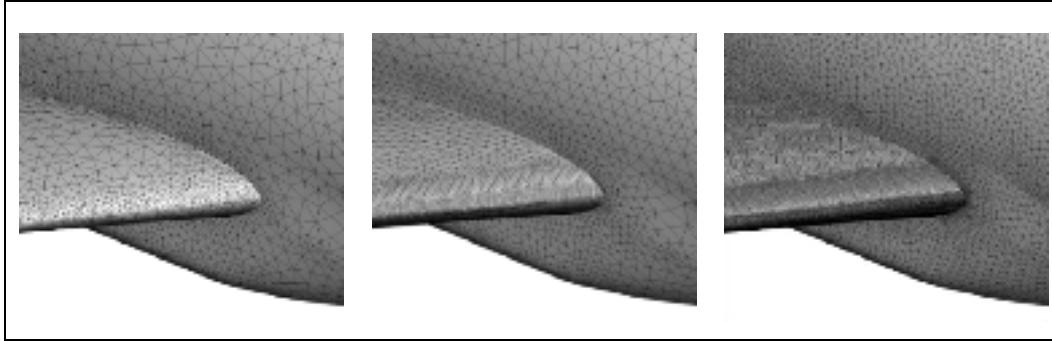


Figure 3.10 Coarse (left), medium (middle) and fine (right) CRM surface meshes.

Table 3.6 Computational grid parameters for the CRM WB meshes.

Grid	Size (elements)	No. grid points	Tetrahedra	Prisms	First cell height	Growth ratio
Coarse	$6 \times 10^6$	2,021,895	2,968,181	2,970,493	$2.75 \times 10^{-4}$	1.300
Medium	$12 \times 10^6$	4,259,710	5,299,326	6,611,975	$2.5 \times 10^{-4}$	1.220
Fine	$36 \times 10^6$	12,911,696	14,933,036	20,570,585	$1.0 \times 10^{-4}$	1.150

Grid convergence results were obtained to provide additional confidence in the reliability of the CFD results for the wing study based on a common approach followed at Drag Prediction Workshop (Mavripilis, 2005; Lee-Rausch *et al.*, 2003). This technique consists of plotting the computed model loads versus the number of grid points to the power of  $-2/3$  ( $N^{-2/3}$ ) for each of the considered meshes. These results are compared to experimental ventilated-wall data (run 56307) to determine if the solutions converge. Figure 3.11 shows a comparison of the aerodynamic coefficients obtained on the three grids in the attached flow region at  $\alpha=5^\circ$  proving that, at these conditions, results converge to the same solution regardless of the mesh size. In Figure 3.12, this comparison is shown for the results obtained at  $\alpha=12.5^\circ$ , close to the experimentally measured maximum lift coefficient where flow separation is significant. Publications like Lutz *et al.* (2015) describe the difficulties of numerically predicting these

challenging flow conditions. However, even in these circumstances, the computed results converge as the mesh is refined.

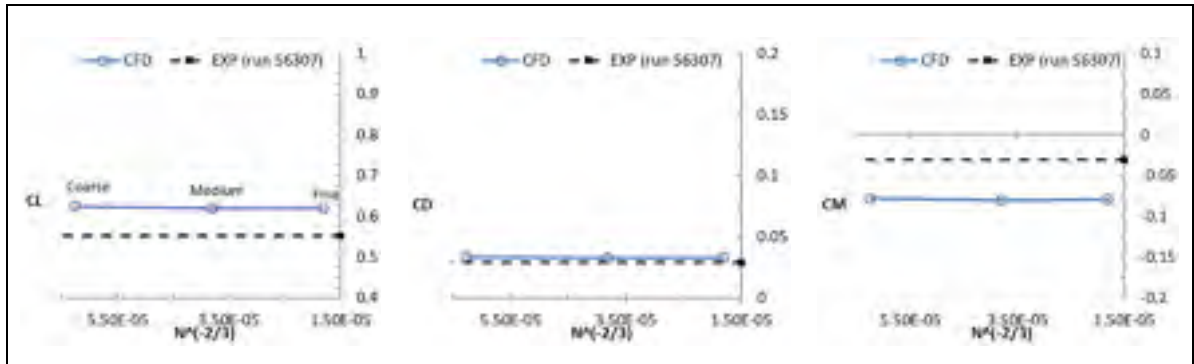


Figure 3.11 Measured model loads at  $\alpha=5.02^\circ$  compared to those predicted by CFD at  $\alpha=5^\circ$  using the three meshes considered versus the number of grid points  $N$  to the power of  $-2/3$ .

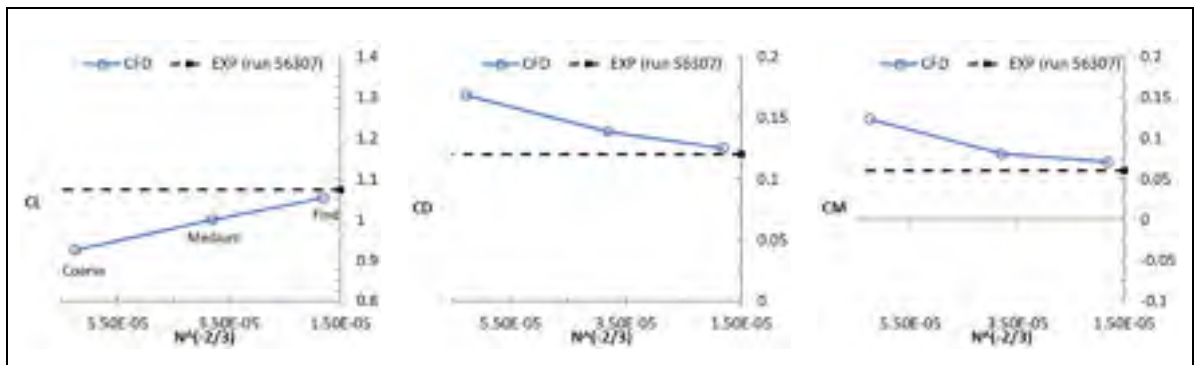


Figure 3.12 Measured model loads at  $\alpha=12.32^\circ$  compared to those predicted by CFD at  $\alpha=12.5^\circ$  using the three meshes considered versus the number of grid points  $N$  to the power of  $-2/3$ .

The reliability of the computational results regarding the CRM WB configuration was successfully proven using experimental measurements of the model forces and moments as well as wing pressure distributions registered during a low-speed ( $M=0.25$ ) test with a ventilated-wall test section boundary (run 56307). The CFD free-air computational results are

compared to those from run 56307 since the uncorrected experimental results measured at the TWT before stall may be considered to be passively corrected with the 1.5% wall-porosity set-up; i.e., they are close to free-air results. For these conditions, Figure 3.13 includes a comparison of the aerodynamic coefficients measured experimentally during the CRM test campaign at the TWT and those predicted by free-air CFD. In an effort to optimize the computational resources available, the data points in the attached flow region were calculated using the coarse grid, whereas the points where flow separation was significant were computed using the fine grid.

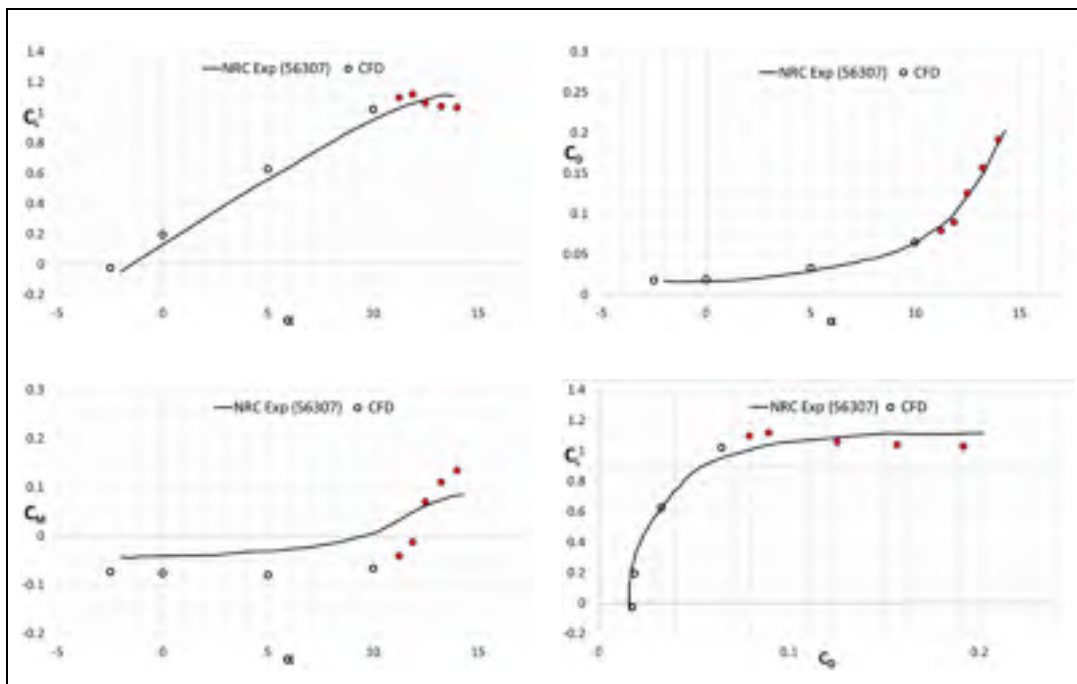


Figure 3.13 CFD predicted aerodynamic coefficients for the CRM WB half-model (red-filled CFD data points indicate flow separation is significant) compared to ventilated-wall NRC experimental results (run 56307).

In pre-stall conditions, Figure 3.13 shows that the CFD predicted aerodynamic coefficients on the semispan CRM WB match satisfactorily the experimental results obtained at NRC using a ventilated-wall test section boundary. Discrepancies in terms of lift coefficient (constant offset of  $C_L \approx 0.07$ ) and pitching moment coefficient in the attached flow region are within acceptable limits according to Rivers *et al.* (2012) or Ueno *et al.* (2013) and have been

observed in the work of Bouriga *et al.* (2015), who studied wall mounting effects on the CRM at subsonic flow using numerical solutions using the SU<sup>2</sup> solver (Palacios *et al.*, 2013 and 2014). A similar behavior is observed by authors studying the CRM model deformation effects (Yasue *et al.*, 2015) and in the results presented at the 2016 Drag Prediction Workshop at transonic flow, as described by Tinoco *et al.* (2017) and Keye *et al.* (2017).

To further verify the reliability of the computational results in pre-stall conditions, the CFD predicted pressure distributions on the wing in free-air were checked against those measured during the ventilated-wall experimental tests. Figure 3.14 is an example of this comparison for the pre-stall data point  $\alpha=0^\circ$  showing a very good match between CFD and experimental measurements. Note that only certain  $\eta$  stations had both upper and lower pressure port measurements available.

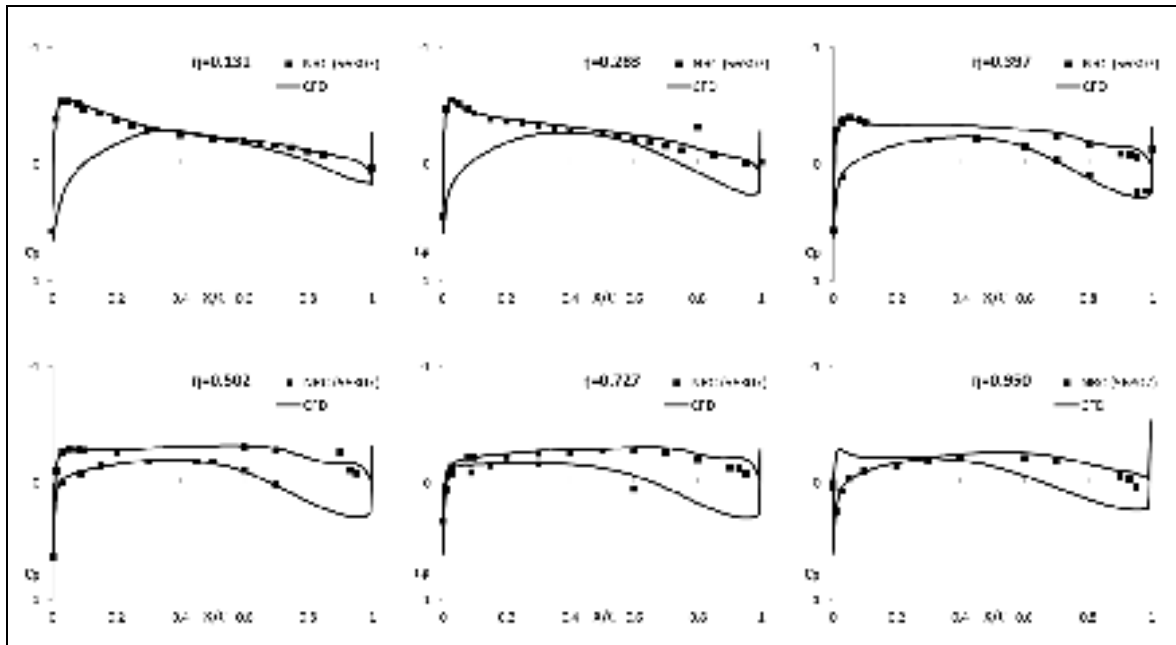


Figure 3.14 CFD predicted wing pressure distributions at  $\alpha=0^\circ$  compared to NRC experimental ventilated-wall results (run 56307) at  $\alpha=0.08^\circ$ .

Judging by the results shown in Figure 3.13, CFD results at higher angle of attack show a premature flow separation with a more sudden loss of lift relative to the experimental findings. While reliable in typical cruise flow conditions, it is more challenging for CFD to achieve similar levels of accuracy for significantly separated flow (stall) in aircraft applications. Figure 3.15 shows the CFD predicted development of flow separation on the suction side of the NASA CRM wing as the tested angle of attack increases, based on the x-component of the skin friction coefficient.

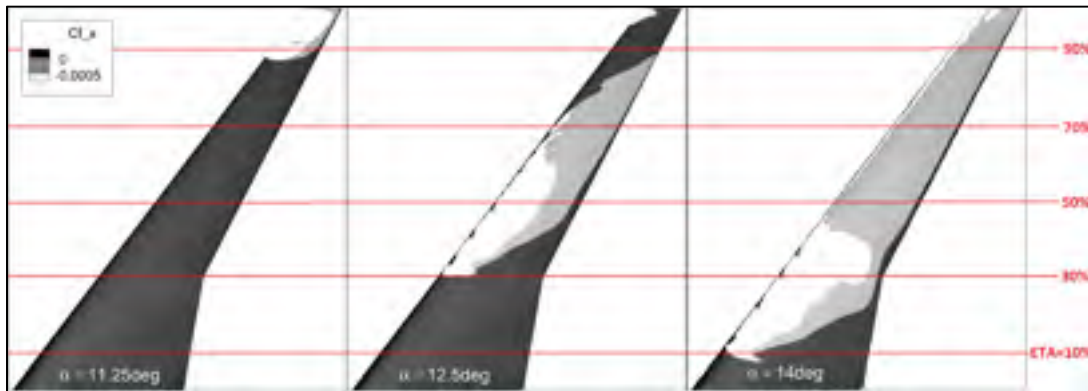


Figure 3.15 CFD-predicted evolution of the flow separation over the CRM wing. The x-component of the skin friction coefficient vector is used to indicate flow separation on the suction side of the wing.

To quantify a potential over-prediction of the flow separation observed in the computational results for the model at higher angle of attack, the experimental (ventilated-wall) and numerical wing pressure distributions are compared in the same manner as previously presented for the attached flow region. Figure 3.16 presents an example of this comparison at  $\alpha=11.25^\circ$  with very good agreement between CFD and experimental data. The pressure plateau on the suction side of the outboard region of the wing,  $\eta=0.950$ , shows evidence of flow separation. However, Figure 3.17 ( $\alpha=14^\circ$ ) indicates that at higher angle of attack, the computational and experimental results differences grow larger. Although both exhibit flow separation on the outboard section of the wing, the integral of the pressure coefficient along the complete airfoil is generally lower in the CFD results. Consequently, lower lift is predicted by the RANS simulations.



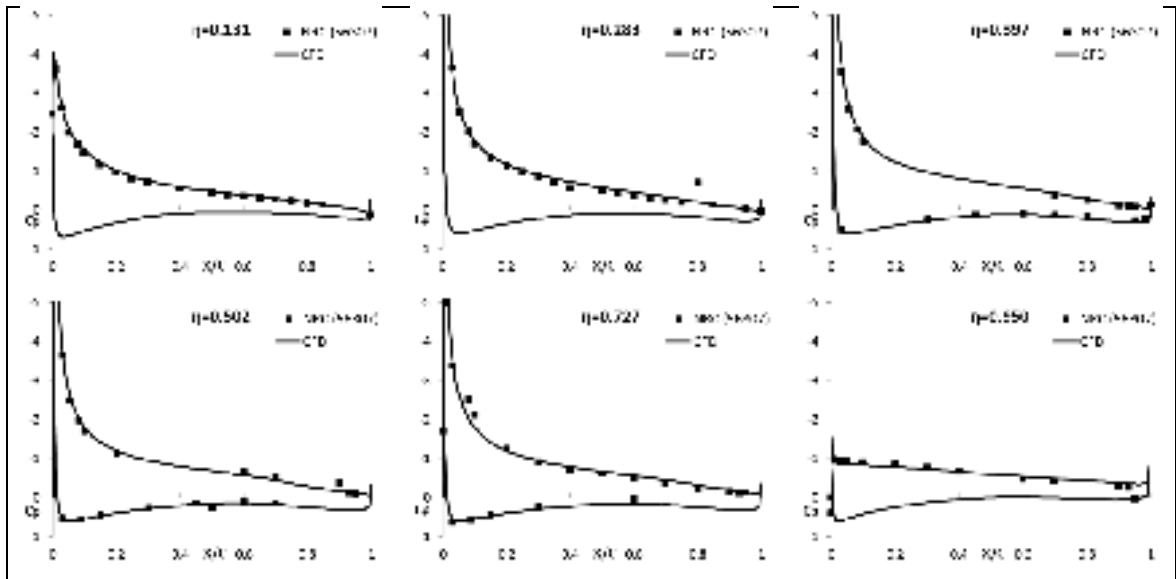


Figure 3.16 CFD predicted wing pressure distributions at  $\alpha=11.25^\circ$  compared to NRC experimental ventilated-wall results (run 56307) at  $\alpha=11.29^\circ$ .

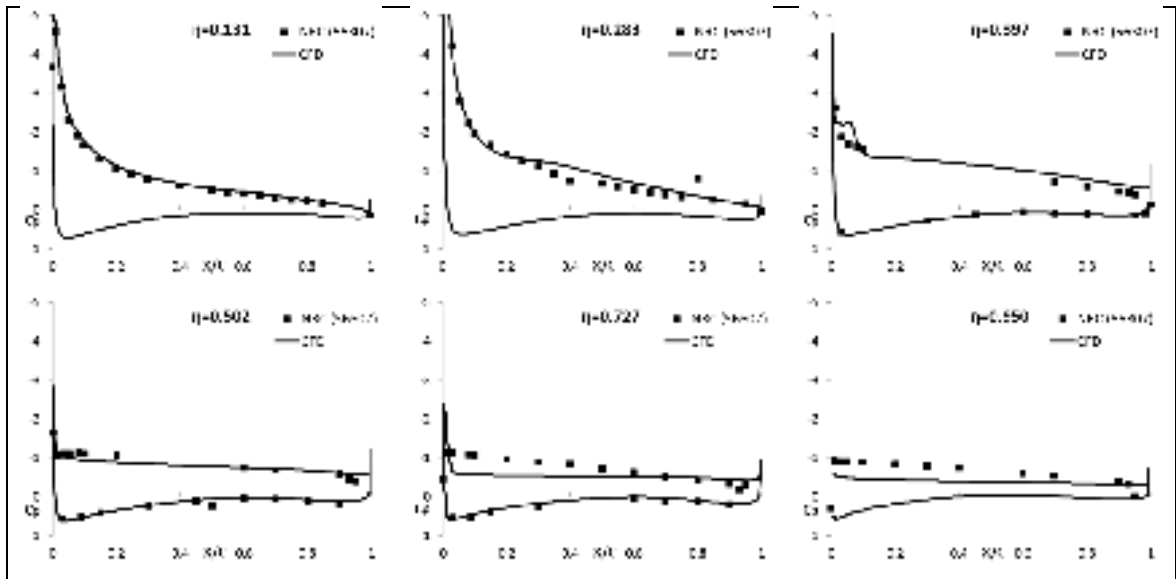


Figure 3.17 CFD predicted wing pressure distributions at  $\alpha=14^\circ$  compared to NRC experimental ventilated-wall results (run 56307) at  $\alpha=13.93^\circ$ .

### 3.4 The use of CFD to improve and validate wall corrections

One of the goals of the work addressed in this document is to improve the singularity representation of the test article. It could be argued that Euler or Navier-Stokes CFD simulations would provide a more accurate farfield solution than potential flow methods within wall-correction algorithms. However, for properly chosen potential flow model representations at suitable distances from the test article, the gains of a CFD solution are insignificant and its cost in time and processing is many orders of magnitude greater than the potential flow methodology. In addition, the CFD solution would have to be tuned or iterated on until it matches the experimental data point.

In spite of the unsuitability of the use of CFD simulations in real-time production tests, the use of CFD may be implemented as a benchmark to assess the potential flow representation of the test article currently in use by the one-variable method and to validate the accuracy of the wall corrections calculated. An accurate farfield solution of the flow around the model in free-air is of equal importance compared to the measurement of the boundary velocities for obtaining reliable wall corrections using the one-variable method. This requirement becomes particularly critical in semispan wind-tunnel testing, where the tunnel walls are generally closer (not so farfield) relative to full span testing. In pre-stall conditions, the free-air farfield results generated by the current potential-flow representation of the test article can deliver reliable wall-correction results, given all the salient flow features of the model are dealt with. However, at test conditions where, for example, flow separation on the test article becomes significant, the farfield obtained using the existing (streamlined, lifting aircraft) potential-flow model representation lacks the accuracy to expect reliable wall corrections (Toledano *et al.*, 2016).

To evaluate what level of bias errors some of these potential-flow representation simplifications introduce into the semispan wall-interference corrections and to assess the effects of changes to the potential-flow model, numerical results from the high fidelity free-air CFD solutions for the aircraft model geometries considered are obtained and used as the in-tunnel measured flow field, as well as the model force and moment data for the given data point. The farfield results from the original or updated potential-flow singularity

representation of the tunnel model are then created for the CFD data point flow conditions and the “wall interference” is evaluated for the expected test section boundary location (of the NRC wind tunnel). Given that both calculations are made under free-air conditions (Figure 3.18), the wall corrections should be zero.

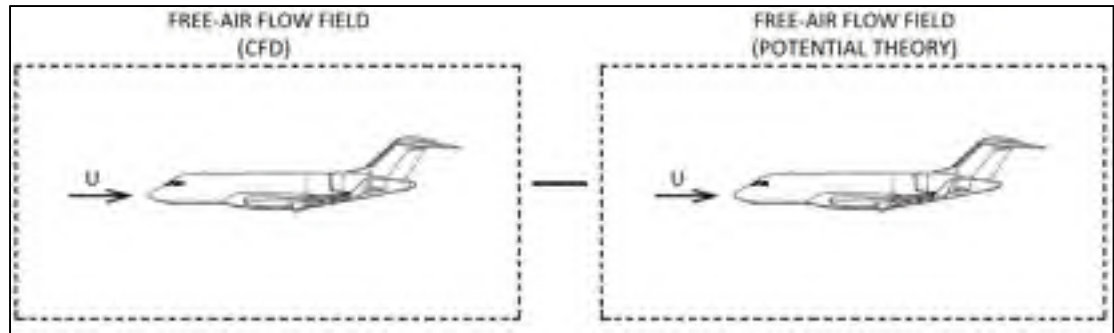


Figure 3.18 Theoretical “zero” wall interference described as the difference between CFD-predicted and potential theory free-air flow fields.

Significant corrections of either angle of attack ( $\Delta\alpha$ ) or Mach number ( $\Delta M$ ), would indicate that the simplified potential-flow model is not sufficiently accurate for the case, and bias errors of similar magnitude can be expected in the corrections for a real wind-tunnel data point under similar conditions. Establishing an uncertainty budget is necessary to determine the validity of the results (Walker, 2005). For this study, the significance of the “zero-correction” results has been adopted from Steinle and Stanewsky uncertainty budgets established in their 1982 AGARDograph 184 publication, which provides guidance to set the acceptable flow quality and data accuracy limits in subsonic and transonic wind-tunnel test results.

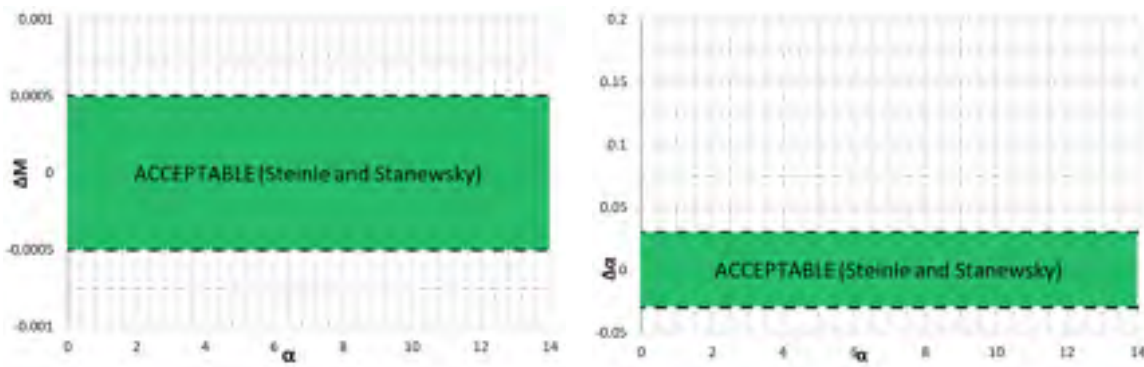


Figure 3.19 Mach and angle-of-attack “zero-correction” uncertainty budget based on AGARDograph 184.

The acceptable boundaries considered in this dissertation are inspired by uncertainty budgets for high lift testing applications. For this mode of testing, uncertainty in the Mach number and angle of attack of  $\pm 0.0005$  and  $\pm 0.03$  respectively, are generally acceptable (see Figure 3.19).

The previously introduced NASA Common Research Model (CRM) in its fuselage only (B) and wing/body (WB) configuration has been the test article considered to perform both free-air CFD simulations and experimental wind-tunnel tests at subsonic flow in a half-model configuration.

## CHAPTER 4

### RESULTS

The motivation for this research project comes in great part from the room for improvement that can be found in the one-variable method currently applied in the NRC 5ft TWT on subsonic tests performed on semispan models at high incidence, as introduced in § 1.4. Fruit of the combined analysis of the available wind-tunnel experimental data and the numerical simulations completed along this research project, a series of results have been achieved to satisfy the goals defined at the beginning of this dissertation.

#### **4.1 Parametric study on semispan models tested at the NRC 5ft TWT**

As described at the end of chapter 1, an offset existed between the angle of attack wall corrections obtained with the one-variable method and those obtained through traditional textbook methods. This motivated a parametric study to try to determine the source of the disagreement. All the results addressed in this section are related to the wall corrections calculated for the solid-wall boundary test of the Bombardier Global 6000 (run 1271 in Table 1.3).

First, the sensitivity of the position of the upstream and downstream faces of the computational boundary surface of the panel method (described in § 1.3) was evaluated. Originally, the upstream face was located 90 inches upstream from the balance centre ( $X_{\text{ups}}=-90''$ ), close to the first upstream pressure tap located at  $X=-87.5''$ , and the downstream face was 50 inches downstream from the turntable centre ( $X_{\text{downs}}=50''$ ); as seen in Figure 4.1.

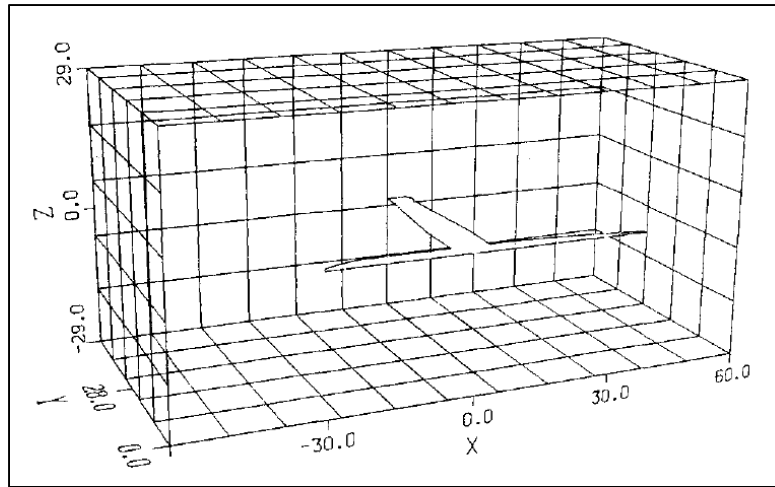


Figure 4.1 Computational boundary for panel method.  
From: Mokry *et al.* (1987).

A number of combinations for this geometry were tested and the best results were obtained for  $X_{\text{ups}}=-100''$  and  $X_{\text{downs}}=50''$ , for which the angle of attack correction offset observed was slightly diminished and the  $\Delta\alpha/C_L$  slope matched theoretical ESDU results (Figure 4.2). Also, the number of streamwise subdivisions of the boundary surface was increased from the original 11 subdivisions (Figure 1.18), but no significant improvements were experienced.

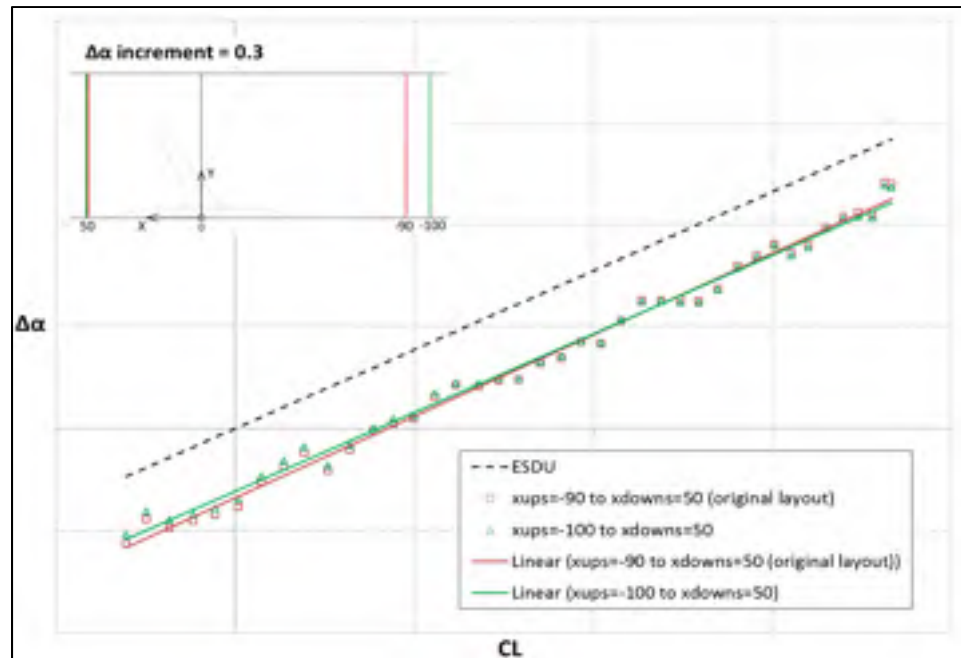


Figure 4.2 Results from the computational boundary surface parametric study using solid-wall experimental data from a test performed on the Bombardier Global 6000 model.

Following the parametric study of the computational boundaries, the referencing of the experimental static pressure measurements of the pressure rails was investigated. Due to experimental noise issues, the standard practice had been to shift all the boundary pressures of each electronically scanned pressure module such that one of its upstream pressure measurements is forced to a  $C_p=0.0$  state. The required offset was also applied to all the pressure measurements on the same module. This raised the question of whether this procedure was responsible for the  $\Delta\alpha$  offset with respect to ESDU-based corrections. To investigate this, each set of rail pressures was offset to force an upstream pressure tap to read the pressure coefficient expected at that location in the “free-air” condition (calculated by means of a potential-theory singularity model representation) as opposed to  $C_p=0.0$ . The results show that this modification did not change the offset at zero lift (Figure 4.3).

However, the slope of the angle-of-attack correction versus lift coefficient curve now does not match theoretical predictions based on ESDU 95014 (1995), indicating this new practice was not appropriate.

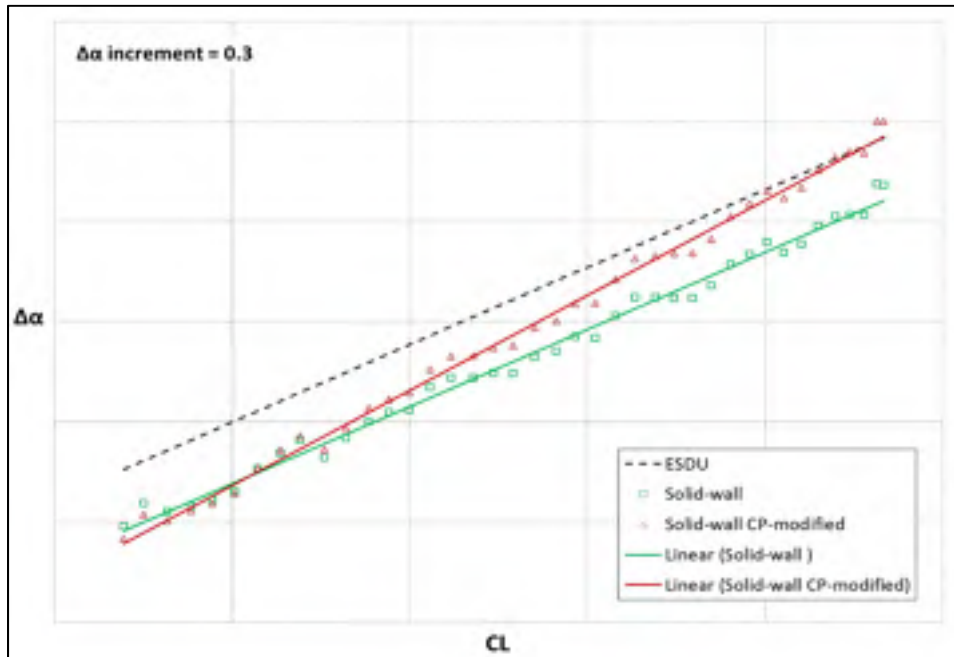


Figure 4.3 Results from the reference pressure re-adjustment using solid-wall experimental data from a test performed on the Bombardier Global 6000 model.

During the solid-wall boundary wind-tunnel experiments, the influence of the splitter plate that forms the reflection plane was also examined. As it was explained in chapter 1, the effect of the side-wall boundary layer over the half-fuselage can represent a significant interference during semispan model tests. This can be minimized by using splitter plates or standoffs to relocate the model at a distance where better flow quality can be provided (Gatlin *et al.*, 1997). Typically, the upstream edge of the reflection plane is a splitter plate located about 62 inches upstream from the center of the turntable (Figure 4.4).



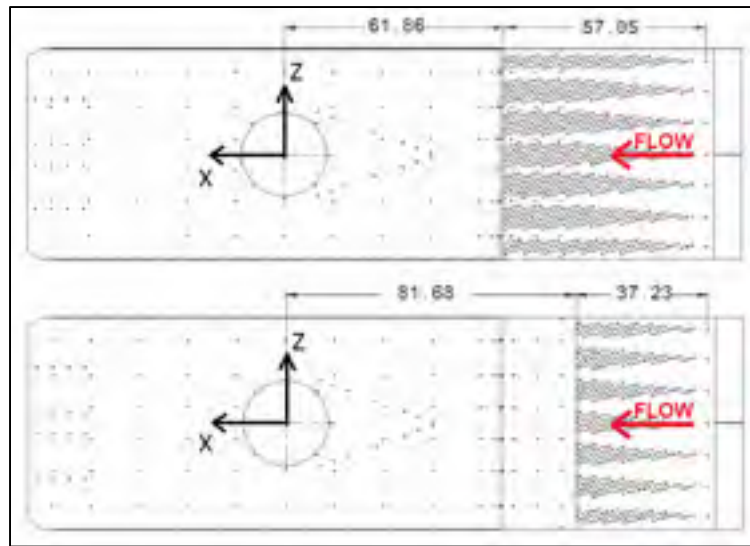


Figure 4.4 Original (top) and extended (bottom) versions of the NRC TWT reflection plate.

A 20-inch upstream extension of the reflection plate was installed to improve the flow quality/symmetry of the half-model test section configuration. This data set, corresponding to run 1272, was performed in the exact same conditions as run 1271 (Table 1.3) with the only difference of using the extended reflection plate. The corrections results obtained with the extended reflection plate were significantly closer to those predicted by theory, due to a reduction in the offset on the angle-of-attack correction versus lift coefficient curve (Figure 4.5), with no difference in terms of the measured uncorrected model forces and moments. These results do not indicate what is the ultimate root cause of the “offset problem” and additional considerations like the implications of the specific (6%) porosity setting of the side-wall behind the reflection plate must be considered to further study this phenomenon. However, they highlight the importance of good flow quality to obtain satisfactory wind-tunnel results.

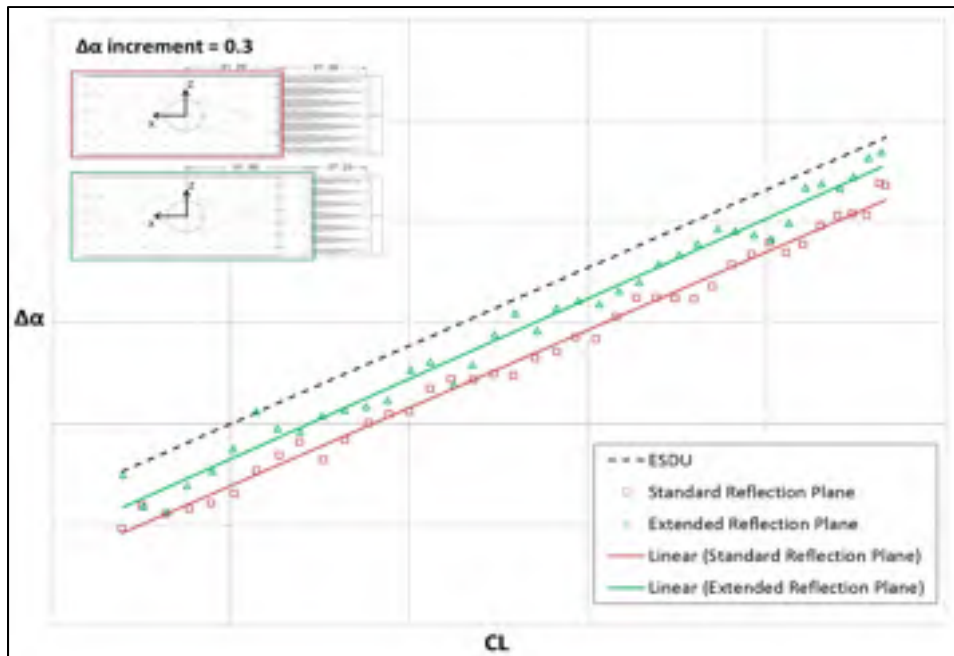


Figure 4.5 Results from the study of the influence of the reflection plane extension using solid-wall experimental data from a test performed on the Bombardier Global 6000 model.

## 4.2 CFD-based Validation of the Complete Wall-Correction Algorithm

Although relevant to any typical transport aircraft semispan model tested at the NRC Trisonic Wind Tunnel, the results presented in the remainder of this chapter were drawn from the experimental and numerical data obtained from the NASA Common Research Model test campaign completed in 2016 at the TWT.

The data obtained from the free-air CFD RANS simulations performed for the 2.7% scale semispan geometry of the NASA CRM WB provide an opportunity to validate the wall-correction method used at the NRC 5ft TWT without the need for experimental wind-tunnel measurements. For the purpose of this validation, the wall-interference calculation code was modified to take as input the wall pressure signature and the model forces obtained from the free-air CFD RANS results. It may be worth it to remind that those model forces are used in the potential theory representation of the wind-tunnel model to calculate the flow behavior around the test article (in the farfield) in free-air. If the

methodology operates correctly, the corrections obtained should be zero, since CFD results in free-air are being compared to a potential theory estimation of the flow behavior, also in free-air.

Figure 4.6 shows the Mach number and angle of attack corrections obtained from these validation tests. The results in the attached flow region match the expectations; as  $\Delta M$  and  $\Delta \alpha$  are practically zero. The limits for “zero” are best estimated by the purposes of the wind-tunnel test. As introduced in the methodology section, this particular application is for take-off and landing, where the acceptable uncertainty budgets for Mach number and angle of attack are  $\pm 0.0005$  and  $\pm 0.03$  respectively, as indicated by Steinle and Stanewsky (1982). At stall conditions, significant correction in  $\Delta \alpha$  is obtained. This aligns with the previously introduced idea that, at high angles of attack where flow separation is significant, there is a significant disagreement between the estimated “wall” pressure signature estimated using the current potential theory representation of the test article and that actually being produced by the article in free-air.

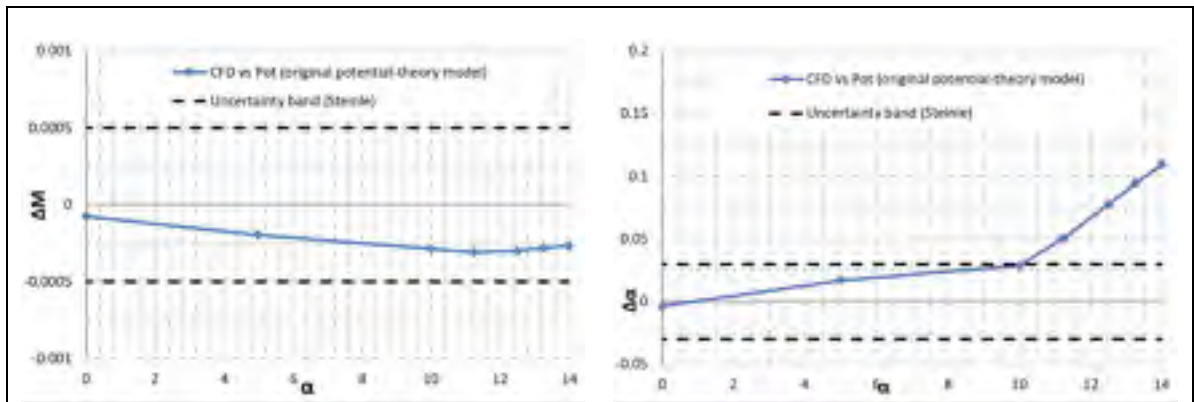


Figure 4.6 Validation of the one-variable method using free-air CFD results as input.

This procedure represents a CFD-based alternative to validate the wall-correction methodology and proves that, while reliable in the attached-flow region, the one-variable method requires improvement as flow separation develops on the tunnel model. The following sections describe how the methodology may be improved by updating the potential-flow representation of the test article.

### **4.3 Improvement of the current non-pitching Rankine body fuselage representation**

At the NRC 5ft TWT, relatively long models are used for take-off and landing investigations. Due to the wide range of angles of attack tested, there was concern that the currently employed non-pitching Rankine body introduced a significant bias error. For this reason, the first investigation launched to improve the potential flow representation of the test article in the wind tunnel involved the evaluation and update of the fuselage representation. The geometry considered was that of the fuselage of the 2.7% scale model of the NASA CRM tested at angles of attack ranging from  $0^\circ$  to  $30^\circ$  at low-speed ( $M=0.2$ ) subsonic flow.

The current fuselage representation (Mokry, 1985) used at the NRC 5ft TWT consists of a Rankine body of strength  $m$  formed by a source (located at a distance  $d$  downstream of the fuselage nose) and a sink of equal strength (located at a distance  $d$  upstream of the fuselage tail) on a line parallel to the stream direction (Figure 4.7) at the mid height of the cylindrical section of the fuselage. The Rankine body strength  $m$  is a function of the source and sink position. As the model pitches, the nose and tail positions are projected on the x-axis and these are used to locate the source and sink.

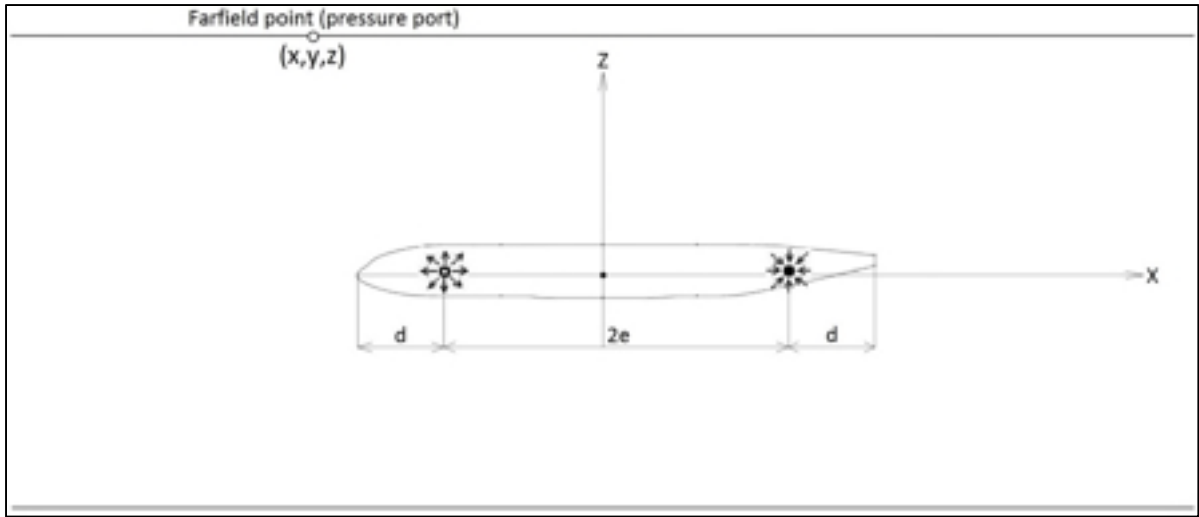


Figure 4.7 Rankine body fuselage representation over sketch of the CRM fuselage relative to the NRC 5ft TWT boundary location.

The distance  $d$  can be determined as a function of the eccentricity  $e$  of both singularities (the source and the sink) with respect to the Rankine body half-axes. In a more practical approach, as presented by other authors such as Ulbrich (1998),  $d$  can be made equal to the fuselage radius. The current fuselage representation calculates  $e$  as specified by Vallentine (1967). The velocity potential due to the Rankine body  $\phi_{Rankine}$  at a specific  $(x, y, z)$  location obeys Eq. (4.1), where  $\beta = \sqrt{1 - M^2}$  is the Prandtl-Glauert compressibility correction factor.

$$\phi_{Rankine}(x, y, z) = \frac{m}{4\pi} \left[ \frac{-1}{\sqrt{(x+e)^2 + \beta^2 y^2 + \beta^2 z^2}} + \frac{1}{\sqrt{(x-e)^2 + \beta^2 y^2 + \beta^2 z^2}} \right] \quad (4.1)$$

For a specific wind-tunnel model, like the 2.7% scale semispan model of the NASA CRM considered in this study, the geometry specifications required for the Rankine body fuselage representation include the fuselage radius  $r$  and the positions of the nose and the tail.

To assess the limitations of the current Rankine body fuselage representation over a range of angles of attack  $\alpha$ , free-air “wall” pressure signatures are calculated by applying the velocity potential  $\phi_{Rankine}$  to the equation of the linearized subsonic pressure coefficient  $C_p = -2(\partial\phi/\partial x)$ . These pressure signatures are then compared to those obtained using Euler CFD simulations of the NASA CRM (fuselage only).

Figure 4.8(a) shows the pressure signature at the Top North (TN) pressure rail using the potential flow representation of the Rankine body. Almost identical flow field results are obtained over a range of angles of attack from  $\alpha=0^\circ$  to  $\alpha=30^\circ$ , showing small changes observed for the various angles due to the projection of the nose and tail onto the x-axis which changes with increasing angles of attack. As expected, the signature is exactly symmetrical about the midpoint of the Rankine body. Figure 4.8(b) shows the results of the “wall” pressure signatures estimated at the Top North pressure rail using CFD results at the same location. In this case, the pressure distribution depends on  $\alpha$  and presents asymmetrical signature even at  $\alpha=0^\circ$  as a result of the fuselage having an asymmetrical volume distribution from nose to tail. At angles of attack less than  $10^\circ$  the Rankine body representation is satisfactory. For angles above this or for models with highly asymmetrical volume distributions the existing Rankine body is unsatisfactory.

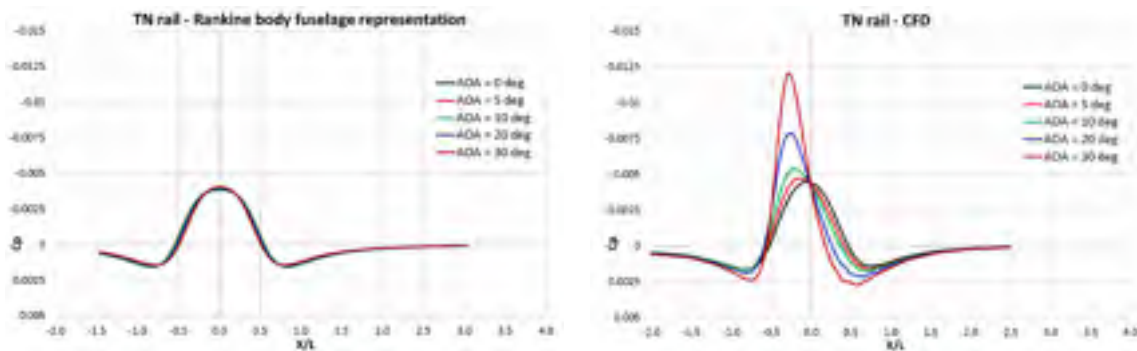


Figure 4.8 Pressure signature at the Top North (TN) rail location comparing (a) the Rankine body fuselage representation to (b) a CFD simulation of the actual 2.7% scale NASA CRM fuselage.

Additionally, as described in the last section of the methodology, “zero-corrections” (i.e., wall corrections calculated for the CFD-predicted free-air flow field) were computed to assess the validity of the Rankine body fuselage representation. The resulting flow field from the free-air Euler CFD simulations of the NASA CRM fuselage was used to calculate the pressures at the same locations in space as the wind-tunnel boundary rails. These results, together with the CFD-predicted forces and moments were used as the “experimentally” measured pressure and balance data. The data points considered were corrected using the “one-variable” method that made use of the Rankine body potential-flow representation to obtain results of the “wall interference”. As seen in Figure 4.9, the estimated “wall corrections” ( $\Delta M$  and  $\Delta \alpha$ ) required to bring the tunnel data to “free-air” are negligibly small at low angles of attack, while at angles of attack above  $\alpha=8^\circ$ ,  $\Delta \alpha$  is at or above the uncertainty budget for angle of attack. This clearly indicates that for a model of this size in this test section, a more complex potential-flow model is needed.

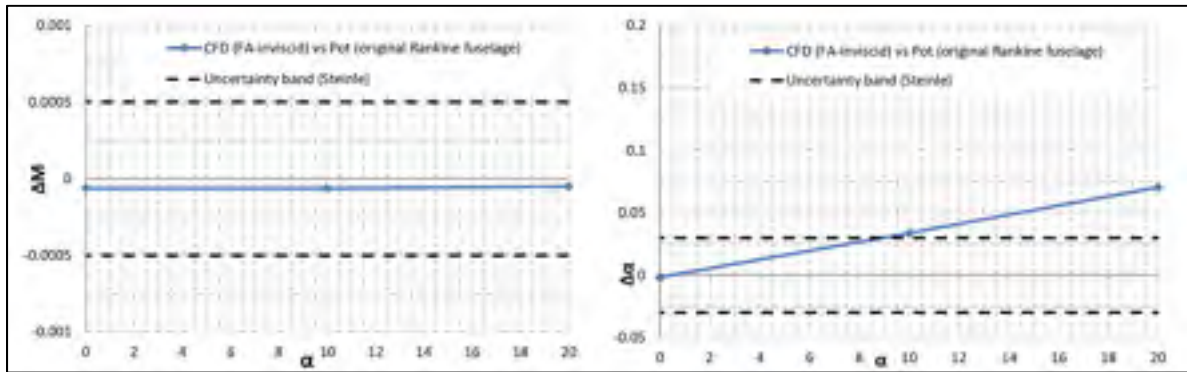


Figure 4.9 Error band for Mach number and angle of attack corrections computed using the one-variable method applying the original fuselage representation of the CRM.

To improve upon the Rankine body representation, a new fuselage singularity representation was developed based on the slender body theory applications presented by Katz and Plotkin (2001) and Schlichting (1979). Both authors present the possibility of representing an

axisymmetric body of varying cross sectional area aligned with the flow ( $\alpha=0^\circ$ ) by a number of sources/sinks (either one or the other in each singularity location) and a similar body in a transverse flow ( $\alpha \neq 0^\circ$ ) by a number of point doublets oriented to the negative local  $Z'$  fuselage axis.

For the test conditions that a fuselage typically encounters in the NRC 5ft TWT, a combination of sources/sinks and doublets was implemented and tested to find how suitably they would represent the flow around the model. The number of singularities used was  $n$  sources/sinks (one or the other depending on the gradient of the fuselage cross-sectional area) and  $n$  doublets. The number of singularities  $n$  is approximately equal to the fuselage length  $L$  divided by the fuselage radius  $r$ , which is aligned with the work of Vaucheret (1982). For the NASA CRM fuselage geometry,  $n=22$ . The singularities are evenly distributed from nose to tail so that if the centerline is divided into  $n$  sections  $j=1$  to  $n$  of length  $dx$ , there will be either a source or a sink of strength  $\sigma$  and a doublet of strength  $\mu$  at the position  $(x_j, y_j, z_j)$ , in the middle of  $dx$ . The velocity potential due to a source (or sink) of strength  $\sigma$  and a doublet of strength  $\mu$  is expressed by Eqs. (4.2) and (4.3), respectively. Figure 4.10 shows a sketch of the singularity distribution in the updated fuselage representation relative to the NRC 5ft TWT pressure rails distribution.

$$\phi_{\text{source-sink}}(x, y, z) = \frac{-\sigma}{4\pi} \cdot \frac{1}{\sqrt{(x - x_j)^2 + \beta^2(y - y_j)^2 + \beta^2(z - z_j)^2}} \quad (4.2)$$

$$\phi_{\text{doublet}}(x, y, z) = \frac{-\mu}{4\pi} \cdot \frac{-\beta(z - z_j)}{[(x - x_j)^2 + \beta^2(y - y_j)^2 + \beta^2(z - z_j)^2]^{3/2}} \quad (4.3)$$



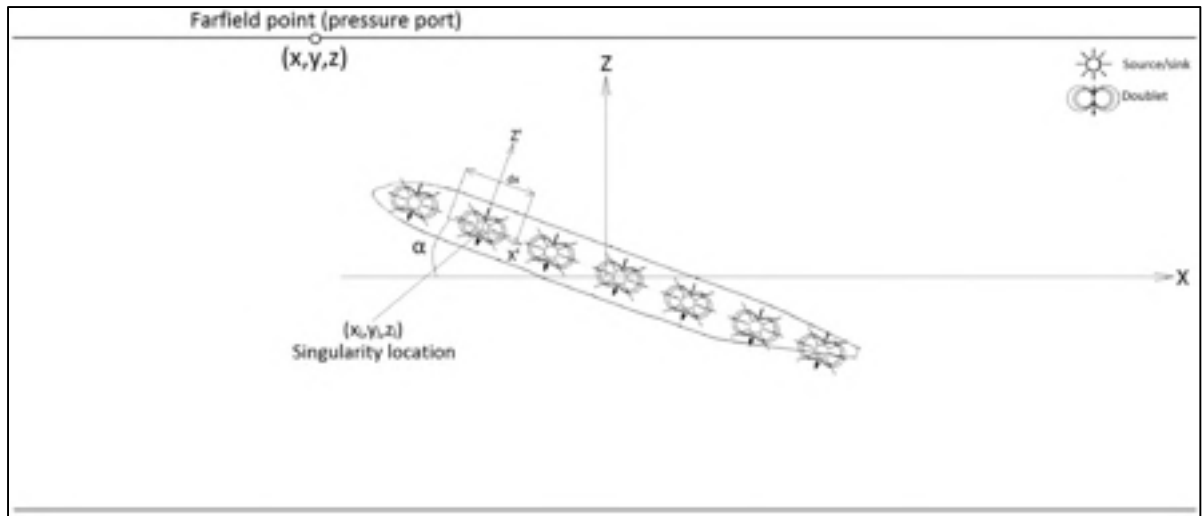


Figure 4.10 Singularity distribution in the updated fuselage representation over sketch of the CRM fuselage relative to the NRC 5ft TWT boundary location.

Whereas the strength  $\sigma$  of the source/sink located at  $(x_j, y_j, z_j)$  depends only on the gradient of the fuselage cross-sectional area with respect to the location of the previous upstream source/sink located at  $(x_{j-1}, y_{j-1}, z_{j-1})$ , the doublet strength  $\mu$  is a function of the angle of attack  $\alpha$ , the distance  $dx$  (zone of influence of that specific doublet) and the fuselage cross-sectional area at the doublet location. The strengths of the singularities at the fuselage nose and tail are set to satisfy the closure condition, as described by Schlichting (1979). Compared to the Rankine body, the only additional model geometry specification required for this new fuselage representation is the fuselage cross-sectional area at each singularity location, which in any case is typically provided to the testing facility to determine the buoyancy drag correction.

The results obtained following an identical validation methodology as described above using the 2.7% scale NASA CRM fuselage geometry are promising. As seen in Figure 4.11, the “wall” pressure signatures obtained using the updated potential flow representation of the fuselage match those obtained by the inviscid CFD simulation for the whole range of  $\alpha$ .

Comparing Figure 4.10 and Figure 4.11, the improvement obtained by the use of the updated fuselage representation may be demonstrated.

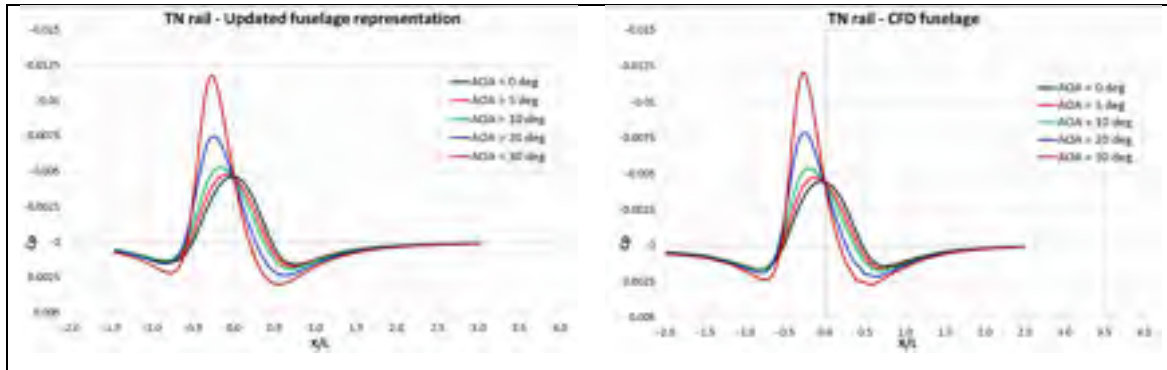


Figure 4.11 Pressure signature at the Top North (TN) rail comparing (a) the updated fuselage representation to (b) a CFD simulation of the actual 2.7% scale NASA CRM fuselage.

For a more complete analysis of the updated potential flow representation of the fuselage, a detailed rail-by-rail (see Figure 1.8 for pressure rails layout at the TWT) comparison (Figure 4.12 to Figure 4.14) was performed showing an excellent agreement between the results achieved through potential theory and those obtained from the CFD simulation.

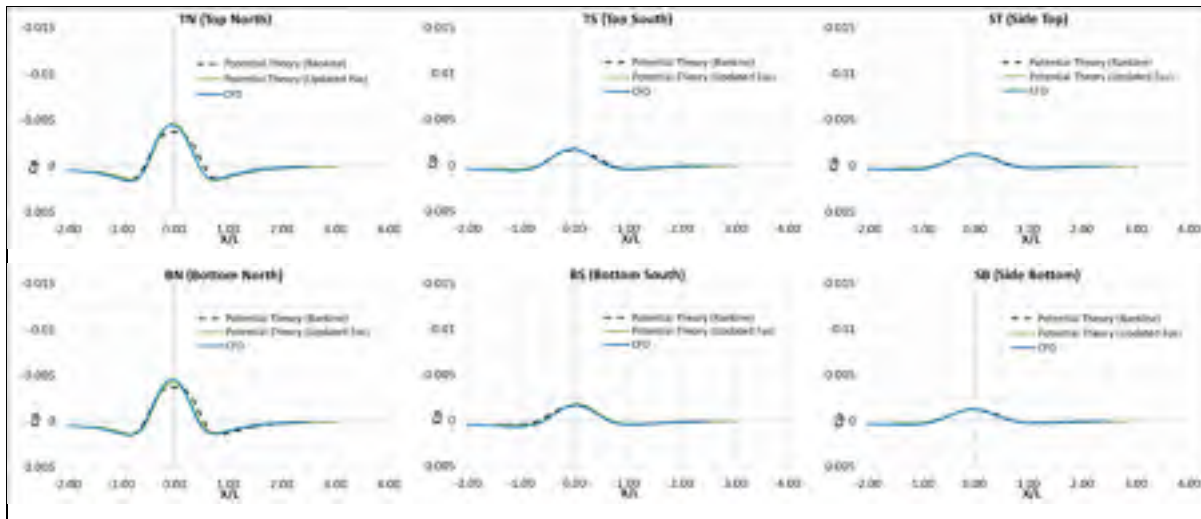


Figure 4.12 CFD validation of the  $n=22$  sources-sinks and  $n=22$  doublets fuselage representation for  $\alpha=0^\circ$ .

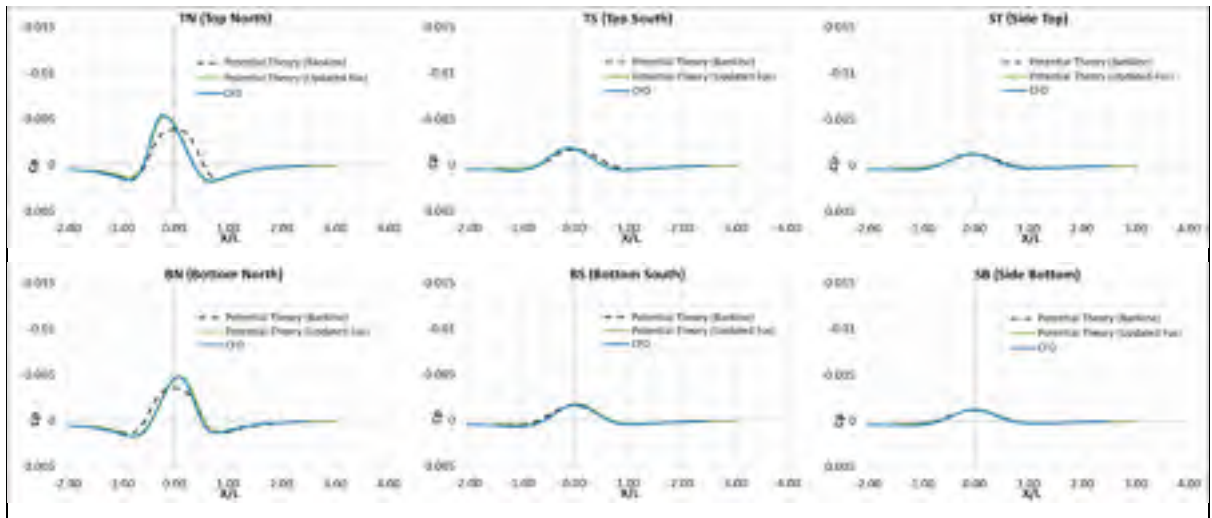


Figure 4.13 CFD validation of the  $n=22$  sources-sinks and  $n=22$  doublets fuselage representation for  $\alpha=10^\circ$ .

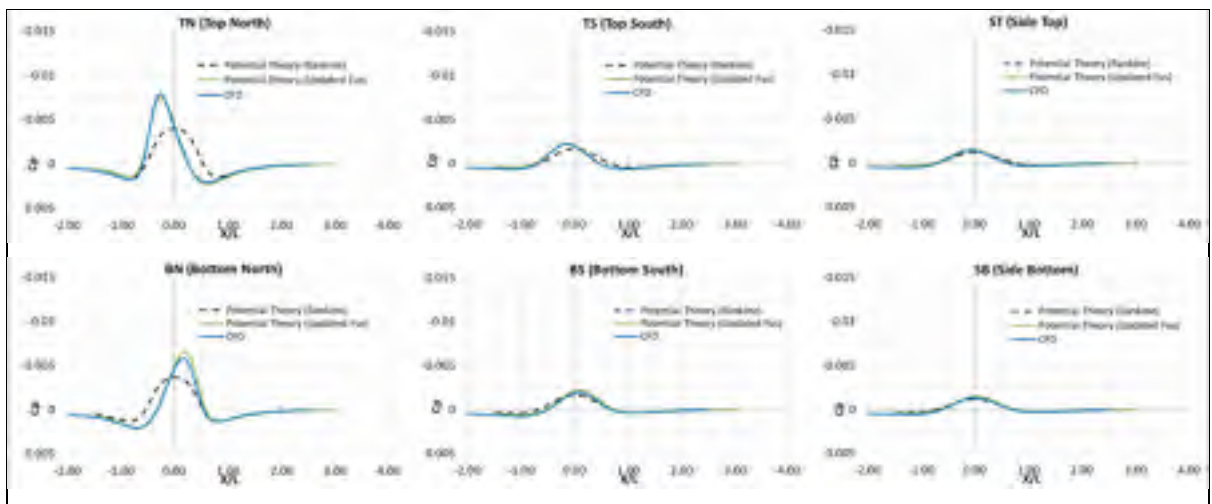


Figure 4.14 CFD validation of the  $n=22$  sources-sinks and  $n=22$  doublets fuselage representation for  $\alpha=20^\circ$ .

When this improved potential-flow representation is used to calculate “zero-corrections” for validation, as seen in Figure 4.15, the  $\Delta M$  error continues to be acceptably small and the  $\Delta\alpha$  “wall correction” is substantially reduced for all fuselage angles of attack, though it will still account for the full uncertainty budget at  $\alpha=20^\circ$ . It is interesting to note that the  $\Delta\alpha$  bias errors from the new fuselage representation have the opposite trend from the original representation (Figure 4.9), which suggests that further accuracy checks could be made of this representation.

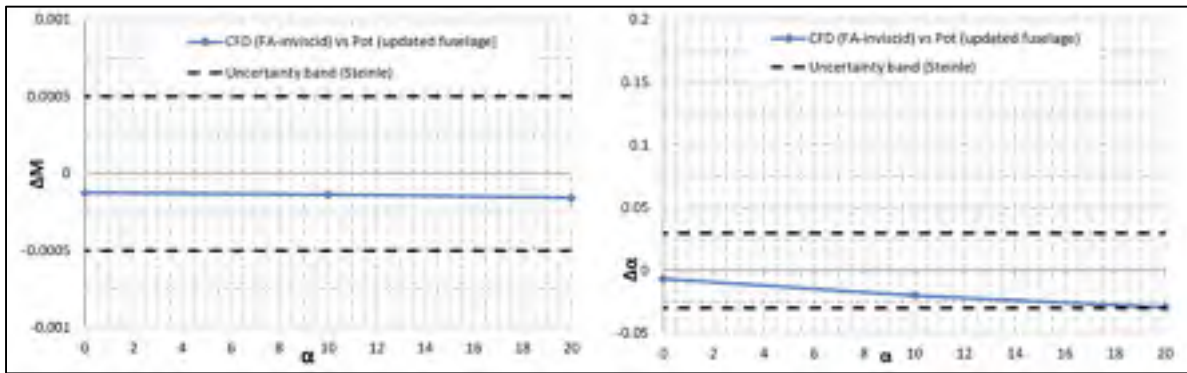


Figure 4.15 Error band for Mach number and angle of attack corrections computed using the one-variable method applying the updated fuselage representation of the CRM.

Overall, the results from this investigation indicate that the updated fuselage representation is ready to be implemented in real tests in the NRC 5ft TWT.

#### 4.4 Improvement of the current wing representation

Next, it was desired to assess the quality of the potential-flow representation of a typical transport aircraft model being tested at low speed. This provided an opportunity to assess the errors in the wall corrections when various levels of flow separation occur. As described in the methodology section, high fidelity RANS simulations were carried out for a semispan 2.7% cruise wing CRM WB (wing/body) model in free-air at  $M = 0.25$  and  $Re_c = 2.93 \times 10^6$  for a range of angles of attack reaching stall. In the same fashion as the fuselage study, the forces and moments of the free-air CFD simulation model, in addition to the flow field measurements in the vicinity of the “tunnel boundaries”, were treated as the wind-tunnel

experimental data and evaluated for “wall interference” using the wall-correction code at the NRC TWT. In this case, the fuselage representation was updated to that described in the previous section, implementing Eqs. (4.2) and (4.3).

In the current potential-flow representation (Mokry, 2006) of the half-model in free-air, the wing is modeled as a number of horseshoe vortices distributed along the quarter chord line to account for the model lift, assuming an elliptic lift distribution. The displacement effect of the wake and the volume effect of the wing are approximated by a discrete distribution of sources and doublets, respectively. In real tunnel tests, this representation requires basic parameters of the model’s wing geometry, as well as the measured model forces (lift and drag) to calculate the various strengths of its singularity distribution. In the following discussion, the model forces were obtained from the CFD simulations performed on the NASA CRM WB geometry. Figure 4.16 shows a sketch of the singularity distribution in the wing representation.

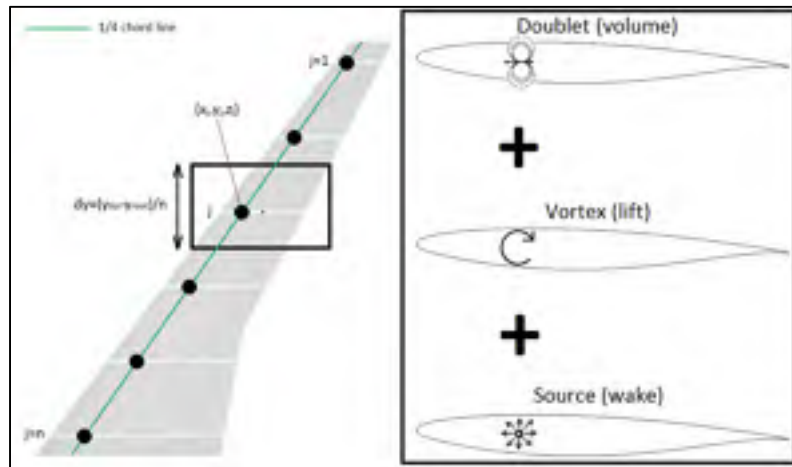


Figure 4.16 Sketch of the singularity distribution employed to represent the model’s wing.

The velocity potential due to the wing representation at a specific  $(x, y, z)$  location can be calculated as a linear superposition of that of the doublet, vortex and source distribution as determined by Eqs. (4.4) to (4.6). The strength  $\mu_j$  of the doublet located at  $(x_j, y_j, z_j)$  is a function of the product of the local chord and thickness, while the strengths of the vortex  $\Gamma_j$  and source  $\sigma_j$  at  $(x_j, y_j, z_j)$  are functions of the measured lift and drag, respectively.

$$\phi_{\text{volume}}(x, y, z) = \frac{1}{4\pi} \sum_j^n \mu_j \frac{x - x_j}{[(x - x_j)^2 + \beta^2(y - y_j)^2 + \beta^2(z - z_j)^2]^{3/2}} \quad (4.4)$$

$$\phi_{\text{lift}}(x, y, z) = \frac{1}{4\pi} \sum_j^n \Gamma_j \frac{z - z_j}{(y - y_j)^2 + (z - z_j)^2} \left( 1 + \frac{x - x_j}{\sqrt{(x - x_j)^2 + \beta^2(y - y_j)^2 + \beta^2(z - z_j)^2}} \right) \quad (4.5)$$

$$\phi_{\text{drag}}(x, y, z) = \frac{1}{4\pi} \sum_j^n \sigma_j \frac{1}{\sqrt{(x - x_j)^2 + \beta^2(y - y_j)^2 + \beta^2(z - z_j)^2}} \quad (4.6)$$

The “free-air” pressure signature at the rails can be obtained by applying the combination of the velocity potential due to both the fuselage (employing its updated representation described in the previous section) and the wing to the equation of the linearized subsonic pressure coefficient  $C_p = -2(\partial\phi/\partial x)$ . Figure 4.17 shows an example of a rail-by-rail comparison between RANS CFD simulation results and the potential-theory representation of the CRM WB configuration at  $\alpha=0^\circ$ . The results show a satisfactory agreement between the potential-theory signature and CFD. This was similarly found for any data point studied in pre-stall conditions.

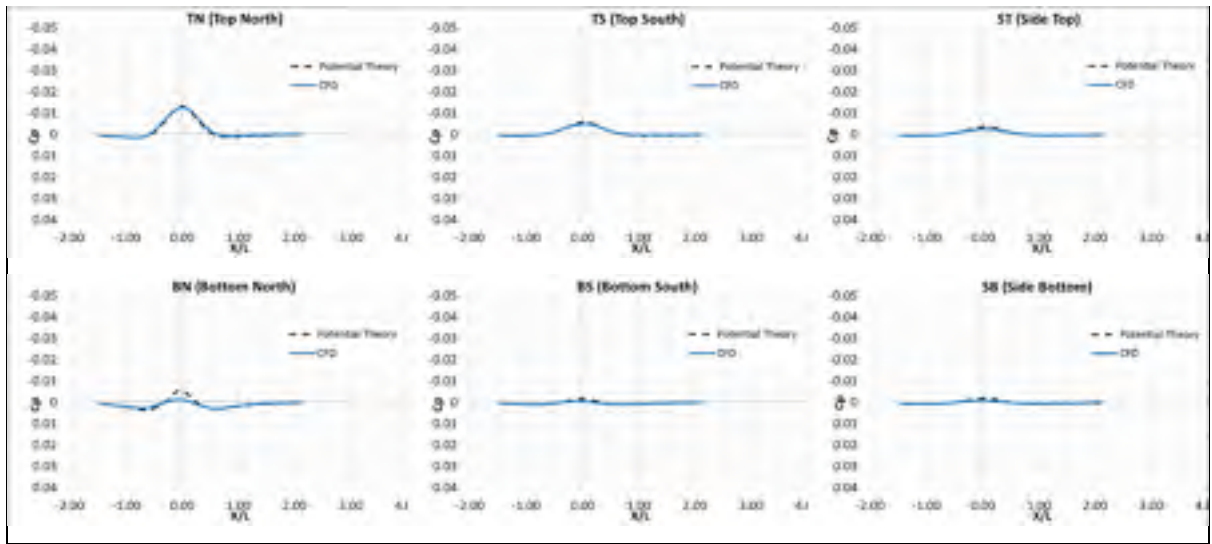


Figure 4.17 Comparison between the farfield pressure signature estimated by the potential-theory representation of the CRM and that predicted by CFD at  $\alpha=0^\circ$ ,  $C_L=0.195$ .

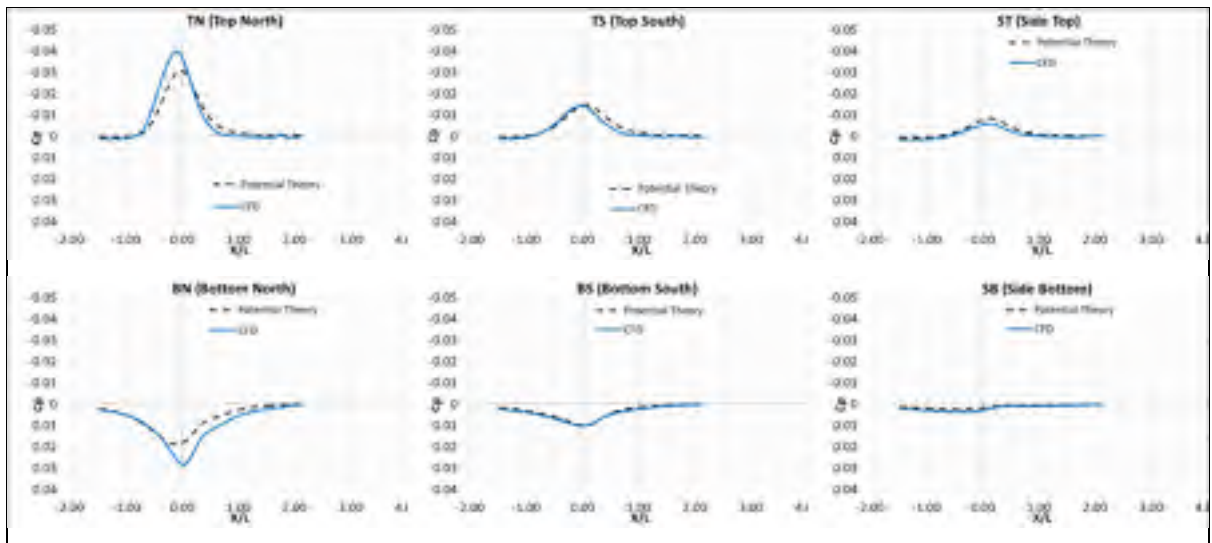


Figure 4.18 Comparison between the farfield pressure signature estimated by the potential-theory representation of the CRM and that predicted by CFD at  $\alpha=14^\circ$ ,  $C_L=1.033$ .

As the angle of attack increases, the potential-theory estimated wall pressure signature begins to show discrepancies with respect to that predicted by CFD, as it is unable to represent the developing flow separation on the model's wing. At high incidence, when flow separation begins to develop, the CFD predicted farfield inboard pressure signature is much larger than in the attached flow region (Figure 4.18).

For the CRM WB configuration, the “wall interference” bias errors of  $\Delta M$  and  $\Delta \alpha$  corrections are shown in Figure 4.19. It can be noticed that the desired low-level corrections for the low lift angles are achieved; validating that the potential-flow model meets adequate levels of accuracy according to the allowed uncertainty budget taken from Steinle and Stanewsky (1982). At stall conditions, a significant error correction in  $\Delta \alpha$  is obtained, exceeding these admissible limits. Unsurprisingly, the reason for this non-zero “wall interference” is the fact that the model has moderate to extensive regions of separation on the wing, and separation is not taken into account by the current potential theory representation of the test article.

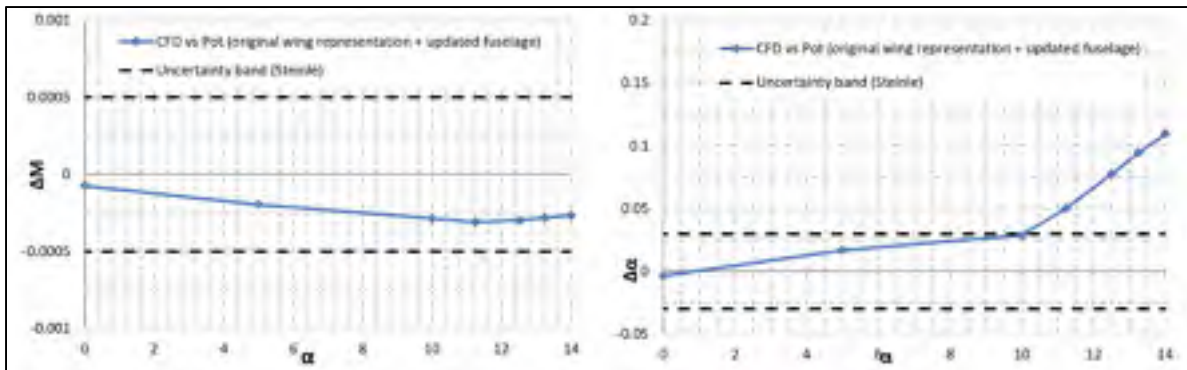


Figure 4.19 Error band for Mach number and angle of attack corrections computed using the one-variable method applying the original wing representation of the CRM WB.

The location and strength of each singularity needs to be revised using balance or other easily measured data. Using potential flow singularities, two different parameters were investigated to improve the model when flow separation becomes significant on the wing.



The first parameter understood not to be modeled correctly is the increased effective model volume due to the separated flow region on the wing. Numerical results reveal how a separation bubble begins to develop at the outboard section of the suction side of the wing, as Figure 4.20 illustrates.

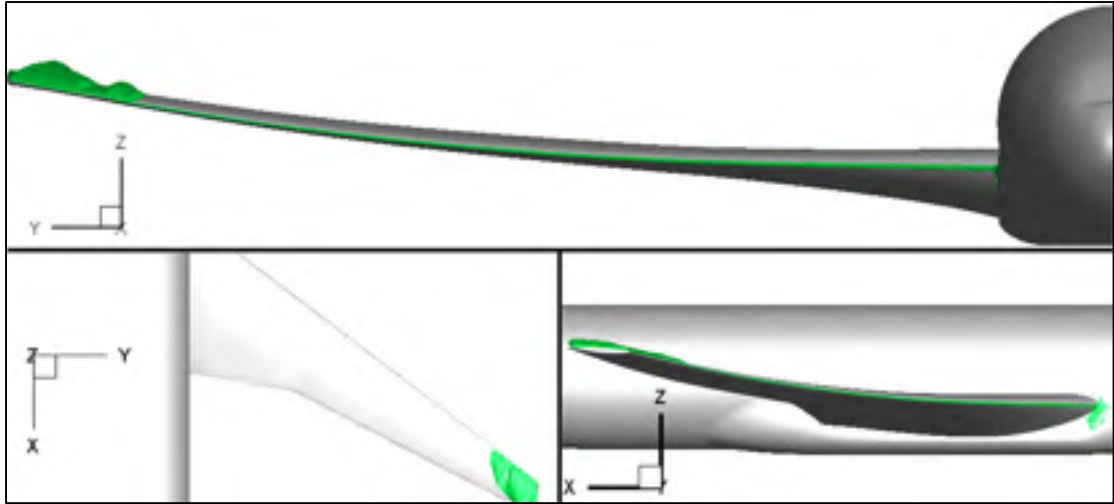


Figure 4.20 CFD predicted separation bubble at the CRM wing at  $\alpha=11.25^\circ$ .

Beyond this point, as the angle of attack approaches the stall point, the separation bubble continues to grow toward the inboard section of the suction side of the wing, as illustrated in Figure 4.21 for  $\alpha=14^\circ$ .

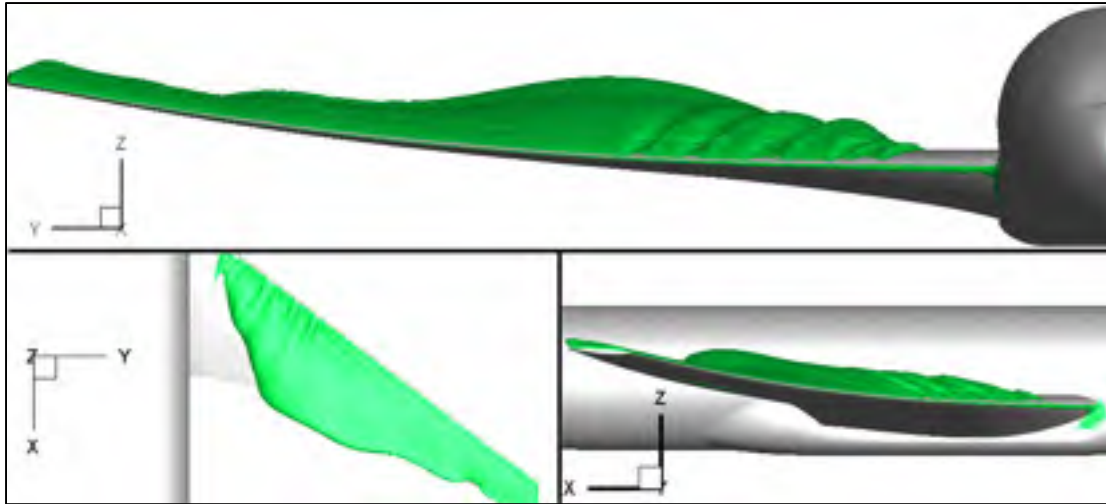


Figure 4.21 CFD predicted separation bubble at the CRM wing at  $\alpha=14^\circ$ .

A possible way of monitoring the growth of the separation bubble is by observing the development of reverse flow regions over the wing. Figure 4.22 presents an isometric view of the CRM WB where the separation bubble size is qualitatively estimated based on the bounded region at which the u-velocity is zero.

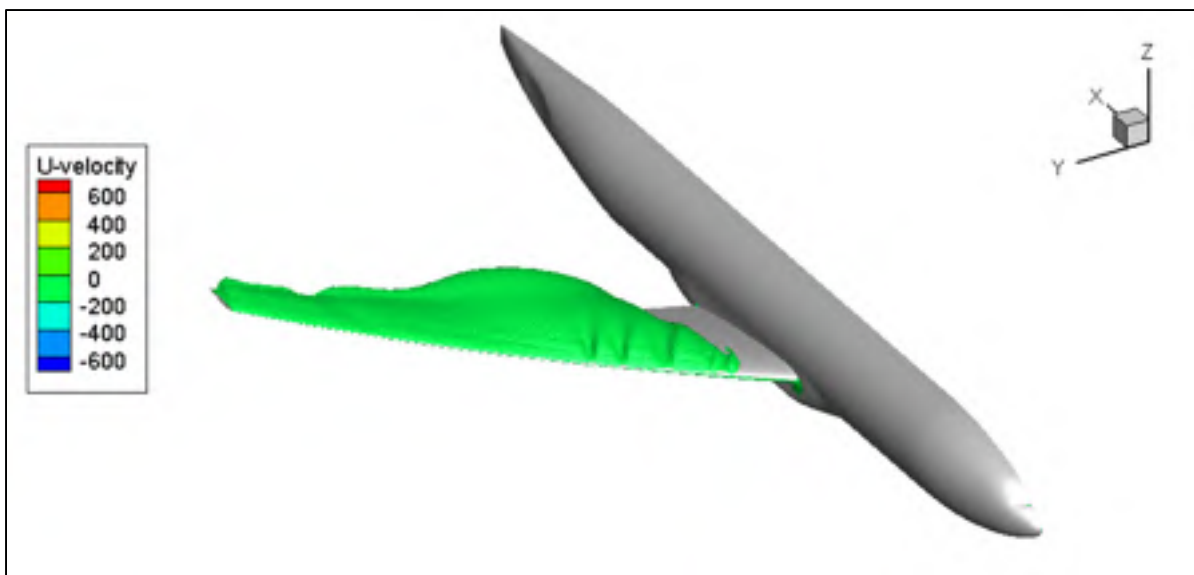


Figure 4.22 Qualitative estimation of the separation bubble size over the CRM WB at  $\alpha=14^\circ$ .

Inspired by different studies of the development and behavior of separation bubbles in laminar (Horton, 1968; and O’Meare *et al.*, 1987) and turbulent (Kiya *et al.*, 1982 and 1983; and Weiss *et al.*, 2015) flows, it was proposed as an improvement to represent this separated flow volume with point doublets located over the suction side of the wing (Figure 4.23).

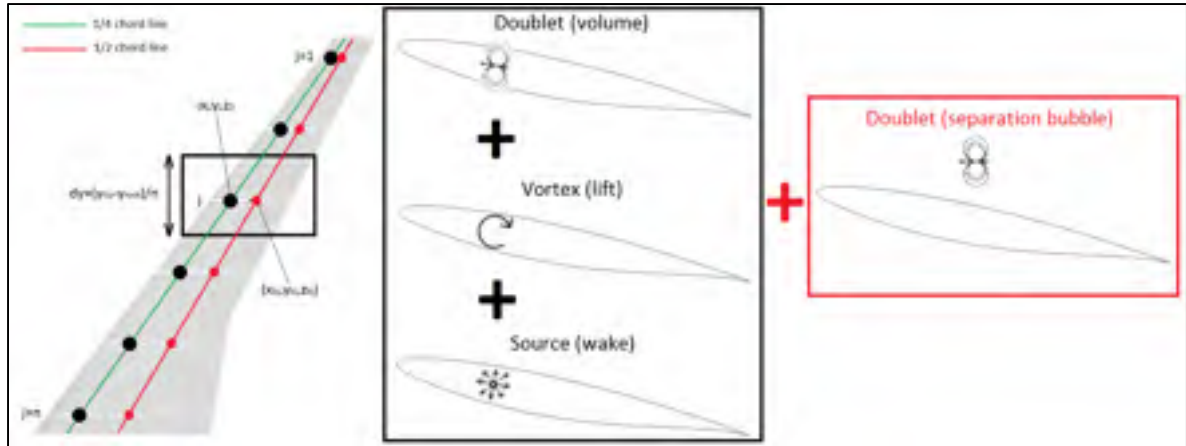


Figure 4.23 Sketch of the singularity distribution employed to represent the model’s wing, including a doublet distribution to represent the separation bubble volume effects.

These new doublets were added to the potential flow representation when separation was detected, on a data point by data point basis. The velocity potential due to this additional separation bubble doublet distribution at a specific  $(x, y, z)$  location can be calculated as determined by Eq. (4.7), where the doublet strength  $\mu_{bj}$  at  $(x_{bj}, y_{bj}, z_{bj})$  is a function of the cross section of the recirculating flow region in the separation bubble at  $y_{bj}$ .

$$\phi_{\text{bubble}}(x, y, z) = \frac{1}{4\pi} \sum_j^n \mu_{bj} \frac{x - x_{bj}}{[(x - x_{bj})^2 + \beta^2(y - y_{bj})^2 + \beta^2(z - z_{bj})^2]^{3/2}} \quad (4.7)$$

The size of these doublets was estimated by making cross sectional cuts in the CFD flow field. An example of this technique is illustrated by Figure 4.24. Although this approach would not be practical in production testing, it was used as a diagnostic tool.

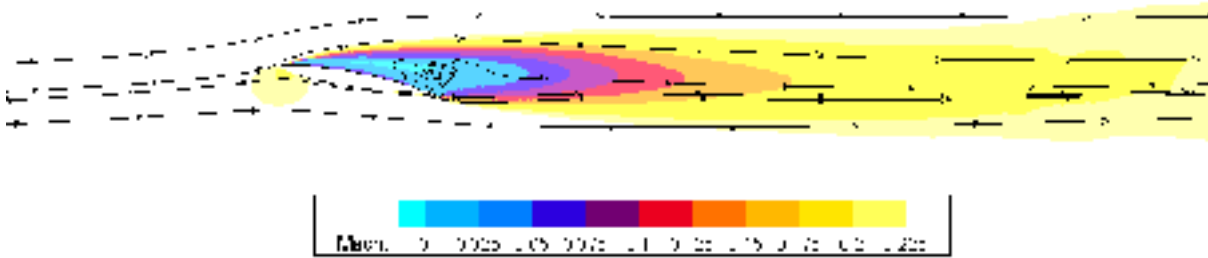


Figure 4.24 CFD predicted separation bubble at CRM wing station  $\eta=0.950$  at  $\alpha=14^\circ$ . The streamlines illustrate the recirculating flow region in the bubble.

The results (Figure 4.25) of this modification to the potential-flow representation had only a minor effect over the corrections bias error. Implementation was deemed not worth the effort even if a convenient, reliable method to determine the size and placement of the additional doublets was available.

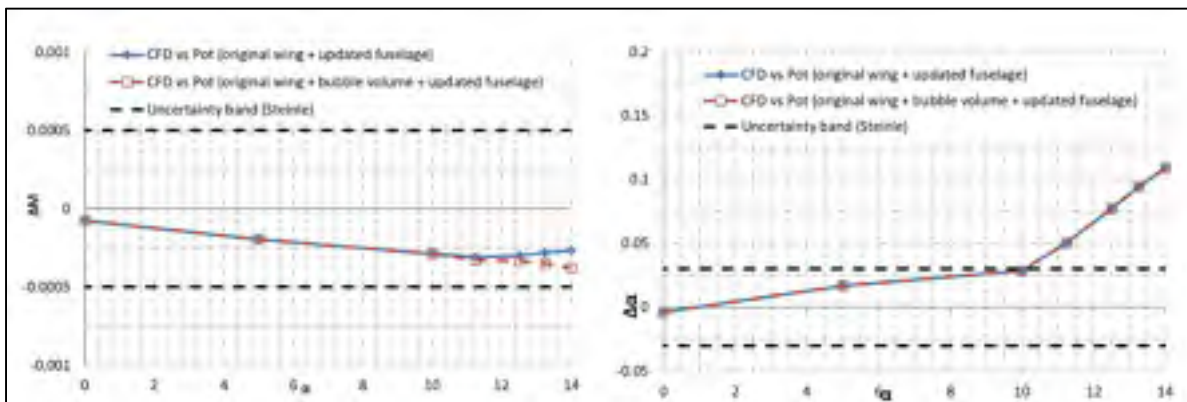


Figure 4.25 Error band for Mach number and angle of attack corrections computed using the one-variable method including the separation bubble volume on the wing representation of the CRM WB.

Next, to account for the lift redistribution caused by the separation at the outboard section of the wing, an attempt to reposition the lift vortices based on an effective wing span  $b_{eff}$  was made (Figure 4.26). Taking into account this modification, the velocity potential due to the redistributed array of horseshoe vortices could be represented following the expression in Eq. (4.8), where  $b_{ref}$  is the (constant) geometric span of the model's wing.

$$\begin{aligned} \Phi_{lift,redis}(x, y, z) &= \frac{1}{4\pi} \sum_j^n \Gamma_j \frac{z - \frac{b_{eff}}{b_{ref}} z_j}{(y - \frac{b_{eff}}{b_{ref}} y_j)^2 + (z - \frac{b_{eff}}{b_{ref}} z_j)^2} \left( 1 \right. \\ &\quad \left. + \frac{x - \frac{b_{eff}}{b_{ref}} x_j}{\sqrt{(x - \frac{b_{eff}}{b_{ref}} x_j)^2 + \beta^2 (y - \frac{b_{eff}}{b_{ref}} y_j)^2 + \beta^2 (z - \frac{b_{eff}}{b_{ref}} z_j)^2}} \right) \end{aligned} \quad (4.8)$$

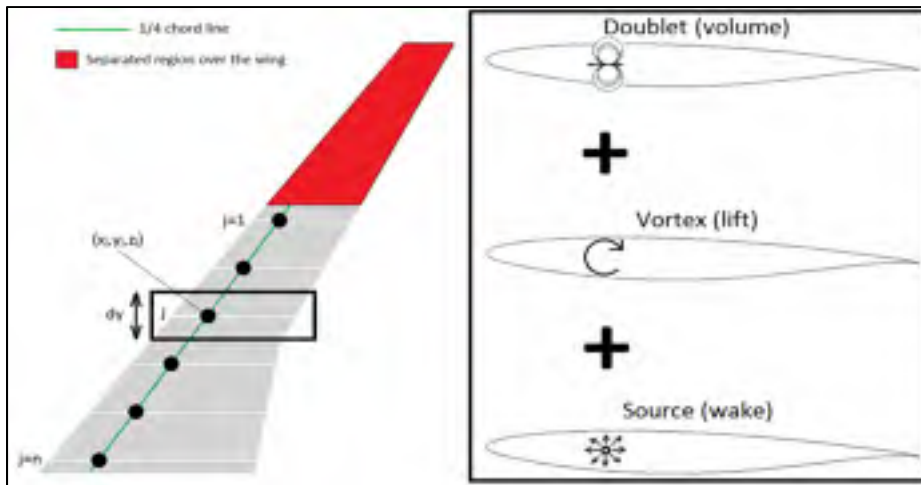


Figure 4.26 Sketch of the singularity distribution employed to represent the model's wing, including the redistribution of the horseshoe vortices to account for flow separation at the outboard region of the wing.

The main challenge of this approach is to find a way to determine the effective wing span as flow separation develops from the outboard region of the suction side of the wing. Initially, the CFD skin friction data (Figure 3.15) was used to estimate the effective wing span, which became smaller due to the outboard stall with increased angles of attack. To keep the potential-flow model as simple as possible, elliptic loading was assumed over the determined effective span. The improvement is evident in the potential-flow model for data points where wing stall is occurring (Figure 4.27).

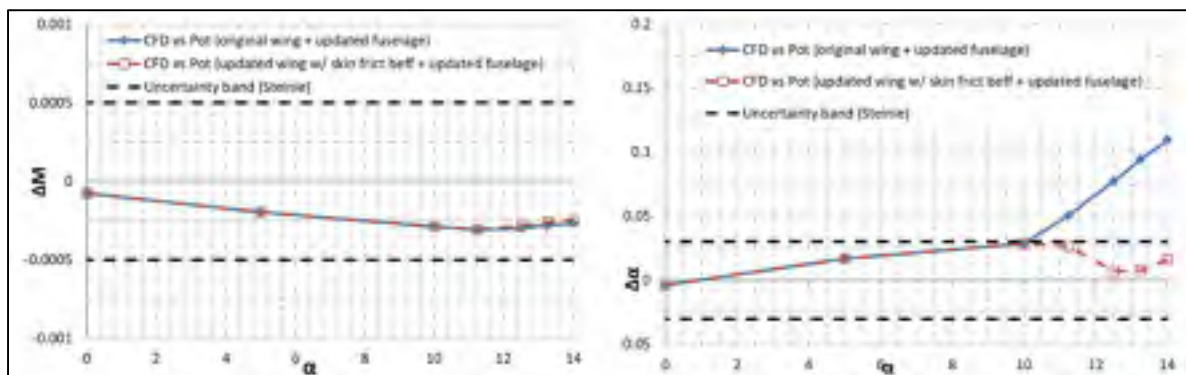


Figure 4.27 Error band for Mach number and angle of attack corrections computed using the one-variable method including the skin friction estimated effective span on the wing representation of the CRM WB.

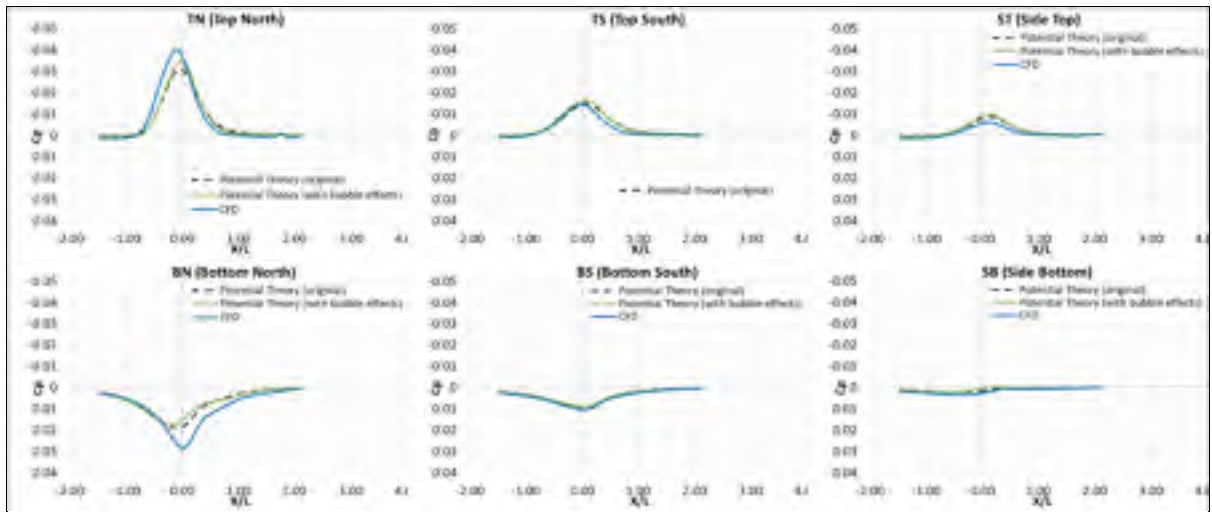


Figure 4.28 Comparison between the farfield pressure signature estimated by the potential-theory representation of the CRM considering the lift vortices redistribution (based on skin friction data from CFD results) and that predicted by CFD at  $\alpha=14^\circ$ ,  $C_L=1.033$ .

From a farfield pressure signature perspective, Figure 4.28 depicts a rail-by-rail comparison between computational results and the potential-theory representation of the model at  $\alpha=14^\circ$ . In general, a better agreement is achieved when redistributing the horseshoe vortices representing the wing's lift based on the effective wing span.

Alternatively, the experimental wing pressure distribution could be used to estimate its effective span. In this approach, the pressure distributions measured at the nine chordwise rows of pressure taps on the CRM wing are analysed to identify pressure plateaus on its suction side, which indicate the presence of flow separation. This allows estimating the extent of flow separation at every data point surveyed. However, in addition to the post-processing effort required to estimate  $b_{eff}$ , wing pressure distributions are not always measured during wind-tunnel tests. Figure 4.29 shows the improvement to the model representation resulting from the implementation of this approach.

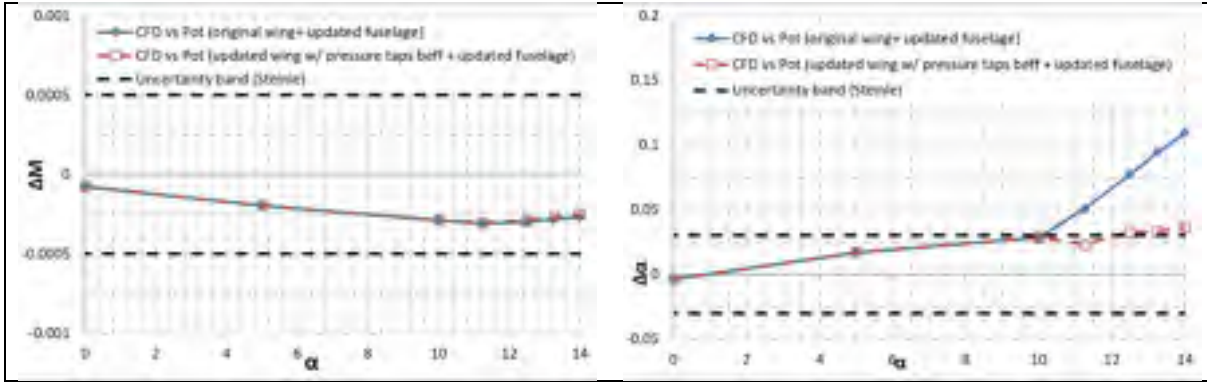


Figure 4.29 Error band for Mach number and angle of attack corrections computed using the one-variable method including the wing pressure tap estimated effective span on the wing representation of the CRM WB.

While the preceding results validate the use of an effective wing-span due to outboard stall, the final goal of this work is to produce an improvement to the wall-correction method that can be implemented in real-time production wind-tunnel tests. Therefore, further investigations were launched to determine how  $b_{eff}$  can be estimated based on the available tunnel measurements. For semispan tests, assuming an elliptical lift distribution,  $b_{eff}$  could be estimated for every  $\alpha$  as a function of the lift coefficient  $C_L$  and the rolling moment coefficient  $C_l$  measured by the balance as expressed by Eq. (4.9).

$$b_{eff} = \frac{C_l}{C_L} \cdot \frac{3\pi b_{ref}}{4} \quad (4.9)$$

Figure 4.30 shows that the “wall interference” results obtained with this approach stay within the acceptable limits of zero, proving that this technique brings an improvement to the wall-correction methodology. It is interesting to note that the use of a measured  $b_{eff}$  reduced the  $\Delta \alpha$  bias error when the wing had fully attached flow, suggesting that this method is an improvement over using just the physical span of the model.



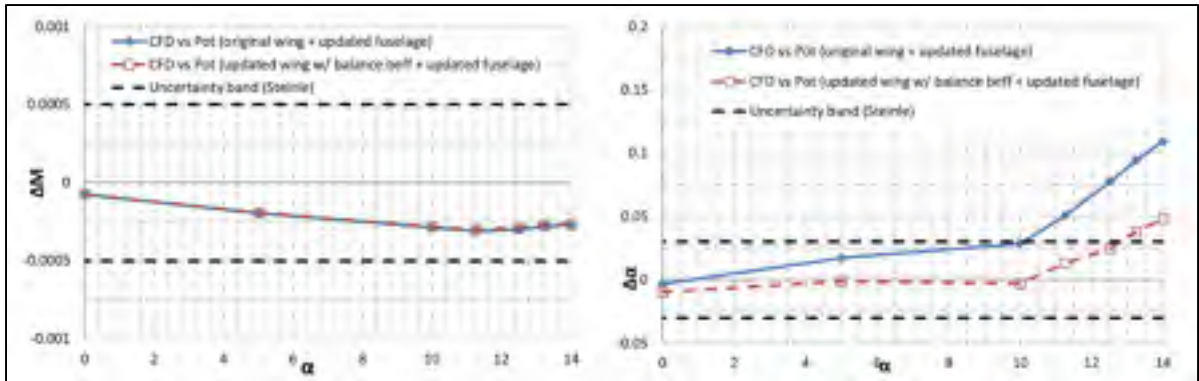


Figure 4.30 Error band for Mach number and angle of attack corrections computed using the one-variable method including the balance data estimated effective span on the wing representation of the CRM WB.

#### 4.5 Overall improvement to Wall Corrections

In this section, the updates to the potential theory representation of the test article are applied to evaluate the overall improvement for the one-variable method. Wall corrections for the available solid-wall experimental data obtained from the test run 56306 (Table 3.5) performed on the CRM WB at the NRC 5ft wind tunnel are calculated using the original and updated potential theory representation of the test article. Solid-wall test data are used in this section, first because corrections are larger than in a ventilated-wall test, and second because it allows comparing the results to well-established standard corrections like ESDU or AGARD.

As Figure 4.31 illustrates, the wall corrections calculated using the simplified potential-flow singularity model match classical textbook corrections in the attached-flow region. This result validates the use of the original potential-flow singularity model to provide the free-air farfield for the one-variable method to obtain production-mode accurate corrections when testing models in pre-stall conditions.

As the angle of attack increases and separation develops on the wing, leading to a progressive drop of the model lift, it would be expected that the angle of attack correction  $\Delta\alpha$  would also drop in some manner. However, this is not the behavior observed from the corrections calculated in the separated flow region by the one-variable method using the original potential-flow singularity representation of the model. These results offer a convincing argument that the  $\Delta\alpha$  trend predicted by the original one-variable method when stall is present at the NRC TWT is not correct and that this is in large part due to errors in the farfield free-air representation of the test article.

The wall-correction results obtained using the updated potential theory representation of the model do show a drop in  $\Delta\alpha$  when flow separation causes a reduction in model lift. Results in terms of  $\Delta M$  replicate those obtained using the standard model representation, which aligns with AGARD estimation. All these results are reliable within a bias error band similar to that shown in Figure 4.30, representing a realistic improvement applicable to production wind-tunnel tests.

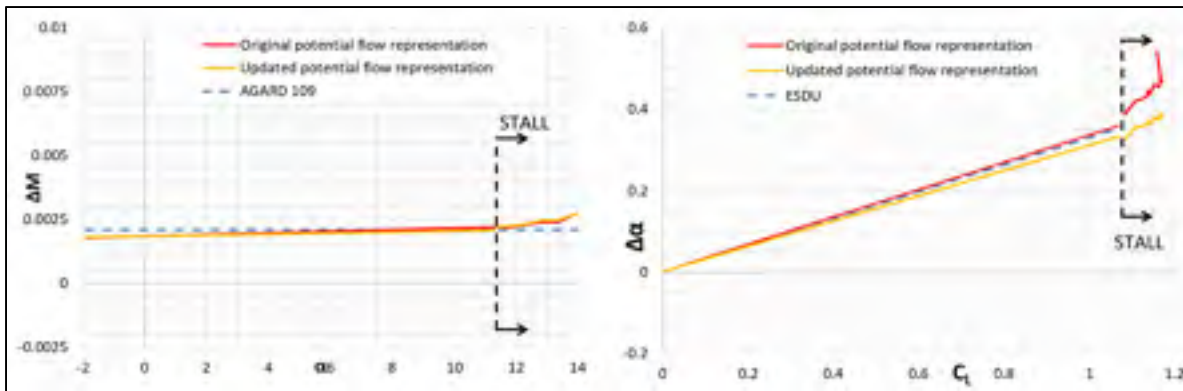


Figure 4.31 Comparison between Mach number and angle of attack corrections computed using the one-variable method for the half-model CRM WB solid-wall test, using the original and updated potential theory model representations.

#### 4.6 CFD-based Wall-Correction Data Set

In an effort to understand what are the realistic trends of the Mach and angle of attack corrections when a typical transport aircraft configuration enters low-speed stall, several

experimental data points from the CRM WB in the solid-wall test section were corrected using the free-air farfield from the validated CFD solutions. Each free-air CFD data point considered for this study (both white and red data points in Figure 4.32) was employed to correct an experimental solid-wall data point of the same (or closest)  $C_L$  value.

In the attached-flow region, the results (Figure 4.33) show a satisfactory agreement of the CFD-based wall corrections with those obtained using standard methods like ESDU or AGARD. These results validate the use of the standard potential flow singularity model to provide the free-air farfield for the one-variable method to obtain production mode accurate corrections when testing models in attached flow conditions. These results also reveal a decrease of  $\Delta\alpha$  as model lift drops (Figure 4.32) when separation grows larger. It should be noted that the decrease rate of  $\Delta\alpha$  with respect to  $C_L$  in stall is faster than experienced in the attached flow region.

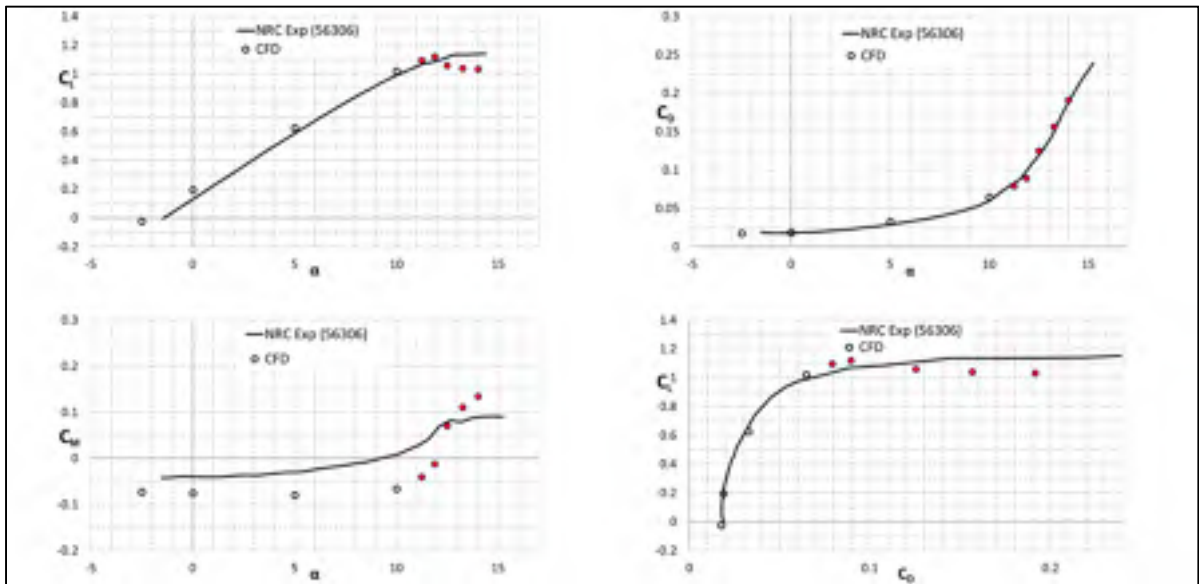


Figure 4.32 CFD predicted aerodynamic coefficients for the CRM WB half-model (red-filled CFD data points indicate flow separation is significant) compared to solid-wall NRC experimental results from run 56306.

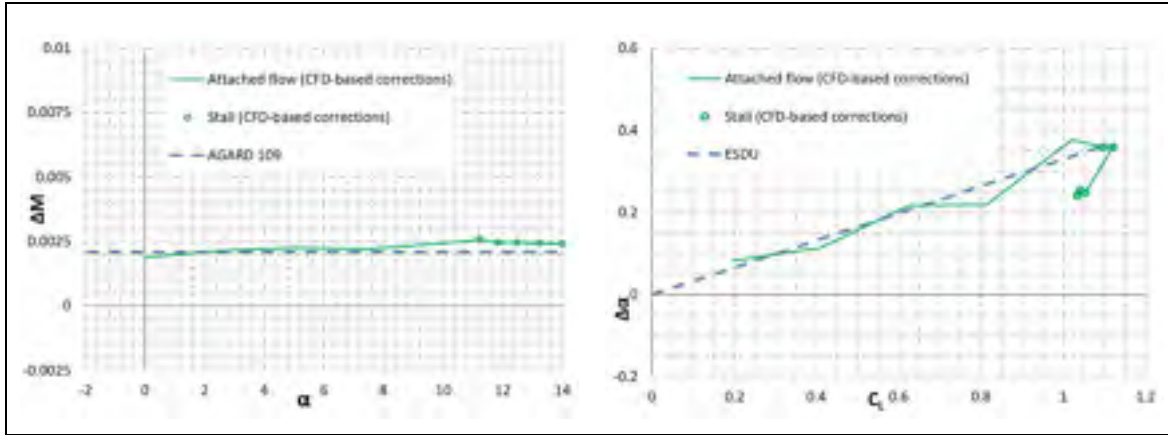


Figure 4.33 Mach number and angle of attack corrections computed using the one-variable method for the half-model CRM WB solid-wall test, based on the validated free-air CFD results.

Although it may be too optimistic to guarantee that these CFD-based wall corrections around stall are “the truth”, they offer a convincing argument that the  $\Delta \alpha$  trend predicted by the standard one-variable method when stall is present at the NRC TWT is not correct and that this is in large part due to errors in the farfield free-air representation of the test article. These results may also provide a better understanding of the behavior of wall corrections for a contemporary transport aircraft tested at low-speed subsonic flow reaching stall conditions.

#### 4.7 Applications to Transonic Flow

Although transonic flows are outside the scope of the work included in this research project, the techniques described in this dissertation were applied to estimate the additional blockage correction necessary to rectify the effect of the supersonic bubble developed over a semispan model tested at the NRC 5ft TWT. Particularly, some work was done in this sense for the 2.7% scale semispan NASA CRM WB. For this study, free-air Euler CFD simulations were performed at  $M=0.8$ ,  $M=0.85$  and  $M=0.87$  at a range of angles of attack between  $\alpha=-1.5^\circ$  and  $\alpha=12^\circ$ .

The effect of a supersonic bubble developing over the wind-tunnel model is not represented by its potential theory representation. The blockage effect generated by this supersonic bubble was calculated by comparing numerical results from free-air CFD simulations of the

flow around the test article at the tunnel boundary to the equivalent farfield results from its original potential-flow singularity representation. By isolating the supersonic bubble effect using this strategy, the additional blockage correction that needs to be applied to the experimental wind-tunnel data in these conditions can be calculated. Model force and moment data were applied to the model singularity representation for every specific data point studied. Figure 4.34 illustrates the results obtained from this technique at transonic-flow.

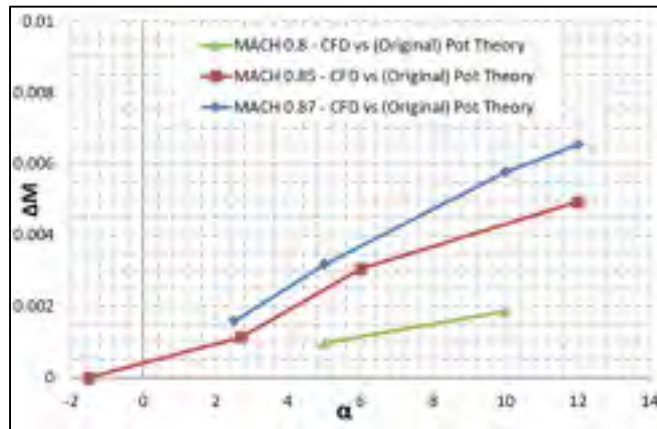


Figure 4.34 Additional Mach number corrections computed using the one-variable method to rectify the supersonic bubble effects over the half-model CRM WB, based on CFD results.

These results can be used as a gauge to determine how accurate the one-variable method corrections are when the model is tested at transonic speeds at the NRC 5ft TWT and could potentially be the start to further studies to improve this wall-correction methodology in transonic flow.



## CONCLUSIONS AND PERSPECTIVES

The main objective of this research project has been to improve the wall-correction methodology at the NRC 5ft Trisonic Wind Tunnel in subsonic wind-tunnel tests reaching stall conditions. For that matter, the one-variable method has been presented and analyzed to point out its limitations. Special attention has been given to the role of the potential-theory representation of the model in the wall-correction methodology.

To allow reprocessing of the available wind-tunnel data, with various modifications to the correction methodology, a test bench has been developed. Preliminary results using a solid-wall dataset from a test performed on a semispan model of the Bombardier Global 6000 show a constant offset between the corrections calculated and those predicted by standard corrections, which has motivated a parametric study to determine the sensitivity of the results to multiple variables involved in the process. The parametric study has revealed little sensitivity to the choice of the computational boundaries or the number of panels making up the computation boundaries (within the range normally used). The importance of flow quality has been indicated by the sensitivity of the  $\Delta\alpha$  correction to the results obtained adding a splitter plate extension to the wind-tunnel reflection plate.

The semispan NASA Common Research Model (CRM) test campaign recently completed at the NRC 5ft TWT has provided the experimental data required for the work presented in this dissertation, including subsonic flow results for the CRM wing/body (WB) configuration. These data have been obtained using both the typically ventilated wall wind-tunnel test section boundary and a solid-wall boundary condition achieved by covering the test section perforated walls. This allows comparing the solid-wall corrections to standard textbook results like those presented by Rae and Pope (1984). Additionally, computational tools have been used to estimate the flow behavior around the model in free-air at the same conditions tested in the tunnel.

In an initial stage, the computational data generated has been applied to validate the one-variable method without the need for experimental wind-tunnel data. Particularly, numerical results calculated for the 2.7% scale semispan NASA Common Research Model (CRM), in its wing/body configuration, have been employed. The validation approach has consisted of modifying the wall-correction methodology to take high fidelity free-air CFD results as measured wind-tunnel data and then comparing it to the free-air potential theory representation of the test article typically employed by the one-variable method, the objective being to obtain  $\Delta M$  and  $\Delta \alpha$  “zero-corrections” for every data point studied. The quality of the results has been assessed based on uncertainty budgets for high lift testing applications taken from Steinle and Stanewsky (1982), revealing that although the one-variable method is reliable in attached-flow conditions it lacks accuracy when flow separation develops on the test article. It has been understood that improving the potential-theory representation of the test article currently applied at the NRC 5ft TWT should improve the overall wall-correction methodology. To this end, the issues with the model representation at high angle of attack and in stall conditions have been addressed.

First, a (Euler) CFD-based study of the potential theory representation of the fuselage currently used at the NRC 5ft TWT has been performed. As a result, the current Rankine body fuselage representation has been replaced by a new fuselage representation consisting of  $n$  sources/sinks and  $n$  doublets evenly distributed at  $n$  locations over the fuselage centerline, that provides an accurate representation of the flow around a pitching fuselage in the farfield. This updated fuselage representation is ready to be implemented in real wind-tunnel tests. The repercussions of replacing the Rankine body representation of the fuselage by its updated version are not likely to be significant to wind-tunnel tests using a complete aircraft half-model, but could have a greater importance for wind-tunnel tests where the test article is essentially a large scale body of revolution (e.g. a missile).

Next, to study the flow behavior around the model’s wing, a series of Reynolds-Averaged Navier-Stokes (RANS) simulations were performed. These computational results were validated using balance model forces and moments, as well as wing pressures measured in the wind tunnel as part of the ventilated-wall experimental data. An analysis of the available



experimental and computational data has resulted in a better understanding of the development of low speed flow separation on the CRM WB, allowing a characterization of the evolution of the size and position of the separation bubble on the suction side of the model wing. This information has been applied to include an additional distribution of doublets to the potential theory representation of the wing to account for the separation bubble volume effects. Some level of improvement has been achieved, as proved by the comparison between the original wing representation, its updated version including separation bubble volume effects, and free-air CFD results. However, this update does not translate into a significant improvement to the overall wall corrections.

An additional effort was made to improve the wing representation at high angles of attack by repositioning the lift vortices to account for the lift redistribution caused by the separation at the outboard section of the wing based on the effective wing span  $b_{eff}$ . An initial proof of concept estimated the effective wing span based on the x-component of the skin friction coefficient obtained from the free-air CFD RANS simulations, showing promising wall-correction results. To make this approach applicable to production wind-tunnel tests, it was necessary to find a way to determine the effective wing span as flow separation develops on the suction side of the wing based on the available tunnel measurements. Assuming an elliptical lift distribution, a strategy to estimate  $b_{eff}$  for every  $\alpha$  as a function of the lift coefficient  $C_L$  and the rolling moment coefficient  $C_l$  measured by the balance has been described. Alternative ways to calculate the effective wing span based on experimentally measured wing pressures or flow visualization techniques have been tested. Using the free-air numerical results as a reference, a general improvement has been demonstrated in the results for the wall corrections obtained using the redistribution of the lift (horseshoe) vortices.

Finally, the available semispan CRM WB solid-wall experimental data set has been corrected using the validated free-air CFD solutions in lieu of the potential-theory representation of the

model. A number of data points have been investigated, some reaching high angles of attack. The corrections obtained in pre-stall match standard corrections like ESDU, which is consistent with the results obtained throughout this whole dissertation. In the separated flow region, the use of the validated CFD results has provided a sensible response by showing the general trend wall corrections should follow in these flow conditions. This result represents a general guideline for the tunnel engineer to make informed decisions when testing an aircraft in subsonic flow conditions reaching stall.

Future perspectives for this work include transonic-flow applications. Initial experiments conducted at the NRC 5ft TWT on the semispan NASA CRM WB at transonic flows have proved that the technique presented in this paper, comparing CFD simulations to potential theory results, may be applicable in transonic wind-tunnel tests to complement the wall corrections traditionally calculated by the one-variable method.

## REFERENCES

- Abbott, I. H., & Von Doenhoff, A. E. (1959). *Theory of wing sections, including a summary of airfoil data*. Courier Corporation.
- Allmaras, S. R., & Johnson, F. T. (2012). Modifications and clarifications for the implementation of the Spalart-Allmaras turbulence model. *Seventh international conference on computational fluid dynamics (ICCFD7)* (pp. 1-11).
- Anderson Jr, J. D. (1984). *Fundamentals of aerodynamics*. WCB/McGraw-Hill Education.
- Anderson, J. D., & Wendt, J. (1995). *Computational fluid dynamics – The Basic with Applications*. WCB/McGraw-Hill.
- Anderson, J. D. (1999). *Aircraft performance and design*. WCB/McGraw-Hill.
- Antón, P. S., Gritton, E. C., Mesic, R., Steinberg, P., & Johnson, D. J. (2004). *Wind Tunnel and Propulsion Test Facilities: An Assessment of NASA's Capabilities to Serve National Needs*. The RAND Corporation Technical Report TR-134.
- Ashill, P. R. (1993). Boundary-flow measurement methods for wall interference assessment and correction: Classification and review. *73rd AGARD Fluid Dynamics Panel Meeting and Symposium on Wall Interference, Support Interference and Flowfield Measurements*.
- Ashill, P. R., & Weeks, D. J. (1982). A method for determining wall-interference corrections in solid-wall tunnels from measurements of static pressure at the walls. *AGARD Wall Interference in Wind Tunnels 12 p (SEE N 83-20957 11-09)*.
- Ashill, P. R., & Keating, R. F. A. (1988). Calculation of tunnel wall interference from wall-pressure measurements. *The Aeronautical Journal*, 92(911), 36-53.
- Aupoix, B., et al. (2011). Transition and turbulence modeling. *AerospaceLab*, (2), p-1.
- Baals, D. D., & Corliss, W. R. (1981). *Wind tunnels of NASA*. Vol. 440. Scientific and Technical Information Branch, National Aeronautics and Space Administration.
- Blackwell Jr, J. A. (1982). Experimental testing at transonic speeds. *Transonic Aerodynamics, Progress in Astrodynamics and Aerodynamics*, 81, 189-238.

- Boone, A., & Ulbrich, N. (2002). The development of a wall pressure measurement system for two NASA Ames wind tunnels. In *22nd AIAA Aerodynamic Measurement Technology and Ground Testing Conference* (p. 3250).
- Bouriga, M., Morency, F., & Weiss, J. (2015). Numerical investigation of wall mounting effects in semi-span wind-tunnel tests. In *53rd AIAA Aerospace Sciences Meeting* (p. 2025).
- Broughton, C. (2013). *2012 Half-model Wall Correction Study Results*. National Research Council Canada.
- Bushnell, D. M. (2006). Scaling: Wind tunnel to flight. *Annu. Rev. Fluid Mech.*, 38, 111-128.
- Capelier, C., Chevalier, J. P., & Bouniol, F. (1978). *Nouvelle methode de correction des effets de parois en courant plan*. CEDOCAR [Centre de documentation de l'armement].
- Cebeci, T., Chang, K., Clark, R., & Sedlock, D. (1989). Analysis of wings with flow separation. *Journal of aircraft*, 26(3), 214-220.
- Chapman, D. R. (1979). Computational aerodynamics development and outlook. *AIAA journal*, 17(12), 1293-1313.
- Cobalt, CFD, Software Package, Ver. 7.1, Cobalt solutions, LLC.
- Dougherty, JR, N., Anderson, C., & Parker, JR, R. (1976). An experimental study on suppression of edgetones from perforated wind tunnel walls. In *14th Aerospace Sciences Meeting* (p. 50).
- Elfstrom, G. M., & Templin, J. T. (2001). A Canadian partnership in development of aerospace and automotive test technology. *Canadian Aeronautics and Space Journal*, 47(3), 327.
- Erickson, L. L. (1990). *Panel methods: An introduction*. NAAS Technical Paper 2995.
- ESDU. (1995). *Upwash Interference for Wings in Solid-Liner Wind Tunnel Using Subsonic Linearised-Theory*. Engineering Sciences Data Unit No. 95014.
- Ewald, B. F. (1998). *Wind Tunnel Wall Corrections (la Correction des effets de paroi en soufflerie)* (No. AGARD-AG-336). Advisory Group for Aerospace Research and Development, Neuilly-sur-Seine (FRANCE).
- Franz, H. P. (1982). The half-model technique in the wind tunnel and its employment in the development of the airbus family.

- Garner, H. C., Rogers, E. W., Acum, W. E., & Maskell, E. C. (1966). *Subsonic wind tunnel wall corrections* (No. AGARD-OGRAPH-109). Advisory Group for Aerospace Research and Development, Neuilly-sur-Seine (FRANCE).
- Gatlin, G. M., & McGhee, R. J. (1997). Experimental investigation of semispan model testing techniques. *Journal of aircraft*, 34(4), 500-505.
- Gilmer, B. R., & FERNANDO, M. (1982). Analysis of stalled airfoils by simultaneous perturbations to viscous and inviscid equations. *AIAA Journal*, 20(9), 1160-1166.
- Glauert, H. (1933). *Wind tunnel interference on wings, bodies and airscrews* (No. ARC-R/M-1566). AERONAUTICAL RESEARCH COUNCIL LONDON (UNITED KINGDOM).
- Goett, H. J., & Bullivant, W. K. (1939). Tests of NACA 0009, 0012, and 0018 airfoils in the full-scale tunnel. NACA-TR-647.
- Goldstein, E. (2010). Wind Tunnels: don't count them out - The nation's wind tunnels, even in a period of growing decline, still offer vital insights that computers cannot match. *Aerospace America*, 48(4), 38.
- Gorbushin, A., Bosnyakov, S., Glazkov, S. A., Llysenkov, A. V., Matyash, S. V., Semenov, A. V., & Quest, J. (2015). Slotted Wall Interference Investigation in ETW using the NASA CRM model. In *53rd AIAA Aerospace Sciences Meeting* (p. 0621).
- Quest, J., & Gross, N. (2004). The ETW Wall Interference Assessment for Full and Half Models. In *42nd AIAA Aerospace Sciences Meeting and Exhibit* (p. 769).
- Hackett, J. E., Wilsden, D. J., & Lilley, D. E. (1979). Estimation of tunnel blockage from wall pressure signatures: a review and data correlation. NASA-CR-152241.
- Hackett, J. E., Wilsden, D. J., & Stevens, W. A. (1980). A review of the wall pressure signature and other tunnel constraint correction methods for high angle-of-attack tests. (No. AGARD-R-692). Advisory Group for Aerospace Research and Development, Neuilly-sur-Seine (FRANCE).
- Hoerner, S. F., & Borst, H. V. (1975). Fluid-Dynamic Lift, Hoerner Fluid Dynamics, Bakersfield, CA. In *Library of Congress Catalog Card* (No. 75-17441).
- Horton, H. P. (1968). *Laminar separation bubbles in two and three dimensional incompressible flow* (Doctoral dissertation). Queen Mary University of London, UK.

ICEM, CFD, Software Package, Ver. 15.0, ANSYS Inc., Southpointe 275.

Iyer, V., & Everhart, J. (2001). Application of pressure-based wall-correction methods to two NASA Langley wind tunnels. In *19th AIAA Applied Aerodynamics Conference* (p. 2472).

Iyer, V., Everhart, J., Bir, P., & Ulbrich, N. (2000, January). Implementation of the WICS Wall Interference Correction System at the National Transonic Facility. In *21st Aerodynamic Measurement Technology and Ground Testing Conference* (p. 2383).

Iyer, V., Kuhl, D., & Walker, E. (2003). Improvements to Wall Corrections at the NASA Langley 14x22-Ft Subsonic Tunnel. In *21st AIAA Applied Aerodynamics Conference* (p. 3950).

Katz, J., & Plotkin, A. (2001). *Low-speed aerodynamics* (Vol. 13). Cambridge University Press.

Keller, J. D. (1972). Numerical calculation of boundary-induced interference in slotted or perforated wind tunnels including viscous effects in slots. NASA-TN-D-6871.

Keye, S., & Mavriplis, D. J. (2017). Summary of Data from the Sixth AIAA CFD Drag Prediction Workshop: Case 5 (Coupled Aero-Structural Simulation). In *55th AIAA Aerospace Sciences Meeting* (p. 1207).

Kilgore, R. A., Goodyer, M. J., Adcock, J. B., & Davenport, E. E. (1974). The cryogenic wind tunnel concept for high Reynolds number testing. NASA-TN-D-7762.

Kiya, M., & Sasaki, K. (1983). Structure of a turbulent separation bubble. *Journal of Fluid Mechanics*, 137, 83-113.

Kiya, M., Sasaki, K., & Arie, M. (1982). Discrete-vortex simulation of a turbulent separation bubble. *Journal of Fluid Mechanics*, 120, 219-244.

Kohzai, M., Ueno, M., Koga, S., & Sudani, N. (2013). Wall and Support Interference Corrections of NASA Common Research Model Wind Tunnel Tests in JAXA. In *51st AIAA Aerospace Sciences Meeting Including the New Horizons Forum and Aerospace Exposition* (p. 963).

Kraft, E. M. (2010). *After 40 years why hasn't the computer replaced the wind tunnel?*. Arnold Engineering Development Center, Arnold Air Force Base, TN.

Kuethe, A. M., & Chow, C. Y. (1986). *Fundamentals of aerodynamics: bases of aerodynamic design*. Wiley.

Lee-Rausch, E., Buning, P., Mavriplis, D., Morrison, J., Park, M., Rivers, S., & Rumsey, C. (2003). CFD sensitivity analysis of a drag prediction workshop wing/body transport

- configuration. In *21st AIAA Applied Aerodynamics Conference*(p. 3400).
- Lutz, T. (2015). Time-resolved prediction and measurement of the wake past the crm at high reynolds number stall conditions. In *53rd AIAA Aerospace Sciences Meeting* (p. 1094).
- Ueno, M., Kohzai, M., Koga, S., Kato, H., Nakakita, K., & Sudani, N. (2013). 80% scaled NASA Common Research Model wind tunnel test of JAXA at relatively low Reynolds number. In *51st AIAA Aerospace Sciences Meeting including the New Horizons Forum and Aerospace Exposition*(p. 493).
- Malik, M. R., & Bushnell, D. M. (2012). Role of computational fluid dynamics and wind tunnels in aeronautics R and D. NASA/TP-2012-217602.
- Maskell, E. C. (1963). *A theory of the blockage effects on bluff bodies and stalled wings in a closed wind tunnel* (No. ARC-R/M-3400). Aeronautical Research Council London (United Kingdom).
- Mavriplis, D. (2005). Grid resolution study of a drag prediction workshop configuration using the NSU3D unstructured mesh solver. In *23rd AIAA Applied Aerodynamics Conference* (p. 4729).
- Milne-Thomson, L. M. (1973). *Theoretical aerodynamics*. Courier Corporation.
- Mokry, M. (2006). *Subsonic Wall Corrections in the IAR 1.5m Wind Tunnel*. Laboratory Report LR-AL-2006-0056, National Research Council Canada.
- Mokry, M. (1985). *Subsonic wall interference corrections for half-model tests using sparse wall pressure data*. National Research Council Canada.
- Mokry, M., Digney, J. R., & Poole, R. J. D. (1987). Doublet-panel method for half-model wind-tunnel corrections. *Journal of aircraft*, 24(5), 322-327.
- Nelson, T. E., & Zingg, D. W. (2004). Fifty years of aerodynamics: successes, challenges, and opportunities. *Canadian Aeronautics and Space Journal*, 50(1), 61-84.
- Ohman, L. H., Nguyen, V. D., Ellis, F., Thain, J., Tang, N., Broughton, C., & Bureau, J. (2001). The IAR 1. 5 m Trisonic Blowdown Wind Tunnel- A review of its history and development. *Canadian Aeronautics and Space Journal*, 47(3), 163-173.
- O'meara, M., & Mueller, T. J. (1987). Laminar separation bubble characteristics on an airfoil at low Reynolds numbers. *AIAA journal*, 25(8), 1033-1041.

- Palacios, F., et al. (2013). Stanford university unstructured (su 2): an open-source integrated computational environment for multi-physics simulation and design. In *51st AIAA aerospace sciences meeting including the new horizons forum and aerospace exposition* (p. 287).
- Palacios, F., et al. (2014). Stanford university unstructured (SU2): Analysis and design technology for turbulent flows. In *52nd Aerospace Sciences Meeting* (p. 0243).
- Rae, W. H., & Pope, A. (1984). *Low-speed wind tunnel testing*. John Wiley.
- Rivers, M., & Hunter, C., (2012). *Support System Effects on the NASA Common Research Model*. AIAA Paper 707.
- Rivers, M., Hunter, C., & Campbell, R. (2012). Further investigation of the support system effects and wing twist on the NASA common research model. In *30th AIAA Applied Aerodynamics Conference* (p. 3209).
- Rivers, M. B., & Dittberner, A. (2014). Experimental investigations of the NASA common research model. *Journal of Aircraft*, 51(4), 1183-1193.
- Rivers, M. B., Rudnik, R., & Quest, J. (2015). Comparison of the NASA Common Research Model European Transonic Wind Tunnel Test Data to NASA Test Data. In *53rd AIAA Aerospace Sciences Meeting* (p. 1093).
- Rivers, M., & Dittberner, A. (2011). Experimental Investigations of the NASA Common Research Model in the NASA Langley National Transonic Facility and NASA Ames 11-ft Transonic Wind Tunnel. In *49th AIAA Aerospace Sciences Meeting including the new horizons forum and aerospace exposition* (p. 1126).
- Roy, C. J. (2017). Summary of data from the sixth AIAA CFD drag prediction workshop: case 1 code verification. In *55th AIAA Aerospace Sciences Meeting* (p. 1206).
- Rumsey, C. L. (2007). Apparent transition behavior of widely-used turbulence models. *International Journal of Heat and Fluid Flow*, 28(6), 1460-1471.
- Schlichting, H. T., & Truckenbrodt, E. A. (1979). *Aerodynamics of the Airplane*. McGraw-Hill Companies.
- Spalart, P., & Allmaras, S. (1992). A one-equation turbulence model for aerodynamic flows. In *30th aerospace sciences meeting and exhibit* (p. 439).
- Steinle, F., & Stanewsky, E. (1982). *Wind tunnel flow quality and data accuracy requirements* (No. AGARD-AR-184). Advisory Group for Aerospace Research and Development, Neuilly-sur-Seine (FRANCE).



- Tinoco, E. N., Bogue, D. R., Kao, T. J., Yu, N. J., Li, P., & Ball, D. N. (2005). Progress toward CFD for full flight envelope. *The Aeronautical Journal*, 109(1100), 451-460.
- Tinoco, E. N., Brodersen, O., Keye, S., & Laflin, K. (2017). Summary of Data from the Sixth AIAA CFD Drag Prediction Workshop: CRM Cases 2 to 5. In *55th AIAA Aerospace Sciences Meeting* (p. 1208).
- Toledano, A., Broughton, C., Morency, F., & Weiss, J. (2015). Improvement of subsonic wall corrections in an industrial wind tunnel. *CASI 62nd Aeronautics Conference and AGM*, Montreal.
- Toledano, A., Weiss, J., Morency, F., Broughton, C., & Benmeddour, A. (2016). Towards the use of CFD to improve and validate the wall-correction methodology at the NRC 1.5 m trisonic wind tunnel. In *32nd AIAA Aerodynamic Measurement Technology and Ground Testing Conference* (p. 3497).
- Toledano, A., Weiss, J., Morency, F., Broughton, C., & Benmeddour, A. (2017). Study of the Subsonic Wall Interference in Stall of the NASA CRM at the NRC 1.5 m Trisonic Wind Tunnel. In *33rd AIAA Aerodynamic Measurement Technology and Ground Testing Conference* (p. 4130).
- Ulbrich, N., & Boone, A. R. (2003). Direct validation of the wall interference correction system of the Ames 11-foot Transonic Wind Tunnel. NASA/TM-2003-212268.
- Ulbrich, N. (2000). *Description of panel method code ANTARES*. NASA/CR-2000-209592.
- Ulbrich, N., & Boone, A. (1998). Real-time wall interference correction system of the 12 ft pressure wind tunnel. In *36th AIAA Aerospace Sciences Meeting and Exhibit* (p. 707).
- Ulbrich, N., & Boone, A. (2001). Determination of the wall boundary condition of the NASA Ames 11ft Transonic Wind Tunnel. In *39th Aerospace Sciences Meeting and Exhibit* (p. 1112).
- Ulbrich, N. (2002). The application of panel method code ANTARES to wind tunnel wall interference problems. In *40th AIAA Aerospace Sciences Meeting & Exhibit* (p. 307).
- Vallentine, H. R. (2013). *Applied hydrodynamics*. Springer.
- Vassberg, J., Dehaan, M., Rivers, M., & Wahls, R. (2008). Development of a common research model for applied CFD validation studies. In *26th AIAA Applied*

*Aerodynamics Conference* (p. 6919).

Vaucheret, X. (1982). *Améliorations des calculs des effets de parois dans les souffleries industrielles de l'ONERA*. Paper 11 in AGARD CP-335.

Waldmann, A., Gansel, P. P., Lutz, T., & Krämer, E. (2015). Unsteady wake of the nasa common research model in low-speed stall. *Journal of Aircraft*, 53(4), 1073-1086.

Waldmann, A., Lutz, T., & Krämer, E. (2016). Wind Tunnel Support System Influence on NASA Common Research Model at Low Speed Conditions. In *32nd AIAA Aerodynamic Measurement Technology and Ground Testing Conference* (p. 3655).

Walker, E. L. (2005). Statistical calibration and validation of a homogeneous ventilated wall-interference correction method for the National Transonic Facility (Doctoral dissertation). Virginia Polytechnic Institute and State University.

Walker, E., Everhart, J., & Iyer, V. (2001). Sensitivity study of the wall interference correction system (WICS) for rectangular tunnels. In *39th Aerospace Sciences Meeting and Exhibit* (p. 159).

Weiss, J., Mohammed-Taifour, A., & Schwaab, Q. (2015). Unsteady behavior of a pressure-induced turbulent separation bubble. *AIAA Journal*.

Wilcox, D. C. (1998). *Turbulence modeling for CFD* (Vol. 2, pp. 172-180). La Canada, CA: DCW industries.

Yasue, K., Ueno, M., Koga, S., & Kohzai, M. (2015). CFD-Aided Model Deformation Corrections of NASA Research Model Wind Tunnel data. In *53rd AIAA Aerospace Sciences Meeting* (p. 0620).

